Université de Lille
Ecole Graduée Mathématiques-Sciences du numérique et de leurs interactions
Caranx Medical

Thèse de Doctorat

Conception, modélisation et développement d'un robot endoscopique chirurgical souple

---

Design, Modeling, and Development of a Soft Robotic Surgical Endoscope

Flavie PRZYBYLSKI

Directeurs de thèse:
Christian DURIEZ, Director of Research at INRIA Lille
Pierre BERTHET-RAYNE, Co-founder and CTO of Caranx Medical

Co-directeurs de thèse:
Jérémie DEQUIDT, Professor at Université de Lille
Yinoussa ADAGOLODJO, Associate Professor at Université de Lille

Président du jury:
Christos BERGELES, Professor at King's College London

Rapporteurs:
Kaspar ALTHOEFER, Professor at Queen Mary University of London
Vincent LEBASTARD, Professor at Institut Mines-Télécom Atlantique

Examinateur:
Tania MORIMOTO, Associate Professor at University of California San Diego

6 Février 2026

"Dicebat Bernardus Carnotensis nos esse quasi nanos, gigantium humeris insidentes, ut possimus plura eis et remotiora videre, non utique proprii visus acumine, aut eminentia corporis, sed quia in altum subvenimur et extollimur magnitudine gigantea."

"Bernard de Chartres disait que nous sommes comme des nains assis sur des épaules de géants. Si nous voyons plus de choses et plus lointaines qu'eux, ce n'est pas à cause de la perspicacité de notre vue, ni de notre grandeur, c'est parce que nous sommes élevés par eux."

Abstract

Minimally invasive endovascular navigation, particularly in procedures such as transcatheter aortic valve implantation, offers major clinical benefits but remains constrained by the rigidity of conventional catheters. These devices can generate frictional and contact forces that may cause vascular injury in tortuous, calcified, or stenotic arteries. To address these limitations, this thesis proposes a soft eversion-based robotic approach in which a thin membrane progressively turns inside out under internal fluid pressurization, thereby reducing sliding contact and promoting atraumatic advancement within complex vascular geometries.

Because endovascular safety requirements impose the use of a physiological fluid for actuation, fluid pressurization constitutes a structural condition of the problem. Initial experimental investigations revealed that internal liquid pressurization can induce membrane stiffening, limiting local adaptability and increasing stresses transmitted to the arterial wall. This work therefore focuses on preserving the intrinsic compliance of the eversion mechanism while explicitly accounting for the mechanical effects introduced by fluid pressurization.

Three main contributions were developed within this framework. First, a membrane based modeling approach was established within the SOFA environment to represent eversion under internal pressurization and to analyze stress redistribution and deployment stability in confined geometries. Second, a material design methodology was derived from numerical simulations and experimentally validated to restore effective compliance under pressure, leading to the selection of thermoplastic polyurethane as a suitable membrane material. Third, a functional robotic system integrating a central working channel and a controlled pressure regulation architecture was realized and validated on synthetic vascular phantoms, as well as on cadaveric and porcine models, demonstrating the feasibility of fluid-actuated atraumatic navigation in conditions approaching the clinical context.

Note on Terminology

In the scientific literature, the phenomenon studied in this thesis appears under various terminologies, such as *eversion*, *extraversion*, or *everted tube*. This terminological diversity reflects both the historical evolution of the concepts and the parallel development of research across different fields, ranging from medical robotics to soft structures. While these expressions all describe the same principle of inside-out growth, other related notions such as *toposcopic* devices refer to specific instruments based on eversion mechanisms rather than alternative designations of the phenomenon itself.

In the section dedicated to the state of the art, each term is preserved as it appears in the original works, in order to respect the terminology and understanding specific to each era. However, for the sake of clarity and consistency, the remainder of this manuscript will uniformly employ the term **eversion**. This choice ensures a clear and coherent reading of the chapters devoted to the modeling and design of the robot, where the use of a unified terminology facilitates the understanding of the phenomenon under study.

Acknowledgements

I would like to start by thanking Professor Althoefer, Professor Bergeles, Professor Lebastard, and Dr. Morimoto for taking part in my defense committee and for evaluating this work.

Je tiens avant tout à exprimer ma plus profonde gratitude à mon directeur de thèse, Christian, pour sa bienveillance, sa disponibilité et son implication exceptionnelle. Il a toujours été présent, attentif et engagé, aussi bien dans le suivi scientifique que dans l'accompagnement humain. Son écoute et sa présence constante m'ont portée tout au long de cette thèse, et j'ai conscience de la chance d'avoir été encadrée par quelqu'un d'aussi investi.

Je remercie également mon co-encadrant, Jérémie, pour sa participation active, sa rigueur et sa vision globale qui ont contribué à la dynamique de cette recherche.

Un grand merci à Younes, toujours disponible, efficace et de bonne humeur. Sa présence et sa coopération ont souvent simplifié les moments les plus complexes.

Ma gratitude va aussi à Pierre, qui m'accompagne depuis mes débuts. C'est lui qui m'a encouragée à aller plus loin et à croire en ce projet. Au-delà du cadre professionnel, j'ai découvert une personne passionnée, humaine et profondément inspirante, avec qui j'ai eu la chance de construire une véritable complicité.

Je souhaite également remercier Éric, pour son énergie communicative, sa capacité à prendre des risques et à transformer chaque défi en occasion d'apprendre (et, parfois, de survivre grâce à une bonne dose de Monster !).

Merci à Anna, dont les conseils et la clarté d'esprit m'ont souvent permis de retrouver du recul et de la sérénité. Sa bienveillance et sa lucidité ont profondément marqué ma manière de voir les choses.

Je remercie toute l'équipe de Caranx pour ces années incroyables. Travailler dans un environnement où la curiosité, l'entraide et la bienveillance sont au coeur du quotidien a été une véritable chance.

Ma reconnaissance va également à ma famille, mes parents, ma soeur, mon frère, ma grand-mère, mon beau-frère et ma belle-soeur, pour leur présence, leur soutien et ces moments partagés qui m'ont permis de retrouver légèreté et équilibre.

Une pensée particulière pour mes oncles et mes tantes, pour leurs attentions simples et sincères.

À mes amis, un immense merci. La bande de toujours, Béré, JB, Jéjé, Lulu, Nico, Sarah et Vic, depuis plus de dix ans, vous êtes là, fidèles et bienveillants. Vos rires, vos messages et vos mots ont su remettre les choses en perspective quand il le fallait. Je ne vous le dis peut-être pas assez, mais votre amitié m'a portée plus d'une fois. À mes gâtés du quotidien, Andrea, Carlo, Célia, Coco, Iona, Jerem, Kieran, Luc et Romain, merci pour votre amitié, vos éclats de rire et cette bonne humeur contagieuse.

Et bien sûr, Camille et Federica, les copines de thèse, les confidentes, les compagnes de route. Merci pour les soirées tardives, les doutes partagés, les moments d'épuisement et les fous rires absurdes qui ont tout sauvé. Vous avez été un soutien unique, à la fois sincère et joyeux.

Enfin, une pensée toute particulière pour mes deux petits neveux adorés, Marius et César. L'un déborde d'énergie et de rires, l'autre s'émerveille encore de tout. Ensemble, ils incarnent ce qu'il ne faut jamais oublier, même au coeur des plus grandes aventures : la joie, la curiosité et la capacité de s'émerveiller.

Merci à toutes les personnes qui ont, d'une manière ou d'une autre, accompagné ce parcours.

Table of Contents

Abstract **3**
Acknowledgements **5**
Table of Contents **7**
List of Tables **11**
List of Figures **13**
1 Introduction **27**
Publications 31
2 From Catheter to Soft Robotics **35**
2.1 Early explorations toward atraumatic navigation 36
2.2 Silverman's conceptual breakthrough 37
2.3 The legacy of a principle 38
2.3.1 Technological variants from patents 39
2.3.2 Experimental biomedical investigations 44
2.4 From *extraversion* to eversion 48
2.4.1 Emergence of soft robotics 48
2.4.2 Technological diversification of eversion 53
2.4.3 Medical motivations for eversion 54
2.4.4 Principles and tools for eversion modeling 57
2.5 Preliminary experiment 61
2.6 Research Objectives and Contributions 66
3 Parametric Modeling of the Eversion-Based Robot **69**
3.1 A New Modeling Approach 71
3.1.1 Cosserat Rod Model 71
3.1.2 Fiber-based Geometric Representation 72
3.1.3 FEM Model 73
3.1.4 Hybrid Modeling through 1D/2D Coupling 74
3.1.5 Fiber-based Geometric Model 78
3.1.6 Definition of the FEM on the Fiber-based Geometry . . . 84
3.2 Preliminary Numerical Validation 89
3.2.1 Validation on eversion shapes 89

3.2.2 Validation in constrained environments 90
3.3 Conclusion 92
4 Modeling Elastic Wall Mechanics for an Everting Robot 95
4.1 Mesh geometry using fiber analogy 97
4.1.1 Principle & Requirements 97
4.1.2 Modeling 98
4.1.3 Implementation in SOFA 101
4.2 Mesh topology and thin-shell modeling 102
4.2.1 Principle & Requirements 102
4.2.2 Modeling 103
4.2.3 Implementation in SOFA 105
4.3 Eversion modeling 106
4.3.1 Principle & Requirements 106
4.3.2 Modeling 108
4.3.3 Implementation in SOFA 110
4.4 Conclusion 113
5 Design, control and experimental validation 117
5.1 Experimental System 118
5.1.1 Experimental Actuation System 119
5.1.2 Material Range 123
5.2 Experimental Evaluations 129
5.2.1 Material Inflation 129
5.2.2 Eversion under Unconstrained Conditions (Free deployment) 132
5.2.3 Eversion in a Constrained Environment 133
5.3 Preclinical validation 138
5.3.1 Mechanical Integration with the Delivery Channel 139
5.3.2 Autonomous Deployment and Control 141
5.3.3 Preclinical Evaluation in Biological Environments 145
5.4 Conclusion 148
6 Conclusion 151
6.1 Summary of Work and Contributions 151
6.2 Future Research Directions 153
6.3 Toward the Realization of a Complete TAVI Procedure 154
6.4 Perspectives and Clinical Translation 155
References 157
A Overview of SOFA's Mechanical Architecture 169
B Algorithms 171

C Bariatric Applications: Supplementary Studies **177**
C.1 Design and Preliminary Tests 178
C.2 Embedded Capsule 180
C.3 Conductive Inks 183
C.4 Conclusion 184
D Copyright Permissions **187**
D.1 Authorization to re-use Figure 2.5 188
D.2 Authorization to re-use Figure 2.7 189
D.3 Authorization to re-use Figure 2.7 190
D.4 Authorization to re-use Figure 2.7 191
D.5 Authorization to re-use Figure 2.7 192
D.6 Authorization to re-use Figure 2.8 193
D.7 Authorization to re-use Figure 2.9 194
D.8 Authorization to re-use Figure 2.9 195
D.9 Authorization to re-use Figure 2.9 196
D.10 Authorization to re-use Figure 2.9 197
Résumé en français **199**

List of Tables

3.1 Distribution of models according to the functional zones of the robot. 77

5.1 Characteristic pressures used for the robot experiments. 122
5.2 Characteristic pressurization thresholds in an unconstrained environment for the different membrane materials: initiation pressure P_i, stable eversion pressure P_e, rupture pressure P_r, and corresponding safety margin P_e/P_r. 124
5.3 Influence of the fused TPU cutting offset on the mechanical integrity of a robot. Critical pressures define the failure range, and rupture and deformation rates quantify the percentage of affected samples. 127
5.4 TPU and LDPE tubular sample properties. 129
5.5 Sensitivity analysis of the adjusted bending coefficient α on the predicted displacements. 131
5.6 (Top) Nominal Pressure (NP) and Rated Burst Pressure (RBP) of commercial coronary stents. (Bottom) Ratio between the crossing pressure P_c of the TPU robot and the nominal stent deployment pressure. 137

List of Figures

1.1 Illustration of the aortic valve function. (a) Normal aortic valve: the leaflets open widely during systole, allowing unobstructed blood flow, and close completely during diastole to prevent regurgitation. (b) Stenotic aortic valve: leaflet motion is impaired, resulting in incomplete opening during systole and incomplete closure during diastole. 28

2.1 Diagram illustrating the principle of Silverman's patented invention. A rigid housing contains a thin-walled flexible sheath folded back on itself. Controlled injection of a pressurized fluid causes the sheath to progressively turn inside out in a process called eversion. Progression within the cavity is facilitated by internal pressure and traction applied by a cord, without sliding or friction against surrounding tissues. 38

2.2 Principles of using eversion for atraumatic sampling or drainage. (a) The primary eversible tube guides a second thick-walled aspiration tube to the target site, where a negative pressure system enables fluid aspiration. (b) Another configuration features the everted sheath with an internal adhesive coating, allowing passive collection of secretions or microbial samples upon contact with the walls. (c) Localization devices, such as a marker or a graduated traction cord, allow the deployed length to be precisely associated with the sampling position along the anatomical pathway. 40

2.3 Principles of therapeutic administration by eversion. (a) The first approach involves coating the sheath with an active chemical substance, applied directly to the cavity walls during deployment. (b) The second configuration uses a perforated sheath allowing controlled diffusion of a drug or solution at the target site. 41

2.4 Intravascular applications of eversion deployment. The everted sheath enables controlled and centered delivery of an internal instrument through complex vascular segments while minimizing injury risk. (a) A flushing solution introduced into the annular space acts as a lubricant and reduces friction between the deployed wall and the internal instrument. (b) A dilatable sheath, designed as an expandable envelope, can be positioned at a stenosis and inflated to exert radial pressure and restore vessel diameter. 42

2.5 Controlled eversion deployment device. (a) Auxiliary table with all necessary equipment for manual pressure control and sterile filling. (b) Toposcopic catheter connected to a three-way stopcock for safe and atraumatic eversion. All images reproduced from Goldstein et al., (1980) [1] (a) and National Institutes of Health History of Medicine, (1979) [2] (b). 44

2.6 In vivo testing of the toposcopic catheter. (a) Catheter (arrows) ascending the left vertebral artery via the anterior spinal and basilar arteries to retrogradely access the internal carotid artery. (b) Catheter (arrows) in the hepatic branch of the left gastric artery, AP and lateral views with hepatic staining. (c) Angiogram showing a toposcopic catheter (arrow) at the tip of a dog's tongue, accessed via a branch of the external carotid artery. All images reproduced from Doppman et al. (1979) [3] and Goldstein et al. (1980) [1]. 47

2.7 Examples of technologies in soft robotics, including (a) materials such as shape-memory polymers [4] and liquid crystal elastomers [5], (b) actuation methods such as twisted-coil actuators [6] and hydraulic systems [7], and (c) fabrication processes such as molding [8] and additive manufacturing [9]. All images are reproduced from the respective publications cited for each example. 49

2.8 (a) A body elongates from its tip toward a target. As the tip advances, the body adopts the shape of the traversed path. (b) Examples of biological systems that grow to navigate their environment. Reproduced from Hawkes et al., 2017 [10]. 50

2.9 Timeline of key developments in the field of soft eversion-based robots from 2017 to the present time. Each year highlights notable contributions, including works by Hawkes et al. and Sadeghi et al. (2017) [10–12]; Blumenschein et al., Agharese et al., and Greer et al. (2018) [13–15]; Luong et al. and Abrar et al. (2019) [16, 17]; Takahashi et al., Jeong et al., and Satake et al. (2020) [18–20]; Kim et al., Takahashi et al., and Gruebele et al. (2021) [21–23]; Satake and Ishii and Hausladen et al. (2022) [24, 25]; Wu et al., Pi et al., and Jitosho et al. (2023) [26–28]; and recent advances in 2024 by Al-Dubooni et al., Satake et al., and Do et al. [29–31]. All images shown in the timeline are reproduced from the respective publications cited for each year. 52

2.10 Overview of eversion-based robot applications in different anatomical targets. Each entry indicates the first author, device diameter, and material. Studies are grouped by application domain: spinal navigation [32]; endovascular surgery [33–35]; colonoscopy [36–39]; mammary ductoscopy [26, 40–43]; bronchoscopy [44]; and intracranial neurosurgery [45]. All images are reproduced from the respective publications cited for each example. 56

2.11 Examples of simulated behaviors and scenarios generated by the simulator, based on a rigid-body, multi-link approximation of the eversion mechanism, including (a) growth, (b) bending, and (c) various contact interactions. Reproduced from Jitosho et al., 2021 [46]. 59

2.12 Examples of FEM-based simulations of the eversion mechanism using the SOFA framework, including (a) continuous deployment through internal pressurization and (b) detailed collision interactions in constrained environments. Reproduced from Wu et al., 2023 [42]. 60

2.13 (a) Automated preforming device with numerical control, equipped with a silicone syringe and a 15G nozzle, with a system of positioning and holding magnets. (b) Close-up view of silicone deposition on the first textile layer. 61

2.14 (a) Syringe pump injecting saline solution into the eversion-based robot, enabling generation and control of internal pressure. (b) Trial in a free environment showing the deployment of the preformed robot using a syringe pump, demonstrating continuous eversion along the programmed curvature. (c) Progression test in a rigid phantom reproducing an arterial pathway from the femoral artery to the aortic valve. 63

2.15 (a) Experimental setup of the cadaveric trial: eversion robot inserted into a 24F introducer and supplied with saline solution mixed with a contrast agent via syringe injection. (b) (1) View of the robot's progression in the femoral artery showing (2) the initial deviation at the level of a proximal stenosis, followed by (3) an arterial rupture on the femoral side, illustrating the constraints encountered when crossing pathological zones. 64

2.16 Methodological framework for the characterisation and optimisation of a fluid-eversion robot for safe and reliable endovascular deployment. Starting from clinical constraints identified in the context of TAVI navigation and the observed compliance limitations under fluid pressurisation, a predictive numerical model was developed and experimentally validated. The combined insights from modelling and experiments guided the parametric optimisation of material properties, geometry, and pressurisation conditions. An optimised robot was subsequently reconstructed and deployed under controlled conditions, followed by stepwise preclinical evaluation in progressively realistic vascular models. 67

3.1 Representation of the three functional zones of the growth-by-eversion robot: stored zone (contained material), eversion zone (turning inside out under pressurization), and deployed zone (externalized body in contact with the environment). 76

3.2 Fiber-based representation inspired by the geometric structure of Cosserat rod theory. (a) A single fiber showing its local reference frame and contribution to the robot's tubular envelope. (b) Arrangement of multiple fibers around the central axis, reconstructing the global geometry and kinematics of the robot. 76

3.3 Definition of the initial fiber arrangement at the robot base. The robot geometry is constructed from a set F of fibers F_i, uniformly distributed along a circular section of radius R in the transverse (y, z) plane. The global reference frame is defined such that the x-axis corresponds to the robot's deployment direction, while the (y, z) plane represents the base cross-section. Each fiber F_i is associated with an angle θ_{F_i} defining its position on the circle. The first node $N_{F_i,0}$ of each fiber lies on this circular section and serves as the fixed anchor point in the base plane. The schematic illustrates the notation used for boundary fibers (F_0, F_{F-1}) and intermediate ones (F_i), as well as their corresponding base nodes ($N_{F_0,0}$, $N_{F_i,0}$, $N_{F_{F-1},0}$). 79

3.4 Definition of the fiber discretization. Each fiber F_i, of total length L_{F_i}, is divided into a set S of sections $S_{F_i,j}$ with $j \in [0, S-1]$, connected by nodes $N_{F_i,j}$ with $j \in [0, S]$. The schematic illustrates the notation used for intermediate (j) and boundary indices (0, 1, $S-1$, S) along the fiber. 79

3.5 Fiber representation of the eversion zone. The fiber consists of sections $S_{F_i,j}$ connected by nodes $N_{F_i,j}$. The base is represented by $S_{F_i,0}$ and $N_{F_i,0}$. The eversion zone is represented by S_e, starting at $N_{F_i,BE}$ and ending at $N_{F_i,EE}$. 80

3.6 (a) The fiber of the robot is divided into three sections: $S_{F_i,0}$ (pre-eversion), $S_{F_i,1}$ (eversion), and $S_{F_i,2}$ (post-eversion). (b) Forward motion is obtained by increasing the distance between $N_{F_i,BE}$ and $N_{F_i,EE}$, which results in $S_{F_i,0}$ stretching and $S_{F_i,2}$ shrinking. (c) Conversely, backward motion is obtained by decreasing this distance, leading to $S_{F_i,0}$ shrinking and $S_{F_i,2}$ stretching. 81

3.7 Illustration of fiber deployment during the eversion motion simulated in SOFA. Panel (a) shows the initial stage of deployment at the onset of eversion, while panel (b) depicts the advanced stage, where the fibers are deployed. 84

3.8 The coupling model ensures the interaction between the fiber and the membrane. Rigid springs ($\mathbf{k}_k = 10^8$) are used in the kinematic zones, corresponding to the pre-eversion ($S_{F_i,0}$) and post-eversion ($S_{F_i,2}$) regions, in order to tightly constrain the FEM nodes to the prescribed kinematic motion. In contrast, the eversion zone ($S_{F_i,1}$) is treated as quasi-static: relaxed springs ($\mathbf{k}_k = 0$) are applied to allow the membrane to deform freely under elastic, pressure, and self-collision forces. This relaxation avoids over-constraining the system and enables natural eversion. 86

3.9 Illustration of mesh deployment during the eversion motion simulated in SOFA. Panel (a) shows the initial stage of deployment at the onset of eversion, while panel (b) depicts an advanced stage, where the mesh is deployed. 88

3.10 Reference eversion shapes experimentally observed in eversion-based robots : (a) random, (b) triangular, (c) linear. Shape (a) appears spontaneously, while shapes (b) and (c) result from specific storage or actuation conditions. 90

3.11 Numerical reconstruction of eversion shapes by combining elementary lengths $L_{e,\min}, L_{e,\text{mid}}, L_{e,\max}$. Three configurations are obtained: (a) random, with constant L_e; (b) triangular, produced by alternating contrasted lengths; (c) linear, built from a succession dominated by long sections framed by shorter segments. . . . 91

3.12 Simulation of the robot traversing a constrained passage: (a) identification of vertical section V_s and horizontal section H_s, (b) indication of the narrowing ratio τ_r and contact force F, (c) initial engagement phase of the robot into the slit, (d) complete passage through the constriction. 92

4.1 Fiber configurations defining the initial geometry of the eversion-based robot. Fibers serve as a temporary framework for shaping the future mesh. (a) The linear fiber configuration maintains a straight structure, while (b) the curved configuration introduces a predefined distal curvature. The robot is fixed to a base, reflecting its initial state in the simulation. 97

4.2 Schematic representation of the fiber-based robot structure. Each fiber F_i has a total length L_{F_i} and is discretized into $S_{F_i,j}$ sections, connected by nodes $N_{F_i,j}$, where $N_{F_i,0}$ is fixed at the base. When a distal curvature is introduced, the reference fiber F_0, positioned at y_{F_0}, is assigned a target curvature radius R_{C_0}. Each other fiber F_i is then evaluated relative to this reference in order to compute its own curvature radius R_{C_i}, arc length L_{C_i}, and curved sections $S_{C_i,j}$ composing the curved portion C_i. 99

4.3 Numerical implementation of the fiber-based geometry in SOFA. (a) Initial configuration of the eversion-based robot generated from the fiber analogy, with a predefined distal curvature ensuring a controlled and stable mesh discretization. (b) Validation test performed in a constrained tubular environment to verify the proper functioning of the collision module and the preservation of the preformed geometry with pressurization. 101

4.4 Numerical guide regulating the deployment of the membrane during eversion through dynamic zones. In the storage zone, the mesh is attached to the numerical guide by springs, ensuring its stability before deployment. As the mesh progresses, it enters the eversion zone, where the springs are released. 108

4.5 The numerical guide is composed of sub-guides G_i, each aligned with its corresponding mesh fiber F_i. The guide and the mesh are discretized into corresponding sections $S_{G_i,j}$ and $S_{F_i,j}$. Each node $N_{G_i,j}$ of the numerical guide is connected to its corresponding mesh node $N_{F_i,j}$ by springs whose stiffness varies according to their position: in the storage zone, high-stiffness springs ($\mathbf{k}_{1e9}$) prevent premature motion, while in the eversion zone, the stiffness progressively decreases to zero ($\mathbf{k}_0$) to enable controlled release of the elements. 110

4.6 The numerical visualization shows the guide frames ensuring the robot's deployment, the shell mesh representing the robot membrane, and the two functional zones governing its motion: the storage and the eversion zone. 112

4.7 Progressive eversion process from (a) to (c), where the storage zone gradually diminishes as the robot deploys. The advancing shell illustrates controlled membrane growth and the stable progression of the eversion front in a free environment. 112

4.8 Preliminary SOFA simulation of an eversion-based robot's deployment within the Pangolin phantom, a vascular model replicating the anatomical pathway from the femoral artery to the aortic valve. 114

5.1 The experimental setup includes a dual-syringe pump driven by a brushless DC (BLDC) motor and a lead screw mechanism to inject physiological saline solution into the reservoir. The pressure sensor is mounted on the first tube, which also serves as the fluid injection point. A widened 15mm (C-C section) diameter segment creates a passive air chamber that stabilizes internal pressure by damping fluctuations. The tubing then returns to 11 mm (A-A section) before narrowing to 8 mm at the robot base (B-B section), where the robot is immersed. Air bubbles are trapped at the interface between the 15 mm and 11 mm sections, contributing to pressure regulation during deployment. 119

5.2 (a) Global view of the setup, comprising the pressure sensor mounted on the reservoir inlet tube, the dual-syringe pump, the pressurized reservoir filled with saline solution, and the main injection site (reservoir port). (b) Detailed view of the reservoir port equipped with a three-way Luer lock stopcock, enabling three distinct connections: the storage inlet port for filling with saline solution, the syringe pump port for controlled injection, and the reservoir filling port ensuring hydraulic continuity during experiments. (c) A dynamic actuation module designed to generate sinusoidal pressure profiles, consisting of a self-centering plunger equipped with quad-ring seal, sliding along a linear rail within the reservoir to minimize friction. 121

5.3 The robot's geometry is first defined and transferred to a laser cutting device to shape the substrate. To achieve the desired internal diameter of 6 mm, the substrate is cut with a width of 9.42 mm between the cut edges. 125

5.4 Thermo-compression is performed between a first and a second TPU layer, with the substrate placed in between to define the robot's shape and limit heat diffusion during the process. 126

5.5 Evolution of the mechanical behavior of a TPU sample during pressurization: (a) initial state after complete eversion (⌀ = 6 mm), (b) uniform swelling phase (⌀ = 7.76 mm), (c) appearance of a localized deformation zone (⌀ = 10.01 mm), and (d) severe deformation phase, marking the onset of an irreversible regime that may lead to rupture. 127

5.6 After thermocompression, the robot shape is defined by the unfused TPU area. To ensure optimal sealing, the surrounding fused TPU is cut with an offset of approximately 2.04mm. 128

5.7 Correlation between simulated and experimental results for the inflation of TPU (a) and LDPE (b) meshes under applied pressure. The mean deviation between simulation results and experimental data is 0.46 mm for TPU and 0.01 mm for LDPE, with consistent deviations in both cases. 130

5.8 (a) For TPU, a small eversion zone (5% of total length) leads to localized stress concentrations and fluctuations ($\bar{x}$ = 0.045 mm, σ_x = 0.021 mm), whereas a large zone (50%) induces oscillations and loss of guidance ($\bar{x}$ = 0.055 mm, σ_x = 0.044 mm). An intermediate zone (20%) minimizes instabilities ($\bar{x}$ = 0.048 mm, σ_x = 0.018 mm). (b) For LDPE, a 10% eversion zone optimizes stability ($\bar{x}$ = 0.049 mm, σ_x = 0.019 mm). 133

5.9 Comparison between simulated and experimental behavior of the LDPE robot in a 5 mm stenosis, where eversion failure is observed in both cases. The simulation exhibits a non-physical double-growth effect, with mesh progression occurring without distal displacement. Experimentally, excessive pressure causes upstream swelling and rupture, leading to leakage. 135

5.10 Comparison between simulated and experimental deformation profiles of the 6 mm-diameter TPU robot during eversion in stenotic geometries. In both cases, traversal is successful for constrictions of 5 mm and 4 mm. The simulation shows contact-induced bending without radial expansion, indicating geometric adaptation to the lumen. In contrast, the experiment reveals upstream swelling, particularly pronounced in the 4 mm case due to higher internal pressure, leading to temporary or irreversible mesh deformation. . 136

5.11 Sealing interface between a PU microtube and the TPU robot. The microtube is thermally bonded to the distal end of the TPU robot, forming a robust sealing interface. 139

5.12 (a) Dynamic occlusion module using a silicone tube connected to two distinct parts: a fixed section and a rotating section. (b) To ensure sealing, the rotating part performs a 900° rotation, inducing controlled torsion of the silicone tube. This blocks fluid passage around the channel while allowing its longitudinal movement. . . 140

5.13 (a) Drive system composed of servomotors actuating opposing PU wheels, ensuring controlled longitudinal displacement of the channel. (b) Occlusion module in operational configuration, integrating a centering hole to maintain alignment during motion. (c) Module in open state, allowing free passage of the channel. (d) Module in closed state, providing effective sealing under internal pressurization. 141

5.14 Autonomous deployment of the eversion-based robot within a dynamic vascular phantom reproducing the iliac–aortic pathway. The TPU eversion-based robot progresses from the femoral artery bifurcation to the aortic valve (∼600 mm), following the preformed curvature of the phantom, including a 50 mm radius at the aortic arch. 142

5.15 (a) The system includes a reservoir in which the robot body is stored prior to deployment. This reservoir is pressurized by a syringe pump module driven by a BLDC motor, allowing continuous fluid injection from an external tank. Internal pressure is monitored and regulated by a pressure sensor, ensuring stable and controlled eversion of the robot from its base station. In parallel, a channel guidance mechanism, actuated by servomotors, ensures synchronized advancement of the channel fixed to the distal end of the robot, maintaining coordinated motion throughout deployment. The entire system operates within a silicone phantom reproducing the geometry and compliance of the vascular environment. Electronic control units drive the actuators and sensors, providing precise regulation and data acquisition. (b) The system operates under a closed-loop control scheme based on a proportional controller. The measured internal pressure is continuously compared to a fixed setpoint (18 kPa). When the pressure drops below the setpoint, the syringe pump driven by the BLDC motor injects additional fluid; conversely, when the pressure exceeds the setpoint, the servomotor-driven channel guidance mechanism advances to increase the internal volume and reduce pressure. 143

5.16 Autonomous deployment of the eversion-based robot within a dynamic vascular phantom reproducing the iliac–aortic pathway. A central lumen is maintained throughout the robot body, allowing guidewire insertion once the robot reaches its final position at the aortic valve. 144

5.17 (a) Actuation system implemented on the cadaveric model, integrating the pressurization reservoir and the control unit, used to assess the feasibility of eversion within a human vascular anatomy. (b) Introduction of the eversion-based robot directly into the femoral artery, surgically exposed for access, and connected to the base station and the reservoir filled with saline solution and contrast agent. 145

5.18 (a) Actuation system implemented on the porcine model, integrating the pressurization reservoir and the control unit, used to evaluate eversion feasibility under physiological conditions. (b) Femoral access of the robot through a standard 20 Fr (6.7 mm) introducer, connected to the base station and to the reservoir filled with saline solution and contrast agent. 145
5.19 Anatomical tests reconstructed from combined fluoroscopic views. (a) Progression of the robot in the porcine model, from the introducer positioned in the femoral artery up to the proximal segment of the aortic arch. (b) Deployment in a human cadaver, advancing from the femoral artery to the iliac region. 147
5.20 Post-deployment analysis on the porcine model showing the eversion-based robot on its base station, connected to the channel via the PU microtube. A leak was observed at the TPU junction, highlighting the structural weakness of the fusion line and leading to localized robot failure. 147

C.1 (a) First prototype of a 15 mm LDPE eversion-based robot equipped with a support capsule integrating an endoscopic camera and biopsy forceps, with air inlet connected to the pressurization box. (b) Sealing failure observed during the test, with rupture occurring at the welded edges after approximately 10 cm of deployment. 180
C.2 Prototype of the embedded electronic capsule integrating sensing, communication, and control electronics: (a) complete capsule, (b) upper side of the PCB, and (c) lower side of the PCB. 181
C.3 Conductive patterns printed on a Pellethane substrate using the Voltera V-One printer and SEFlex conductive ink. (a) Plastic film positioned on the Voltera printing platform, (b) microscopic view of the SEFlex ink deposited on the TPU surface, and (c) final printed track demonstrating the good solderability of the ink with tin. 183

Acronyms

FEM Finite Element Method. 15, 18, 59, 60, 73, 75, 77, 82, 84–87, 117, 172, 200, 202

LDPE Low Density Polyethylene. 21, 69, 71, 87, 90, 93, 123–125, 128–130, 133–135, 138, 148, 149

PTFE Polytetrafluoroethylene. 123, 124, 138

PU Polyurethane. 22, 24, 139–141, 147, 149

SOFA Simulation Open Framework Architecture. 15, 17, 18, 20, 59, 60, 66, 82, 84, 88, 101, 105, 110, 114, 171–175

TAVI Transcatheter Aortic Valve Implantation. 16, 28–30, 61, 62, 65–67, 69, 117, 134, 137, 138, 148, 151, 154, 155

TPU Thermoplastic Polyurethane. 11, 21, 22, 24, 69, 71, 123–130, 132–139, 142, 146–149, 154, 179

Chapter 1

Introduction

In the architecture of the human cardiovascular system, aortic stenosis stands out as the most common valvular disease [47], with a prevalence that increases markedly with population aging. The aortic valve, located between the left ventricle and the aorta, opens with each heartbeat to allow blood to flow freely (Figure-1.1.a). In the case of stenosis, this opening progressively narrows, turning what is normally a wide and flexible passage into a rigid and narrow conduit that significantly impedes blood flow (Figure-1.1.b). To maintain an adequate output, the left ventricle must then generate much higher pressure to force blood through the narrowed orifice. This overload leads to a progressive thickening of its muscular wall. While this mechanism initially compensates for the obstruction, it is accompanied by a loss of compliance that alters filling between beats. At an advanced stage, this rigidity even compromises the ventricle's contractile capacity, resulting in left ventricular dysfunction. For a long time, the standard treatment for this condition was surgical replacement of the aortic valve. Performed through a sternotomy with the use of cardiopulmonary bypass, this procedure involved removing the calcified native valve and replacing it with a mechanical or biological prosthesis sutured to the aortic annulus. Although this technique achieved excellent outcomes, its highly invasive nature limited access to a minority of carefully selected patients, excluding most elderly or multi-morbid individuals.

It was in this context of therapeutic need that Alain Cribier proposed, in the early 1990s, a then-unprecedented approach [48]: replacing the aortic valve with-

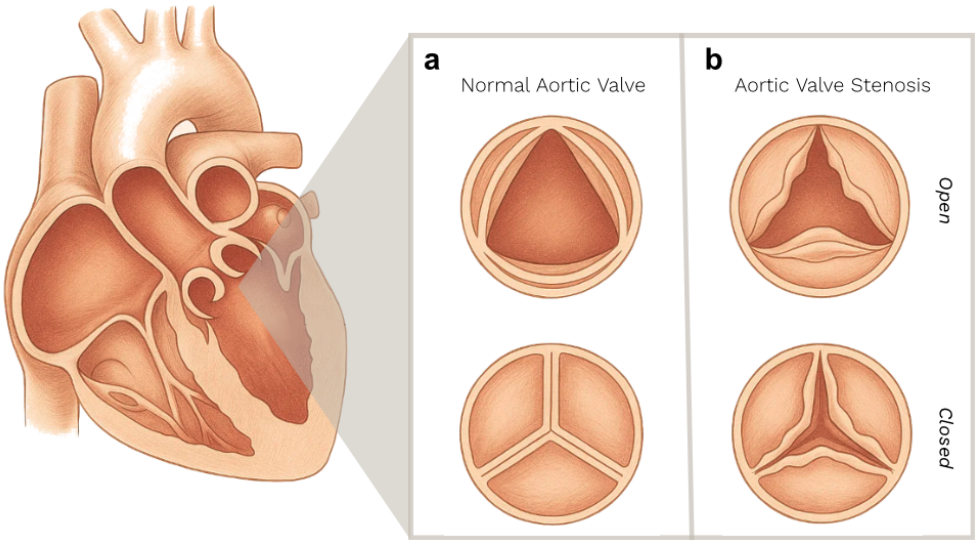


Figure 1.1: Illustration of the aortic valve function. (a) Normal aortic valve: the leaflets open widely during systole, allowing unobstructed blood flow, and close completely during diastole to prevent regurgitation. (b) Stenotic aortic valve: leaflet motion is impaired, resulting in incomplete opening during systole and incomplete closure during diastole.

out thoracotomy by developing a prosthesis specifically designed to be crimped, delivered via catheter, and deployed directly within the heart. To pursue this development, Cribier co-founded the start-up Percutaneous Valve Technologies, with the support of an Israeli investor who provided funding for the initial design and experimental validation phases. After more than ten years of development and preclinical trials, the goal was achieved: in April 2002, the first successful percutaneous implantation of an aortic valve in a human was performed in Rouen [49]. Delivered through the venous route and deployed using a balloon, this procedure marked the birth of a new therapeutic approach: the Transcatheter Aortic Valve Implantation (TAVI) procedure. Two years after this landmark achievement, Percutaneous Valve Technologies was acquired by Edwards Lifesciences, paving the way for industrialization and optimization of the technology. This transition to a larger scale enabled a thorough redesign not only of the valve prostheses but also of the delivery systems required for their implantation. Among these innovations, the *RetroFlex* device, introduced around 2006, represented a decisive breakthrough. More compact and adjustable, it facilitated navigation through the vascular tree and allowed for more precise prosthesis deployment, thus expanding access to the valvular site. While the first implantations relied on

a more complex and invasive transseptal approach, the introduction of *RetroFlex* made a different strategy possible: the transfemoral route. By enabling access to the valve through a simple puncture of the femoral artery, this new approach significantly reduced the invasiveness of the procedure and simplified the intervention. Clinical validation of this technique by Dr. John Webb [50] confirmed its relevance and contributed to establishing transfemoral access not only as a credible alternative but gradually as the preferred access strategy.

In parallel, prostheses and delivery systems continued to evolve. The reduction of introducer sizes, the development of valves of various sizes and repositionable designs, as well as improved catheter ergonomics, simplified procedures and reduced risks, making TAVI accessible to an increasing number of patients.

Initially reserved for inoperable patients, TAVI indications quickly expanded thanks to technical progress and accumulating clinical evidence. Starting in 2011, several randomized trials validated its effectiveness in different patient populations. The *PARTNER 1* study first demonstrated that, in inoperable patients, TAVI significantly improved survival compared with medical therapy alone [51]. Other trials, such as *SURTAVI* and *U.S. CoreValve High Risk Study*, later showed that the procedure could be performed safely in patients with intermediate surgical risk, with outcomes comparable to those of surgery [52, 53].

In 2019, two landmark studies — *PARTNER 3* and *Evolut Low Risk* — marked a new turning point [54, 55]. They demonstrated that TAVI could be safely offered to patients considered at low surgical risk. The results were comparable to those of open-heart surgery and, on certain short-term criteria such as recovery or early complications, were even superior. This milestone made it possible to extend TAVI use well beyond frail or high-risk patients, progressively transforming the management of aortic stenosis into a truly multimodal approach adapted to increasingly diverse patient profiles.

Today, more than one million TAVI procedures have been performed worldwide, making this technique a therapeutic standard in many countries. However, major technical challenges remain: navigating rigid catheters through tortuous, calcified, or stenotic arteries continues to be a major source of complications. Risks of vascular perforation, dissection, or displacement of atherosclerotic plaques still expose some patients to serious adverse events, particularly embolic strokes. These

mechanical limitations highlight the need for exploring more flexible and adaptive solutions, capable of navigating the vascular environment with enhanced safety, without compromising procedural precision or valve deployment efficacy.

Research Objectives

It is precisely in this context that the development of a soft robot, named an eversion-based robot, was initiated. Actuated by fluid for clinical safety and based on the principle of eversion, it is specifically designed for navigation within the vascular system during minimally invasive procedures such as TAVI. Unlike traditional catheters, this robot advances by progressively turning inside out from its distal end, allowing it to follow tortuous anatomical pathways with minimal contact forces and reach otherwise inaccessible areas without trauma. This thesis is dedicated to the design, simulation, control, and experimental validation of this new robotic architecture, aiming to enable safer and more effective navigation during TAVI procedures. The structure of the manuscript is as follows:

Chapter 2 traces the evolution of eversion-based devices, from the earliest patents to modern eversion-based robots, highlighting their biomedical applications and advances in soft robotics. It also provides a synthesis of the modeling approaches used to predict and optimize their behavior. Some hardware configurations reported in the literature were subsequently transposed into an experimental framework through preliminary tests. These trials revealed significant limitations of such approaches when applied to the specific problem addressed, thereby guiding the developments presented in the remainder of the manuscript.

Chapter 3 introduces the numerical modeling framework developed to simulate the robot's eversion process. It presents an initial parameterization approach based on a hybrid representation that combines a fiber-based geometric model with the finite element method. Implemented within the Simulation Open Framework Architecture (SOFA), this model enables a simplified formulation of the eversion process and predicts deformations and contact interactions.

Chapter 4 refines the previously developed model by integrating a thin-shell formulation within the framework of the finite element method. This representation

enables a more accurate description of the physical effects involved in eversion, such as local bending, membrane tension, and complex contact. The objective of this chapter is to improve the accuracy of numerical predictions and to strengthen the mechanical foundations of the model before its experimental validation.

Chapter 5 focuses on the hardware design of the robot and on its experimental validation, comparing the predictions of the numerical model developed in Chapter 4 with measurements obtained on a dedicated test bench. This validation confirms the consistency between the simulated and observed behaviors, particularly in terms of deformation, stability, and pressurization response. Based on this cross-validation, a mechanical characterization of the materials was carried out to identify the most suitable one for the robot's fabrication. The tests showed the superiority of thermoplastic polyurethane, which demonstrated greater flexibility and stability under stress. On this basis, operational prototypes were developed, enabling full navigation through anatomical phantoms, including the passage of an instrument through the robot's inner channel. Finally, preliminary trials conducted on a human cadaver model and an in vivo porcine model allowed the evaluation of the robot's behavior under realistic physiological conditions, highlighting areas of structural fragility while confirming the overall relevance of the concept for future biomedical translation.

Chapter 6 provides a synthesis of the main contributions and limitations of this thesis, while outlining several directions for future research. It emphasizes the need to enhance the structural reliability of the robot, and to refine the numerical model to better capture tissue–robot interactions, vascular compliance, and the nonlinear behavior of the material. The chapter also highlights the development of more adaptive control strategies, supported by embedded sensing for real-time feedback. Finally, it discusses the clinical integration prospects of the robot, including its adaptation to surgical environments and its potential extension to other minimally invasive procedures.

Publications

The following publications are associated with the work accomplished during the PhD. The publications are grouped in categories such as journal or conference

and ranked first by authorship and then by year of publication.

Publications in international conferences:

– **Przybylski, F.**, Adagolodjo, Y., Dequidt, Duriez, C., and Berthet-Rayne, P., "Enhancing TAVI Robot Flexibility Using Semi-Extensible Materials", In Hamlyn Symposium on Medical Robotics (HSMR), 2024.

– **Przybylski, F.**, Adagolodjo, Y., Cerruti, G., Mîra, A., Dequidt, Duriez, C., and Berthet-Rayne, P., "3D kinematics and quasi-statics of a growing robot eversion", In IEEE International Conference on Soft Robotics (RoboSoft), 2023.

Workshop Participation:

– **Przybylski, F.**, and Berthet-Rayne, P., "Growing robots in endovascular surgery: from Lab to cadaver", In IEEE International Conference on Robotics and Automation (ICRA), Workshop on Soft Growing Robots: From Search-and-Rescue to Intraluminal Interventions, 2023.

Poster Presentations:

– **Przybylski, F.**, Adagolodjo, Y., Dequidt, Duriez, C., and Berthet-Rayne, P., "Design, modeling and development of a flexible surgical endoscopic robot", 11^{th} Summer School on Surgical Robotics, Montpellier, 2023.

– **Przybylski, F.**, Adagolodjo, Y., Cerruti, G., Mîra, A., Dequidt, Duriez, C., and Berthet-Rayne, P., "3D kinematics and quasi-statics of a growing robot eversion", IEEE International Conference on Robotics and Automation (ICRA), Workshop on Soft Growing Robots: From Search-and-Rescue to Intraluminal Interventions, 2023.

Patents:

– **Przybylski F.**, Berthet-Rayne P., Sejor E., Smits J., and Mira A., *Insertion instrument for insertion into a cavity*, Filed 21-12-2022, International Publica-

tion Number WO 2023/118322 A1

– Berthet-Rayne P., **Przybylski F.**, Sahafi A., and Perard L., *Insertion instrument, system comprising the insertion instrument and process for manufacturing the insertion instrument*, Filed 19-09-2023, International Publication Number WO 2024/074298 A1

– Berthet-Rayne P., Smits J., Sejor E., Mialhe C., **Przybylski F.**, and Benoist C., *Surgical access port, system and method comprising a surgical access port*, Filed 05-05-2023, International Publication Number WO 2023/214007 A1

Chapter 2

From Catheter to Soft Robotics

The introduction of medical instruments into the internal cavities of the human body, whether blood vessels, urinary tracts, or the digestive system, relies on the use of rigid or semi-flexible catheters. However, these devices present several fundamental limitations that hinder their effectiveness and safety in complex anatomical environments. A first obstacle concerns the friction generated by the sliding of the catheter against the cavity walls. This prolonged contact, necessary to advance the instrument over long distances, can cause pain, discomfort, and, in some cases, cavity injury. Such trauma is particularly problematic in sensitive or already pathological structures.

Navigation through narrow, tortuous, or highly curved pathways constitutes a second obstacle. Physicians are faced with a trade-off between rigid catheters, which provide axial stiffness but lack the flexibility required to follow complex geometries, and soft catheters, which can bend but often fail to maintain sufficient axial rigidity. In the latter case, the device may kink, fold, or collapse under pushing forces, making its progression unpredictable or even impossible in certain conditions.

Added to these issues are increased risks of contamination and loss of sterility, as catheters can be exposed to microorganisms during handling and may promote bacterial migration along mucous membranes [56]. These risks are mitigated through strict aseptic practices and device designs that limit contact and manipulation.

In this context, eversion-based soft robots have emerged as a promising alternative, offering reduced friction, distributed contact forces, and the ability to navigate complex geometries through tip growth rather than global pushing. Over the past decade, significant developments have been made both in hardware design and in modelling strategies aimed at understanding and predicting their behaviour.

This chapter therefore provides a structured overview of these developments, covering both technological implementations and modelling approaches. Beyond a descriptive state-of-the-art analysis, its objective is to identify the physical and technological limitations that arise when transitioning from laboratory prototypes to realistic medical environments. As will be discussed, preliminary investigations and cadaveric trials revealed a critical issue related to compliance under fluid actuation in constrained endovascular conditions. This observation constitutes the scientific starting point of the present work.

2.1 Early explorations toward atraumatic navigation [1]

Faced with the limitations of traditional catheters, inventors of the 20th century sought to design alternatives that were more tissue-friendly and better adapted to anatomical constraints. Although these early devices cannot yet be described as robots or complex active systems, they clearly reflect an intention to introduce greater flexibility and control in accessing internal cavities.

In the early twentieth century, several patents explored the use of fluid pressure, whether air or liquid, to actuate internal elements within the body. In 1905, U.S. Patent US805851A [57] introduced a drug injector equipped with a soft membrane actuated by a pneumatic bulb. Designed for use in the throat or vagina, this system enabled the administration of a substance without any rigid

[1] A large number of early attempts to improve catheter-based devices were disclosed through patents rather than scientific publications. As a result, these contributions are often overlooked in recent surveys on soft robotics. In the context of this CIFRE PhD, however, the study of patents proved essential. It enabled us to reconstruct the historical progression of developments, particularly those based on the principle of eversion.

component coming into contact with the cavity walls.

Three years later, German Patent DE215350C (1908) described a device intended for exploring deep cavities such as the esophagus. It used a thin folded membrane housed within an introducer, which, once inserted, was deployed by internal pressure, ensuring gentle contact with the walls without rigid mechanical extension.

Closer to modern clinical applications, U.S. Patent US2847997A (1958) [58] introduced a nasal catheter equipped with an inflatable balloon covered in hemostatic gauze. Once positioned and inflated, this system enabled localized treatment without aggressive manipulation, thereby reducing pain and the risk of irritation.

In parallel with these systems, efforts were also directed toward the design and manufacture of flexible tubing in general. Patents such as US1956722A (1934) [59] and US2925021A (1960) [60] described processes for manufacturing and coating rubber or latex tubes aimed at strengthening their mechanical resistance while maintaining thinness and flexibility. These material innovations paved the way for the development of sheaths capable of bending, folding or stretching without losing their integrity, an essential quality for achieving gentle navigation in deep, tortuous anatomical structures.

Despite their limited scope, these inventions laid the foundations for a softer and more anatomically adapted approach to internal navigation. They all share the same technical intuition: rather than forcing a rigid body into tissues, it is possible to deploy flexible structures actuated remotely to accomplish the task. However, at this stage, one essential limitation remained: none of these proposals yet offered a mechanism for continuous progression or a solution for actively and atraumatically controlling advancement within the cavity.

2.2 Silverman's conceptual breakthrough

In continuity with the devices described in Section 2.1, Daniel Silverman filed in 1963 a patent (U.S. Patent US3168092A [61]) that, to our knowledge, constitutes the first formal description of a catheter based on the principle of membrane turning. The invention relies on what Silverman termed *extraversion*: a thin-walled,

flexible tube that progressively turns inside out under internal pressure, thus advancing without sliding or friction against the cavity walls. This terminology differs from the more commonly used term *eversion*, although both refer to the same physical phenomenon of a structure unfolding by turning inside out. The mechanism offers several advantages: it maintains sterility of the internal surface, prevents tissue injury caused by friction, and naturally conforms to complex anatomical geometries.

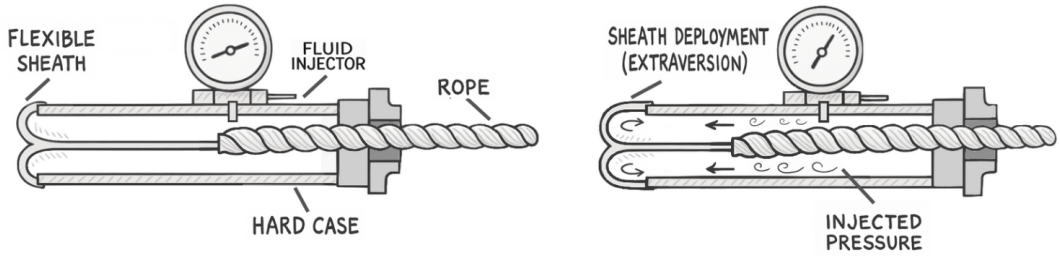


Figure 2.1: Diagram illustrating the principle of Silverman's patented invention. A rigid housing contains a thin-walled flexible sheath folded back on itself. Controlled injection of a pressurized fluid causes the sheath to progressively turn inside out in a process called eversion. Progression within the cavity is facilitated by internal pressure and traction applied by a cord, without sliding or friction against surrounding tissues.

Concretely, the system consists of a rigid cylindrical housing containing a thin-walled, flexible, airtight tube folded back on itself (Figure 2.1). One end of the tube is fixed to the opening of the housing, while the rest is attached to a cord enabling controlled traction from outside. When a fluid, either air or liquid, is injected into the housing, the pressure applied to the internal walls of the tube initiates its turning inside out, referred to as eversion in the patent. The deployed sheath then progresses into the target cavity, driven by internal pressure and the traction of the cord, without axial translation of the housing and without sliding against surrounding tissues.

2.3 The legacy of a principle

The principle of *extraversion* proposed by Silverman was subsequently developed along two distinct paths. On one hand, several patents proposed targeted adap-

tations, modifying the original concept for specific clinical applications or by adjusting certain mechanical aspects. On the other hand, research teams conducted experimental studies to evaluate this deployment method, first on bench models and later on biological models.

2.3.1 Technological variants from patents

Drainage and sampling devices

Extraversion proved particularly effective for the atraumatic introduction of flexible instruments for sampling or aspiration into anatomically challenging cavities. This approach enables the insertion of small-caliber tubes intended for fluid drainage or sample collection without the need for direct mechanical pushing (Figure 2.2).

In one configuration, a second thick-walled tube inserted inside the primary eversible tube is guided to the target site through the deployment of the primary tube. Applying negative pressure at its external end then allows fluid aspiration. This principle was notably used for nasogastric drainage, leading to a significant reduction in irritation compared with conventionally inserted devices [61–63].

Another variant relies on passive collection at the surface of the everted sheath. Initially internal, this surface can be coated with an adhesive or absorbent material to capture tissues, secretions, or microbial agents upon contact with the walls. This method was explored for urethral bacterial sampling, with multi-segmented designs adapted to the conduit's geometry [61, 64].

An additional advantage of this technology lies in the spatial precision it enables. By controlling the length of the deployed tube, each sample can be associated with a specific position along the pathway. Indirect measurement devices such as traction cords, markings or optical systems were proposed to enhance this localization capability [61, 64].

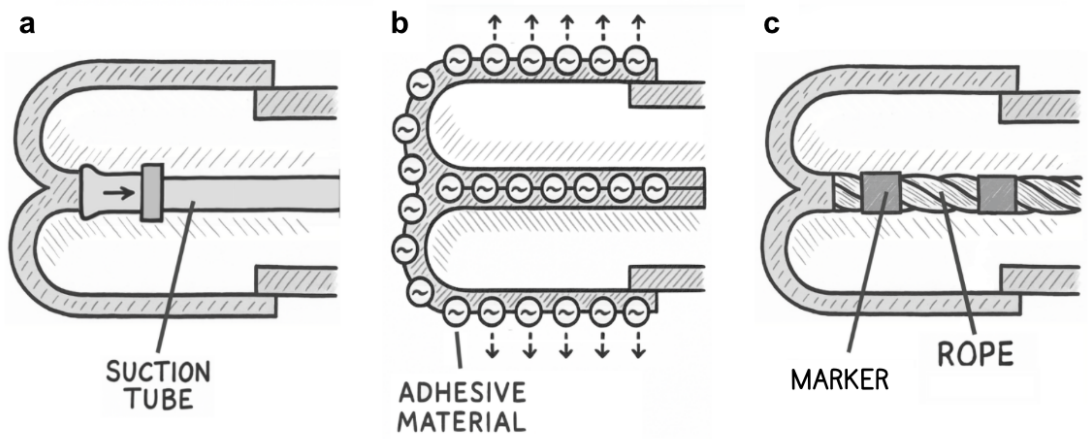


Figure 2.2: Principles of using eversion for atraumatic sampling or drainage. (a) The primary eversible tube guides a second thick-walled aspiration tube to the target site, where a negative pressure system enables fluid aspiration. (b) Another configuration features the everted sheath with an internal adhesive coating, allowing passive collection of secretions or microbial samples upon contact with the walls. (c) Localization devices, such as a marker or a graduated traction cord, allow the deployed length to be precisely associated with the sampling position along the anatomical pathway.

Systems for therapeutic delivery

Beyond sampling and drainage functions, several variants explored the potential of the *everted* tube as a vehicle for localized treatment. Thanks to its atraumatic insertion method and the sterile surface it deploys in contact with tissues, the device naturally lends itself to the targeted administration of therapeutic agents.

Two main approaches were developed. The first involves coating the inner surface (which becomes external during *extraversion*) with active substances such as chemical, antiseptic or radioactive agents to directly treat the cavity walls [61]. The second relies on using a secondary tube with a permeable or perforated wall, capable of delivering a drug or solution to the site of interest [65] (Figure 2.3).

Controlled deployment in the vascular system

The principle of *extraversion* was also adapted for intravascular applications, where the requirements for control, centering, and atraumatic insertion are par-

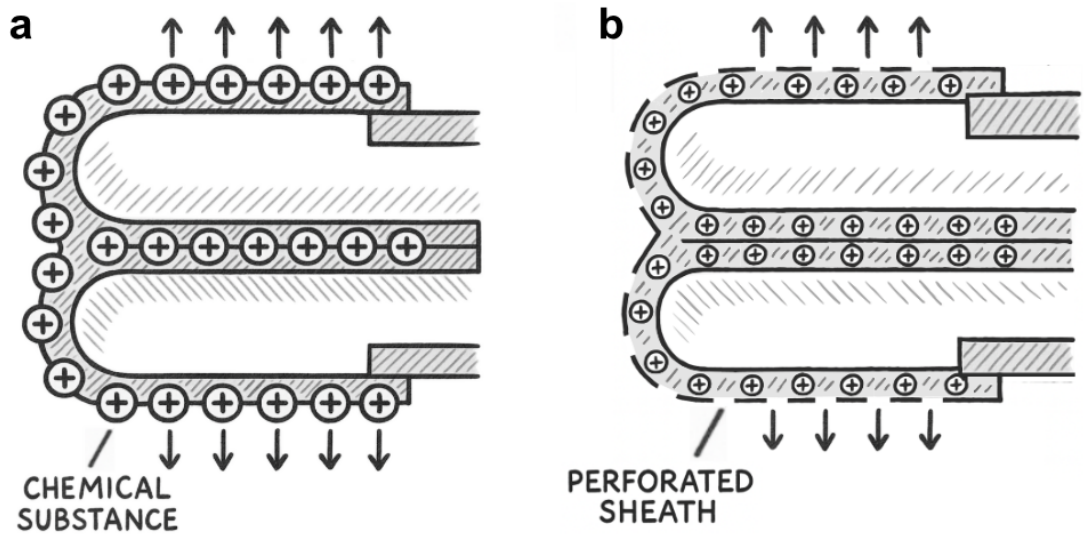


Figure 2.3: Principles of therapeutic administration by eversion. (a) The first approach involves coating the sheath with an active chemical substance, applied directly to the cavity walls during deployment. (b) The second configuration uses a perforated sheath allowing controlled diffusion of a drug or solution at the target site.

ticularly strict. Several devices applied this mechanism to navigate the vascular network, where the combination of small diameter, fragile walls and sharp curvatures makes the introduction of conventional instruments particularly challenging. In this context, the *everted* tube enables the gentle and stable delivery of a catheter, guidewire, or therapeutic device through complex segments while significantly reducing the risk of endoluminal injury.

However, inserting an internal element into the *everted* sheath presents a specific challenge: once deployed, the tube wall tends to adhere to the guided instrument, making independent movement difficult. This internal friction can limit position adjustments, particularly during procedures requiring active navigation or localized intervention.

To overcome this limitation, several patents proposed introducing a flushing solution (saline, contrast agent, etc.) into the annular space between the everted sheath and the internal instrument (Figure 2.4). This solution serves a dual purpose: acting as a lubricant to reduce friction and creating a fluid separation layer that enables longitudinal or axial displacement of the instrument without mechanical adherence to the wall. Some versions integrate specific geometries,

such as axial grooves or helical channels, to facilitate fluid circulation along the sheath [66–68].

Beyond assisted navigation, these devices were adapted for targeted therapeutic applications, notably in the treatment of vascular stenoses. The principle involves everting the distal section of the tube, or a segment specifically designed as an inflatable balloon, to the narrowing site. Once positioned, this element is expanded by injecting a fluid, either air or liquid, exerting radial pressure on the vessel wall to restore the conduit's diameter (Figure 2.4). *Extraversion* here enables atraumatic positioning of the dilatable element, reducing the pushing forces and risks of injury associated with traditional dilation techniques [67, 69].

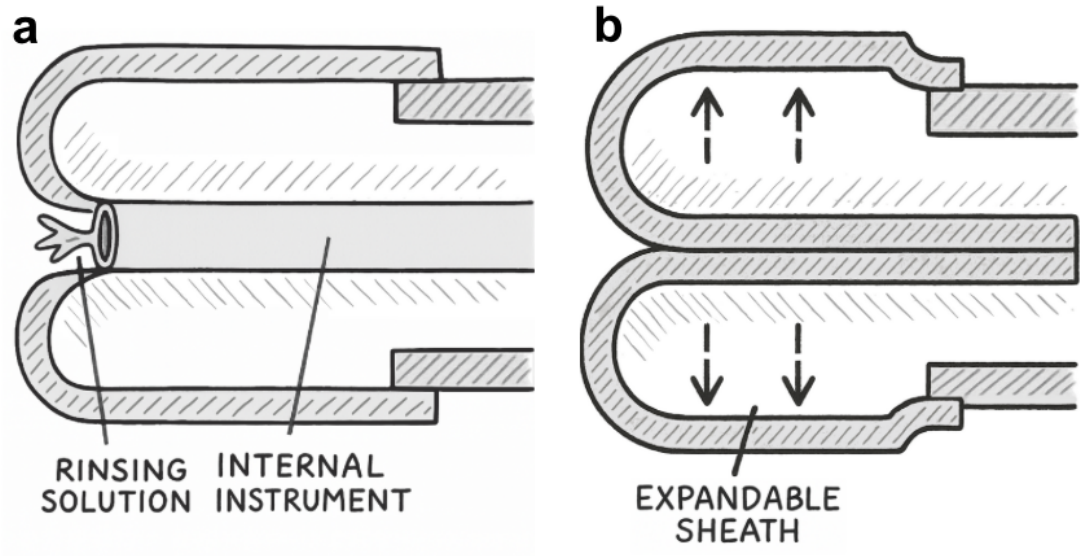


Figure 2.4: Intravascular applications of eversion deployment. The everted sheath enables controlled and centered delivery of an internal instrument through complex vascular segments while minimizing injury risk. (a) A flushing solution introduced into the annular space acts as a lubricant and reduces friction between the deployed wall and the internal instrument. (b) A dilatable sheath, designed as an expandable envelope, can be positioned at a stenosis and inflated to exert radial pressure and restore vessel diameter.

Mechanical enhancements

While early patents mainly focused on diagnostic or therapeutic uses of the *everted* tube, several subsequent developments aimed to mechanically optimize the

device. The goal was to increase its robustness in demanding clinical contexts and refine the control of *extraversion* and *introversion* kinematics. In Silverman's terminology, *extraversion* refers to the unfolding of the tube by turning inside out, whereas *introversion* designates the reverse process, namely its controlled retraction for atraumatic withdrawal.

A first set of improvements targeted the deployment mechanism itself. Some devices, for example, proposed initiating or facilitating tube eversion using an internal element, such as a rod, tube or piston, that mechanically displaces the fluid contained in the housing. This approach reduces the pressure required for eversion and facilitates its use in constrained environments [64, 66, 68, 70].

Other patents have focused on tube dynamics during deployment. By modulating the device's geometry, particularly through variations in wall thickness along its entire length, it becomes possible to influence *introversion* behavior. Reinforced segments act as return zones, stabilizing retraction or imposing predefined folding patterns [61, 64].

These geometric refinements led to reconsidering the materials used for the *evertable* membrane. Early models primarily relied on natural elastomers such as rubber or latex, chosen for their flexibility and ability to invert without tearing. Some devices even integrated internal coatings to improve the sealing of woven structures [71].

With evolving clinical needs, thermoplastic materials such as polyethylene, polypropylene, and polyurethane were introduced for membrane manufacturing. This choice appears to be motivated by the search for improved dimensional stability, enhanced durability, and compatibility with biological environments [63, 71–73].

The adoption of new materials was accompanied by innovations in assembly methods. Adhesive bonding was commonly used to join flexible components to rigid parts, while mechanical solutions such as compression rings ensured junction sealing through simple radial tightening [62, 74].

Finally, some devices used thermoforming processes with a dual purpose. On one hand, they strengthened bonds between different types of components by ensuring a continuous material transition. On the other hand, they enabled the membrane to adopt predefined geometries, such as curvature, helical shapes or transverse

bending, using shape-memory materials like polypropylene. Once activated, these structured forms helped guide the trajectory or stabilize the tube's position within the cavity [64, 73, 75].

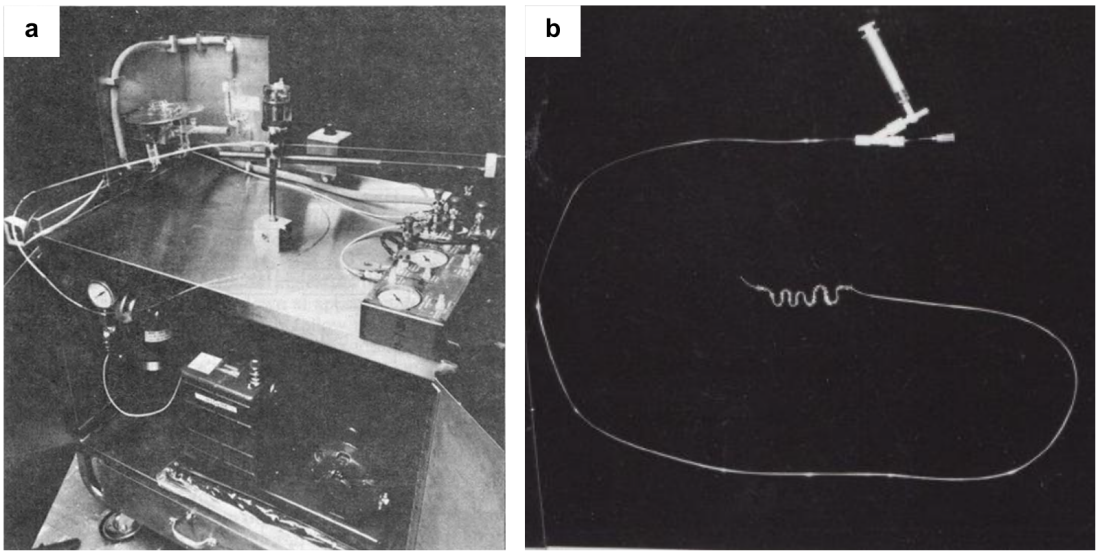


Figure 2.5: Controlled eversion deployment device. (a) Auxiliary table with all necessary equipment for manual pressure control and sterile filling. (b) Toposcopic catheter connected to a three-way stopcock for safe and atraumatic eversion. All images reproduced from Goldstein et al., (1980) [1] (a) and National Institutes of Health History of Medicine, (1979) [2] (b).

2.3.2 Experimental biomedical investigations

Despite the proliferation of patents proposing a wide range of clinical applications and mechanical improvements, these advances largely remained at the stage of conceptual development and preliminary experimentation, without extending to patient testing. To bridge this gap, in 1979, a team developed a controlled-*extraversion* catheter, later referred to as the toposcopic catheter, to experimentally assess the initial promises of the concept for endovascular navigation [1, 3, 76].

The main challenge was to facilitate progression through particularly tortuous or small-caliber vascular segments, while ensuring therapeutic delivery and localized fluid sampling, without increasing the risks of friction, vasospasm, or dissection. To achieve these objectives, several technical barriers had to be overcome:

miniaturizing the mechanism to adapt it to a small diameter while maintaining robustness; controlling internal friction between successive membranes to enable smooth deployment without sliding; and finally, ensuring precise guidance and adaptability of the device to the variety of targeted anatomical configurations.

Device development and optimization

The experimental implementation of the toposcopic catheter required a series of technological choices aimed at balancing miniaturization, mechanical performance, and clinical safety. These choices concerned the constituent materials, the internal geometry of the tube, the assembly processes, and the mechanisms of eversion and control (Figure 2.5).

The primary material chosen for the evertable membrane was Texin 480A, a polyether-based thermoplastic polyurethane. This polymer was selected for its abrasion resistance, flexibility, ability to be extruded into thin walls, and thermal formability. The latter property allowed stabilization of specific tube geometries after extrusion. Biological testing also confirmed its good tissue compatibility — an essential requirement for in vivo use.

The *evertable* tube was permanently attached to the distal end of a conventional catheter approximately 1 meter long using an insertion-based thermal welding process with localized heating ($\approx$ 315 °C) and controlled pressure. This method ensured cohesive bonding without mechanical weakening. Three sizes were developed for the advanced clinical version: 1 mm (3F) with a wall thickness of 0.064 mm, 1.3 mm (4F) with 0.084 mm, and 1.7 mm (5F) with 0.103 mm.

The eversion length reached 40 cm or more, representing a significant improvement over earlier versions limited to 30 cm. To ensure smooth deployment, two complementary strategies were implemented to reduce internal friction forces between the everted membrane and the sliding inner layer:

1. The tube's cross-section was designed to allow controlled flattening under pressure. A cross-shaped profile was initially tested with good results, facilitating symmetric folding of the tube. It was later replaced by a U-shaped configuration, which was simpler to produce while maintaining similar performance. In the most advanced versions, tri- or quadrilobed sections were

developed to further reduce drag by minimizing contact surfaces and improving bending flexibility.

2. In parallel, the inner surfaces were treated with a hydrophilic coating consisting of a polyvinylpyrrolidone hydrogel incorporated into the polyurethane. This coating, activated by the fluid injected into the annular space (usually a contrast agent), formed a low-friction lubricating layer (coefficient $\approx$ 0.05), facilitating eversion even at low pressure.

Thanks to these structural and tribological optimizations, the minimum eversion pressure in unconstrained conditions was reduced to 65 kPa for a 1 mm tube, enabling atraumatic insertion. In cases of pronounced tortuosity or long distances, pressure could reach 250 kPa while remaining well below the estimated rupture thresholds (between 300 and 400 kPa).

Finally, a complete redesign of the control system was carried out to facilitate clinical use of the device. While early prototypes required bulky equipment (vacuum pumps, electromechanical valves, liquid-air interfaces), the advanced clinical version relied on a vented syringe connected to the annulus via a three-way stopcock. This compact and robust system allowed manual regulation of annular pressure (positive, negative, or holding), sterile filling of the annular space, and provided passive safety in case of leakage.

Just before use, the annular space was filled by injecting a contrast agent, which activated the lubricating coating and made the entire device visible under fluoroscopy. This fully polymeric, self-contained, and compact configuration significantly improved catheter maneuverability while simplifying sterile on-site preparation.

Experimental and preclinical validation

The feasibility of the toposcopic catheter was evaluated through a series of in vitro and in vivo tests to validate its performance in constrained anatomical environments (Figure 2.6).

In sinuous glass models with a 1 mm diameter, deployment occurred without blockage or the need for excessive pressures. In vivo testing in dogs confirmed

the device's ability to progress through deep and tortuous segments of the vascular network (carotid arteries, visceral arteries, thyroid veins) without causing spasm or observable injury.

Once in position, injection through the annulus enabled localized delivery of contrast agents at the distal tube end, with good fluoroscopic visibility. The lobed sections promoted the formation of lateral jets, useful for targeted therapeutic applications. Finally, catheter withdrawal was initiated by simple depressurization combined with slight traction, allowing complete retraction in under two minutes without structural damage.

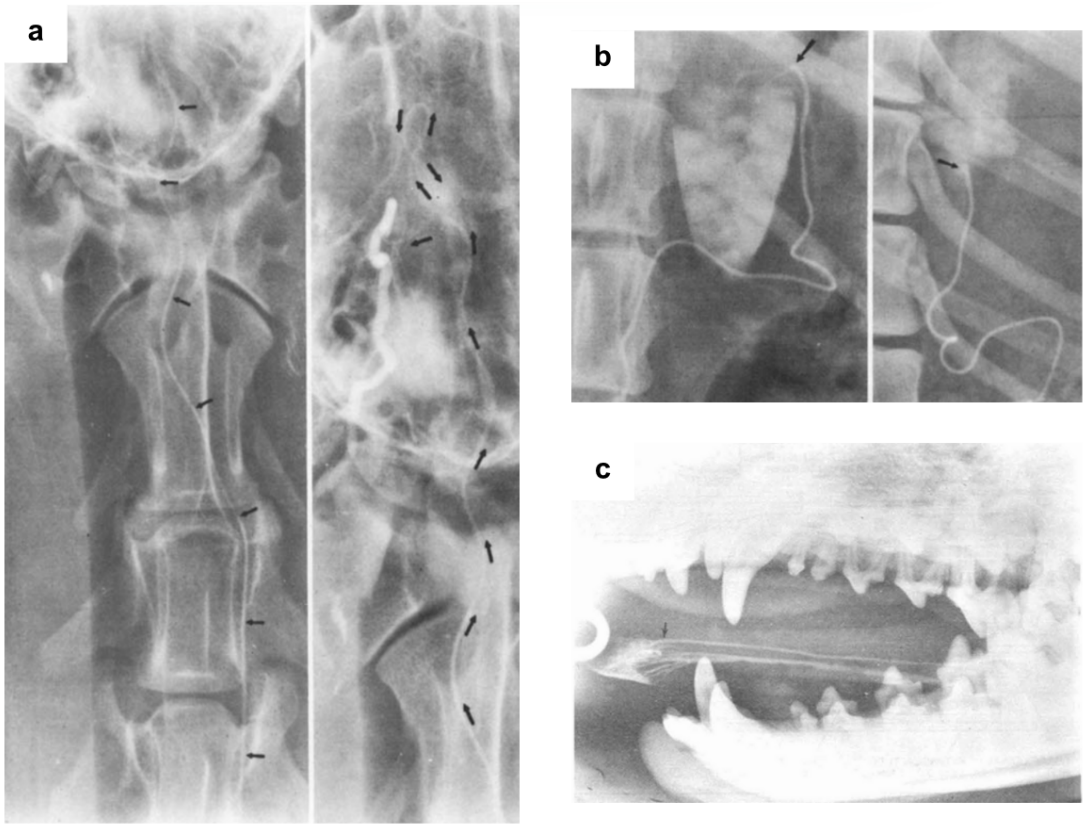


Figure 2.6: In vivo testing of the toposcopic catheter. (a) Catheter (arrows) ascending the left vertebral artery via the anterior spinal and basilar arteries to retrogradely access the internal carotid artery. (b) Catheter (arrows) in the hepatic branch of the left gastric artery, AP and lateral views with hepatic staining. (c) Angiogram showing a toposcopic catheter (arrow) at the tip of a dog's tongue, accessed via a branch of the external carotid artery. All images reproduced from Doppman et al. (1979) [3] and Goldstein et al. (1980) [1].

These results confirmed the robustness of the system and suggested potential clini-

cal applications in areas previously inaccessible to conventional devices. However, despite these encouraging preclinical validations, no significant clinical or industrial development was pursued. According to Seth Goldstein[2], the project lost momentum after the death of Dr. John L. Doppman, who had been the principal investigator and leading contributor to its development. In parallel, the development of soft catheters — simpler to manufacture and to control — gradually took precedence, despite the advantages offered by eversion-based approaches.

In summary, these studies highlighted the relevance of eversion-based mechanisms, but their development remained limited and did not progress toward clinical application.

2.4 From *extraversion* to eversion

Several decades later, the emergence of soft robotics provided a new conceptual and technological framework within which eversion principles could be revisited and further developed.

2.4.1 Emergence of soft robotics

Context and challenges

Soft robotics is a rapidly expanding field that emerged in the 2010s, aiming to design systems capable of operating in complex, fragile, or poorly understood environments [77–79]. Unlike traditional rigid industrial robots, which rely on articulated structures and precise motion planning, soft robots prioritize flexibility and compliance to interact with their surroundings in a safe and robust manner.

To achieve these capabilities, soft robotics builds on three fundamental principles (Figure 2.7) :

[2]This information was obtained during a videoconference interview with Seth Goldstein, who was directly involved in the development of the device at the time.

- the use of structures and materials capable of undergoing large, continuous deformations without rigid joints;

- distributed actuation strategies enabling the control of soft bodies with numerous implicit degrees of freedom;

- manufacturing processes leveraging elastic materials responsive to external stimuli (such as pressure, temperature, or electric fields) to generate complex behaviors from simple control inputs.

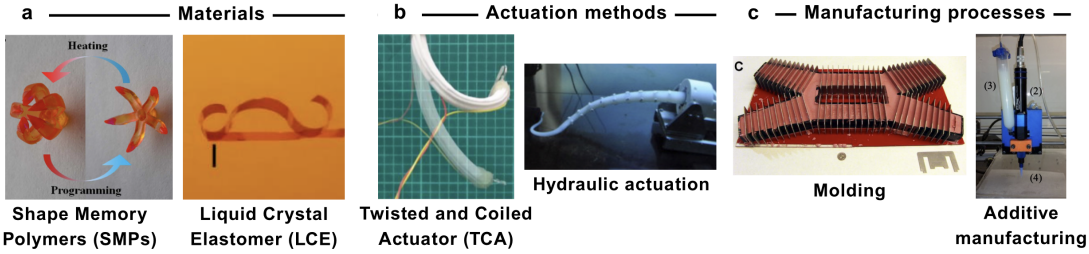


Figure 2.7: Examples of technologies in soft robotics, including (a) materials such as shape-memory polymers [4] and liquid crystal elastomers [5], (b) actuation methods such as twisted-coil actuators [6] and hydraulic systems [7], and (c) fabrication processes such as molding [8] and additive manufacturing [9]. All images are reproduced from the respective publications cited for each example.

Numerous biological systems provide efficient models of locomotion and interaction that have inspired soft robotics, particularly deformable-bodied animals such as octopuses [7, 80, 81], caterpillars [82, 83], and elephant trunks [84, 85], whose mobility relies on continuous deformation and distributed control.

Yet, soft robots inspired by biology extend beyond the animal kingdom. Indeed, the plant world offers remarkably ingenious strategies for growth and navigation. Through their ability to explore their environment via directional growth, to circumvent obstacles by locally modifying their morphology, and to deploy in confined environments, plants represent a unique model of progressive and passive adaptation. These natural mechanisms inspired a new class of robotic systems: eversion-based soft robots, whose progression relies on the continuous elongation of their structure.

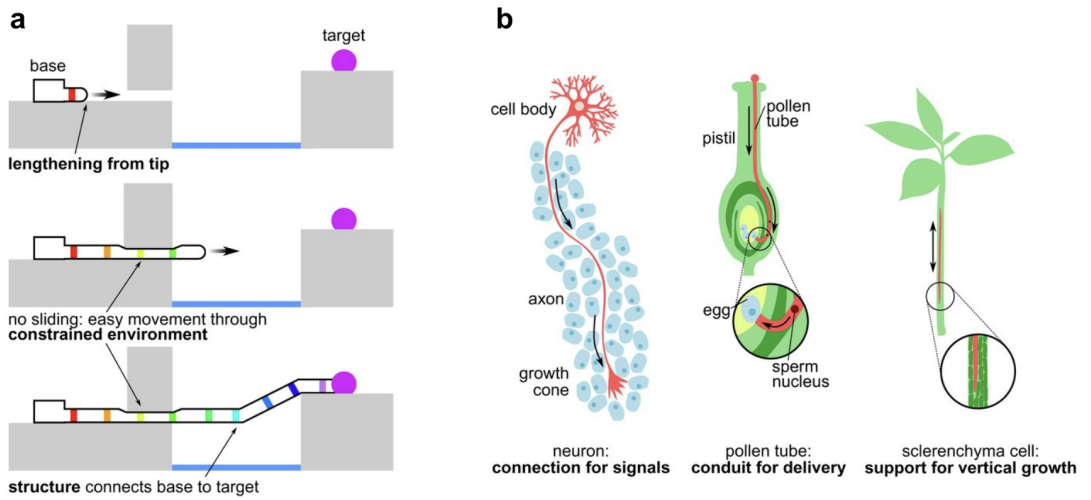


Figure 2.8: (a) A body elongates from its tip toward a target. As the tip advances, the body adopts the shape of the traversed path. (b) Examples of biological systems that grow to navigate their environment. Reproduced from Hawkes et al., 2017 [10].

Modern rediscovery of eversion

This botanical analogy led to a reinterpretation of an old physical principle — *extraversion* — through a modern lens. In 2017, the work of Hawkes et al. [10] marked a decisive turning point in the rediscovery of this principle, now widely referred to as eversion (Figure 2.8). The robot, often described as a vine robot or growing robot, relies on the same principle of apical extension: driven by internal pressure, it deploys by turning its wall inside out, with the material forming its body transported from the base to the tip.

This inherited mechanism was reinterpreted through an architecture capable of steering, adapting to its environment, and progressing continuously without requiring external anchoring or pulling. Eversion, previously regarded as a passive deployment method, thus became a genuine mode of autonomous locomotion. This approach opens new perspectives for robotic exploration, particularly in constrained or hard-to-reach environments.

Building on these contributions, research has gradually been structured around several complementary directions: improving steerability, developing embedded sensing strategies, and optimizing materials and robotic architectures (Figure 2.9). Several recent review articles have attempted to map these advances, iden-

tifying major trends and remaining challenges.

Among them, three recent reviews provide complementary analyses of the progress achieved: the review by Al Harthy et al. [86] (2024), offering an in-depth analysis of engineering principles and mechanical architectures; the review by Oyejide et al. [87] (2025), focusing specifically on miniaturized variants of these robots for medical applications; and the review by Suulker et al. [88] (2026), dedicated to soft eversion robots for colonoscopy. It should be noted, however, that while Al Harthy et al. acknowledges early experimental work such as that of Doppman in the late 1970s, this review traces the origins of eversion back only to Wood's 1977 patent on pipeline lining. Earlier medical patents are not mentioned, even though they had already introduced the principle of eversion under different terminology. In this sense, the present manuscript offers a complementary perspective by reintegrating these contributions into the historical continuum.

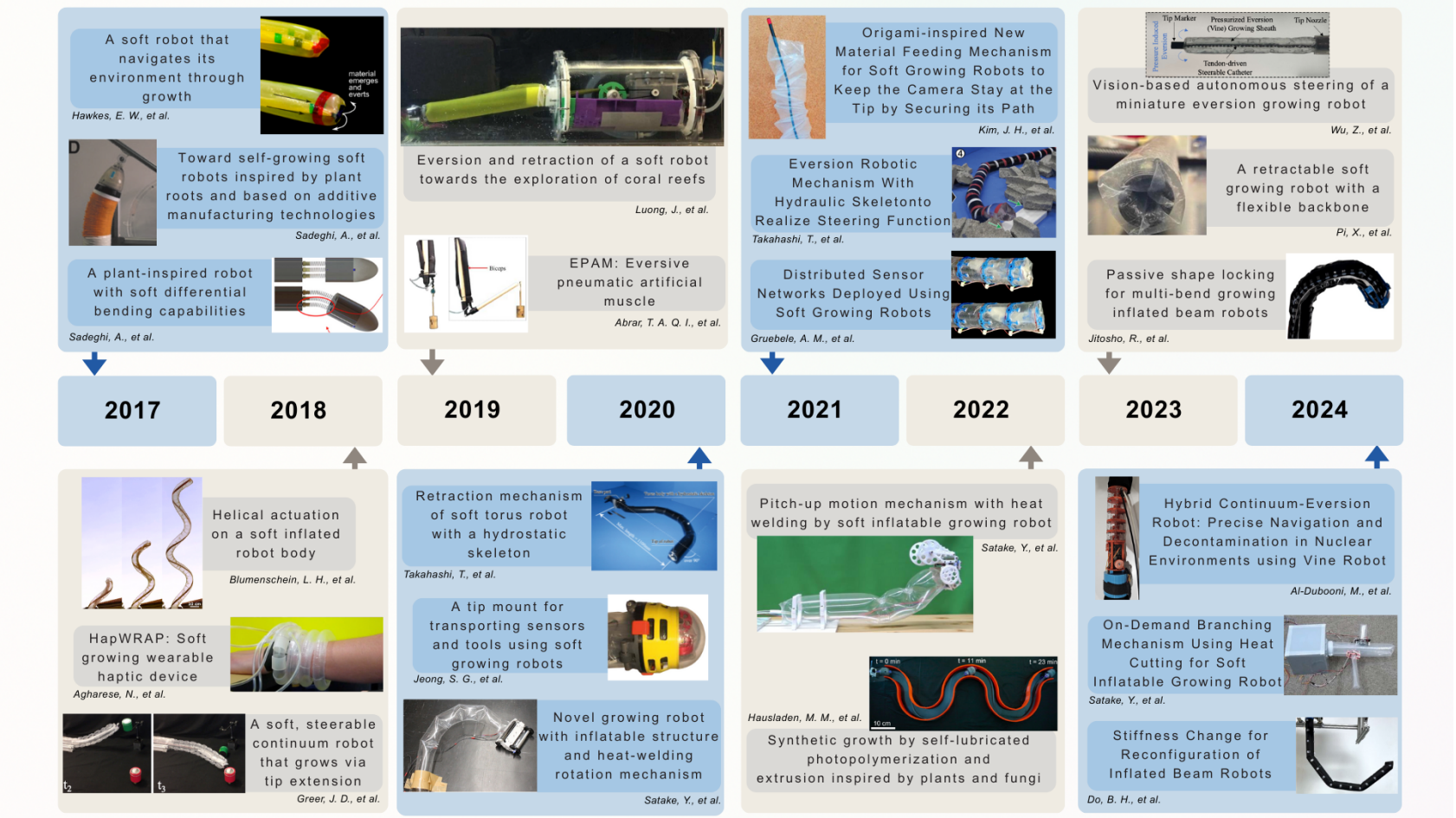


Figure 2.9: Timeline of key developments in the field of soft eversion-based robots from 2017 to the present time. Each year highlights notable contributions, including works by Hawkes et al. and Sadeghi et al. (2017) [10–12]; Blumenschein et al., Agharese et al., and Greer et al. (2018) [13–15]; Luong et al. and Abrar et al. (2019) [16, 17]; Takahashi et al., Jeong et al., and Satake et al. (2020) [18–20]; Kim et al., Takahashi et al., and Gruebele et al. (2021) [21–23]; Satake and Ishii and Hausladen et al. (2022) [24, 25]; Wu et al., Pi et al., and Jitosho et al. (2023) [26–28]; and recent advances in 2024 by Al-Dubooni et al., Satake et al., and Do et al. [29–31]. All images shown in the timeline are reproduced from the respective publications cited for each year.

2.4.2 Technological diversification of eversion

From a general perspective, the literature reveals a remarkable diversity of growth strategies. Pneumatic eversion — in which a flexible tube is turned inside out by internal pressure — remains the most widespread method. It offers a simple, rapid, and nearly frictionless mode of deployment relative to the environment. In parallel, other modalities have emerged: in situ additive manufacturing, enabling the robot to construct its own body through thermoplastic extrusion at the tip [11]; self-lubricated photopolymerization, combining localized solidification with reduced internal friction [25]; and selective thermal welding, used to create localized rigid structures during growth [20, 24, 30]. Each of these strategies presents trade-offs: while pneumatic eversion allows rapid but relatively unstructured extension, additive manufacturing introduces significant pushing forces and requires complex thermal management. Thermal welding enables the creation of self-stabilizing shapes but imposes a command granularity incompatible with certain dynamic applications.

Steering and bending mechanisms — essential for autonomous navigation — have also been explored in various ways. Systems inspired by plant differential growth, using inflatable chambers or serial pneumatic actuators, enable gradual bending without adding rigid components [89]. Other approaches rely on thermal welding to create irreversible bending points [20, 24, 30], or on integrating semi-rigid tips actuated by cables within a hybrid design [26, 29]. While these strategies improve trajectory precision, they can sometimes compromise one of the fundamental advantages of growth robots: their ability to conform to narrow spaces with low contact energy and without external rigidity.

Retraction remains one of the main technological challenges for eversion-based robots. Their flexible nature makes them vulnerable to buckling during any attempt at axial withdrawal. Proposed solutions range from adding an internal skeleton (a flexible longitudinal tube) [18, 26, 27] to retraction systems based on fluid actuation or active anchors positioned at the tip [16, 19, 22]. However, these devices remain partially effective in curved configurations and often add structural or mechanical interface complexity.

In parallel, sensor integration — a prerequisite for robust autonomous navigation

— remains an evolving area. Distributed sensor networks, often implemented on flexible printed circuits, allow partial tracking of shape and environmental conditions [23]. Other strategies include using tactile sensors at the tip to detect obstacles or embedded cameras actuated by origami-inspired mechanisms [12, 21]. While these innovations demonstrate technical feasibility, they still raise questions regarding the balance between embedded functionality and constraints on flexibility, weight, and miniaturization.

2.4.3 Medical motivations for eversion

This wave of innovations has led to new approaches specifically adapted to the anatomical constraints of the medical field. Figure 2.10 summarizes the main devices designed for endovascular navigation, colonoscopy, and breast duct exploration. These eversion robots minimize mechanical interactions with surrounding tissues by keeping their bodies static once deployed. This property facilitates progression in tortuous environments and enables access to anatomical regions previously unreachable with rigid instruments, such as the colon for polyp detection [36], upper and lower gastrointestinal endoscopy [90], renal calyces [45], mammary ducts for breast cancer screening [26, 40, 41], blood vessels in endovascular surgery [34], or the spinal subarachnoid space [32].

A central challenge for these devices lies in integrating a hollow working channel necessary for the passage of biopsy tools, cameras, or sensors [32–34, 36, 38, 40]. However, miniaturization of this channel increases internal friction and thus the pressure required for growth. To overcome this barrier, some teams have developed innovative strategies, such as using crumpled materials stored at the tip to reduce friction and enable smaller diameters [35].

Steerability also remains a key issue. Depending on the clinical context, various mechanisms have been implemented: internal cable-driven catheters to bend the robot's tip [32, 40]; segmented pneumatic muscles integrated into the wall for controlled bending [39]; or magnetic materials allowing remote actuation via external fields [44]. Some devices also rely on preformed geometries tailored to anatomical pathways to reduce normal forces exerted on tissues during extension [34, 45].

Beyond growth and steering, retraction remains an open challenge, notably due to the risk of buckling in curved trajectories. Specific mechanical strategies have been proposed to manage this delicate phase [38, 39, 43]. In parallel, autonomous control systems are being explored, combining force, vision, or magnetic localization sensors with advanced models of the robot's mechanics. From a medical perspective, however, the key requirements remain operational durability and safety: ensuring reliable retraction without tissue damage, preventing risks such as membrane rupture or overheating, and ensuring reproducible performance suited to a clinical environment.

In summary, growth-by-eversion robots open new perspectives for minimally invasive surgery. However, their future adoption will depend on resolving challenges related to miniaturization, reliable retraction, autonomous control, and clinical validation.

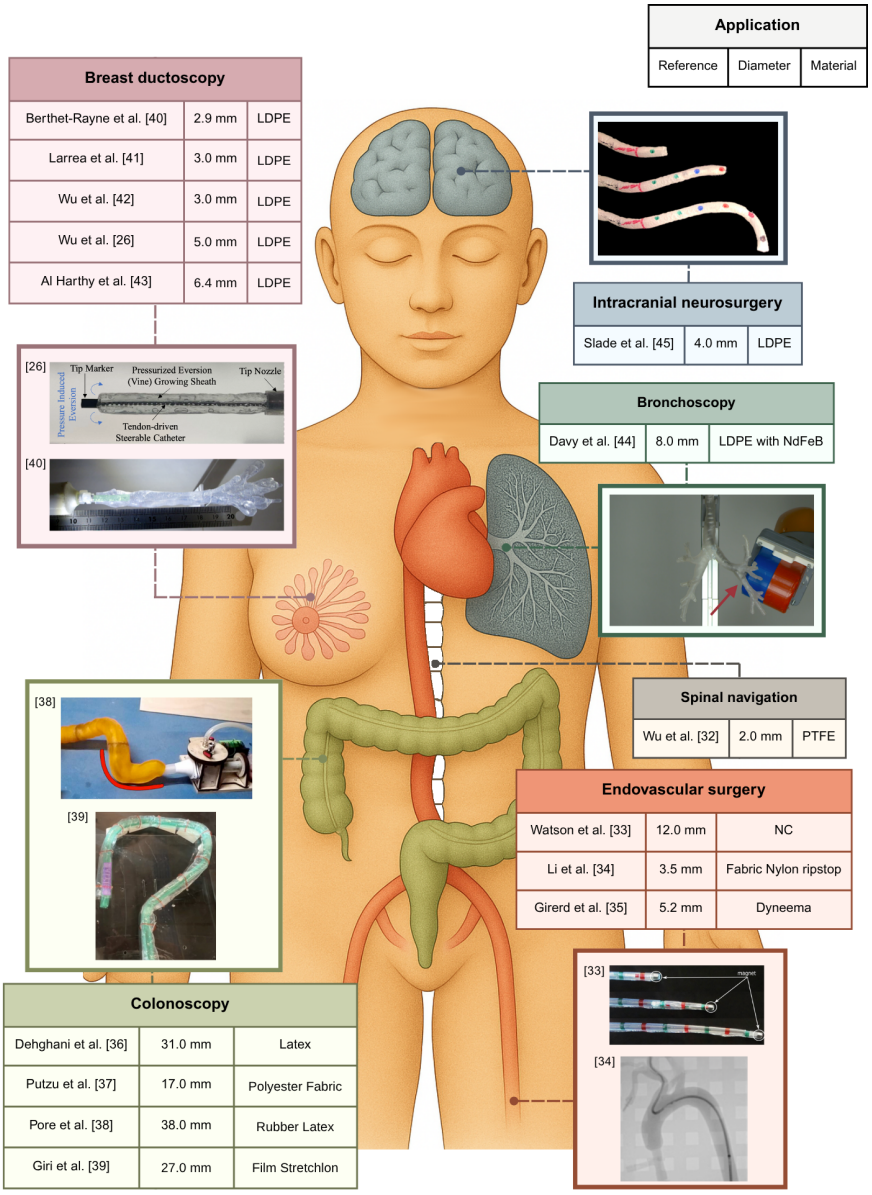


Figure 2.10: Overview of eversion-based robot applications in different anatomical targets. Each entry indicates the first author, device diameter, and material. Studies are grouped by application domain: spinal navigation [32]; endovascular surgery [33–35]; colonoscopy [36–39]; mammary ductoscopy [26, 40–43]; bronchoscopy [44]; and intracranial neurosurgery [45]. All images are reproduced from the respective publications cited for each example.

2.4.4 Principles and tools for eversion modeling

The technological and clinical challenges associated with these robots highlight the need for a deep understanding of the mechanical and kinematic principles governing their growth. In this context, modeling becomes an essential tool. It first enables the analysis of the kinematics and mechanics of eversion-based robots : this unique process, in which the material unrolls from the base toward the tip, induces specific deformations and carries risks, such as axial or lateral buckling in the presence of obstacles.

Furthermore, modeling offers crucial predictive capabilities. It makes it possible to predict the stresses and deformations experienced by the materials, estimate the pressures required for growth, and anticipate the robot's final shape under various loading and actuation conditions. It serves as a key tool for dimensioning and material selection, by quantifying interactions with the environment, it guides design choices (like membrane diameter and thickness) to strike a balance between flexibility and strength. Ultimately, modeling is indispensable for ensuring structural safety by identifying critical conditions that could lead to buckling or rupture, thereby enabling the design of robots capable of reliably growing in complex environments.

Analytical methods and simplified models

Several analytical and simplified approaches have been developed to describe the fundamental behaviors of eversion-based growth robots. Geometric models form the basis of these descriptions. The constant-curvature model, widely used for continuum manipulators, relates deployed length, curvature angle, and curvature plane to predict the robot's shape [91, 92]. Other, more general geometric models, including helical actuation or more complex configurations, rely on precise relationships assuming an inextensible but flexible tube capable of bending to change shape [93]. These formulations allow prediction of the resulting shape for a given actuation or the design of an actuator capable of producing a target shape.

Lumped-parameter models offer another approach: they describe the robot using a reduced number of points along its main axis, such as the tip or contact points

[94, 95]. Rather than aiming for high physical accuracy, these models prioritize simplicity and computational efficiency, which makes them particularly attractive for real-time applications such as trajectory planning.

Quasi-static models have also been adapted to estimate the forces required for propulsion and to evaluate frictional losses [96, 97]. Inspired by the Lockhart-Ortega equation (used in biology for cellular growth) and the Capstan equation (employed for tension transmission in Bowden cables), these models decompose losses into trajectory-independent components (threshold pressure, velocity dependence) and components dependent on length and curvature. This approach provides a more detailed characterization of internal friction and additional losses related to geometry.

However, these analytical methods have significant limitations. They rely on simplifying assumptions—such as purely planar motion, mass concentrated at a single point, or linear behavior for materials that are, in reality, strongly nonlinear—and sometimes neglect complex phenomena such as detailed friction with the environment or multiple interactions between closely spaced contact points. These limitations explain why, beyond initial design estimates, it becomes necessary to resort to more comprehensive numerical methods to capture the true complexity of these robots' behavior in operation.

Numerical simulation

To overcome the limitations of analytical approaches, numerical simulation emerges as an essential tool for the design and study of eversion-based growth robots. It enables a more faithful representation of complex 3D shapes, nonlinear deformations, and interactions with the environment, going beyond the simplifications inherent in analytical models. However, not all simulation approaches pursue the same goals: they involve trade-offs between physical fidelity and computational performance.

The simulator developed by Jitosho et al. [46] illustrates an approach focused on real-time motion planning (Figure 2.11). It models the robot as a rigid-body, multi-link system with prismatic joints that abstract growth while maintaining a fixed-size state vector—a crucial aspect for computational speed and compatibil-

ity with conventional planning algorithms. This simplification efficiently handles contacts via predefined points along the robot. This modeling assumption, however, introduces an approximation: when the contact points are too sparsely distributed, the interaction with the environment may be inaccurately represented. Moreover, the nonlinear behaviors typical of thin-walled structures—such as buckling or localized folding—are represented by approximations like distributed bending, with full nonlinear buckling modeling identified as future work. This type of simulator also neglects continuous length variation and the translation dynamics of the sheath, which are inherent to the eversion mechanism. To reduce the gap between simulation and reality, empirical parameter tuning based on experimental data is required, indicating that the simulation remains an approximation of the actual geometric and mechanical behavior.

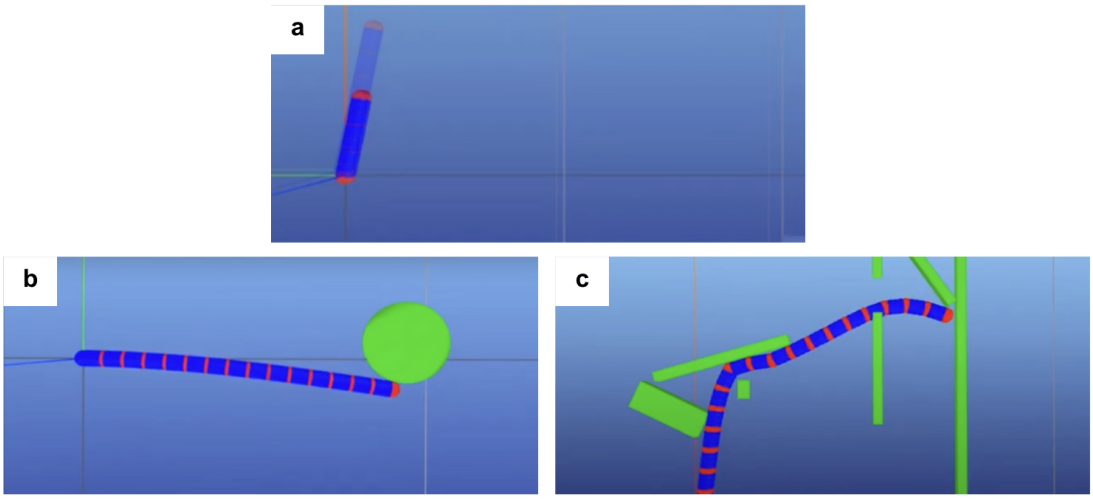


Figure 2.11: Examples of simulated behaviors and scenarios generated by the simulator, based on a rigid-body, multi-link approximation of the eversion mechanism, including (a) growth, (b) bending, and (c) various contact interactions. Reproduced from Jitosho et al., 2021 [46].

Conversely, Finite Element Method (FEM)-based approaches, such as those implemented with the Simulation Open Framework Architecture (SOFA) framework in the work of Wu et al. [42], aim for highly detailed and physically realistic modeling (Figure 2.12). They seek to capture the full dynamics of eversion: continuous length changes, sheath translation, stiffening effects due to internal pressurization, as well as complex interactions with the environment and gravity. This level of fidelity enables detailed study of phenomena such as buckling, localized folds, or multiple contacts in constrained anatomical environments. However, it comes

at a high cost, as FEM simulations are computationally expensive and often slow, which limits their use for real-time planning or closed-loop control. Wu et al. also highlight specific challenges, such as difficulties in simulating sheath growth with volumetric or surface meshes, numerical stability issues for large time steps, and the complexity of efficiently modeling internal friction. Discrepancies observed between simulated and experimental results for certain behaviors illustrate the persistent difficulty of achieving perfectly accurate modeling for miniaturized soft systems.

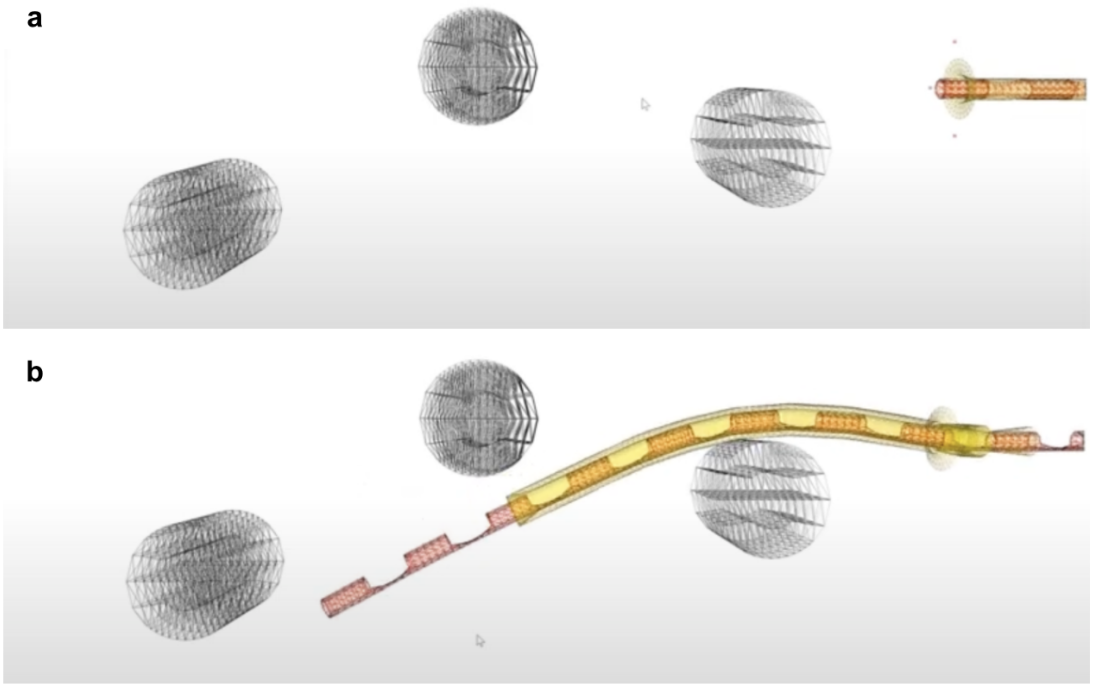


Figure 2.12: Examples of FEM-based simulations of the eversion mechanism using the SOFA framework, including (a) continuous deployment through internal pressurization and (b) detailed collision interactions in constrained environments. Reproduced from Wu et al., 2023 [42].

In summary, while numerical simulation is essential for understanding, predicting, and designing eversion robots, the choice of approach remains a fundamental trade-off. Simplified simulators favor speed and compatibility with motion-planning algorithms but inevitably sacrifice physical accuracy. Conversely, FEM-based simulators provide physical fidelity and allow exploration of complex behaviors, but at the cost of high computational demand and calibration challenges that underscore the persistent difficulty of reproducing the reality of soft robots.

2.5 Preliminary experiment

The literature highlights the potential of eversion robots for efficiently navigating complex anatomical environments, particularly in the context of endovascular access. Building on this observation, one of the first objectives of our work was to assess the possibility of transposing these concepts to a TAVI procedure, which requires a trajectory from the femoral artery to the aortic valve. In this perspective, the work of Li et al. [34], who developed an eversion-based robot specifically adapted for endovascular navigation, served as an essential reference from which our first experimental prototypes were derived.

More specifically, the use of a textile combined with a controlled deposition of silicone adhesive presents the decisive advantage of enabling precise preforming of the robot, a task that is difficult to achieve with extruded tubes. This technique therefore makes it possible to obtain curvatures tailored to the anatomical constraints of the pathway, particularly at the level of the aortic arch in the intended application. The resulting preformation gives the robot a passive navigation capability, allowing it to follow a predefined anatomical route without resorting to active steering mechanisms. This avoids the addition of components that could increase the overall stiffness and compromise progression within constrained vascular environments.

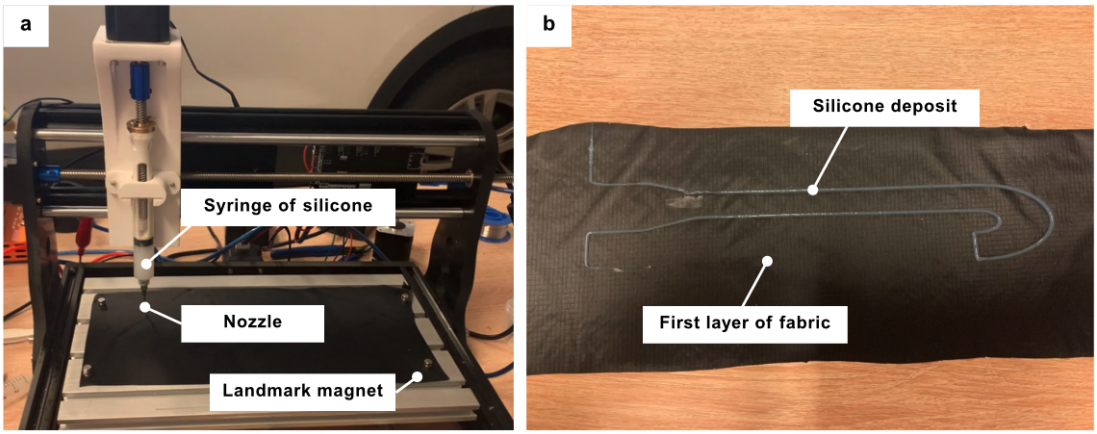


Figure 2.13: (a) Automated preforming device with numerical control, equipped with a silicone syringe and a 15G nozzle, with a system of positioning and holding magnets. (b) Close-up view of silicone deposition on the first textile layer.

To improve prototype reproducibility and simplify fabrication, this initial concept

was revisited through the development of an automated process. A numerically controlled machine (Figure2.13-a) was adapted to perform a regular and homogeneous deposition of silicone adhesive (*Sil-Poxy*, Smooth-On) directly onto a first layer of textile (*Ripstop Nylon 6.6*, Extremtextil), precisely following a predefined trajectory based on a CAD model. The superposition of a second textile layer forms the soft, sealed body of the robot, whose outline is then cut to obtain its final shape (Figure2.13-b).

The resulting prototypes met the targeted dimensions to faithfully reproduce the anatomy encountered during a TAVI procedure: an 8 mm diameter (corresponding to a 12.56 mm circumference) matching the average caliber of the thoracic aorta, a deployed length of about 600 mm covering the trajectory from the femoral artery to the aortic valve, and a curvature radius of about 50 mm at the aortic arch.

Initial trials were conducted outside any biological environment, in a controlled experimental setting, to observe the robot's behavior during eversion. Internal pressurization was provided by a customized syringe pump, ensuring a steady flow and stable pressure for deployment (Figure 2.14-a). Initial empty trials confirmed that deployment was continuous, with no blockage or interruption of the eversion mechanism, and visually demonstrated the robot's ability to follow the preformed curvature (Figure 2.14-b). The device was then evaluated in a rigid phantom reproducing the targeted arterial pathway, in order to test its ability to progress within an anatomically representative conduit (Figure 2.14-c). These trials confirmed the feasibility of deployment but also showed that progression could be slowed by mechanical resistance related to pronounced curvatures and friction against the inner wall of the conduit.

To approach clinical conditions, a complementary trial was performed on a cadaver. Access to the right femoral artery was obtained by direct opening, allowing the placement of a 24F introducer (*2064-HQS-24F*, Alcis) on which the robot was positioned. Eversion was then carried out by manually injecting, through a syringe connected to the introducer, a saline solution mixed with a contrast agent (*Iomeron 350*) (Figure 2.15-a). The use of a saline solution was dictated by endovascular safety considerations. In intravascular procedures, the presence of air entails a risk of gas embolism in the event of leakage, which may lead to severe

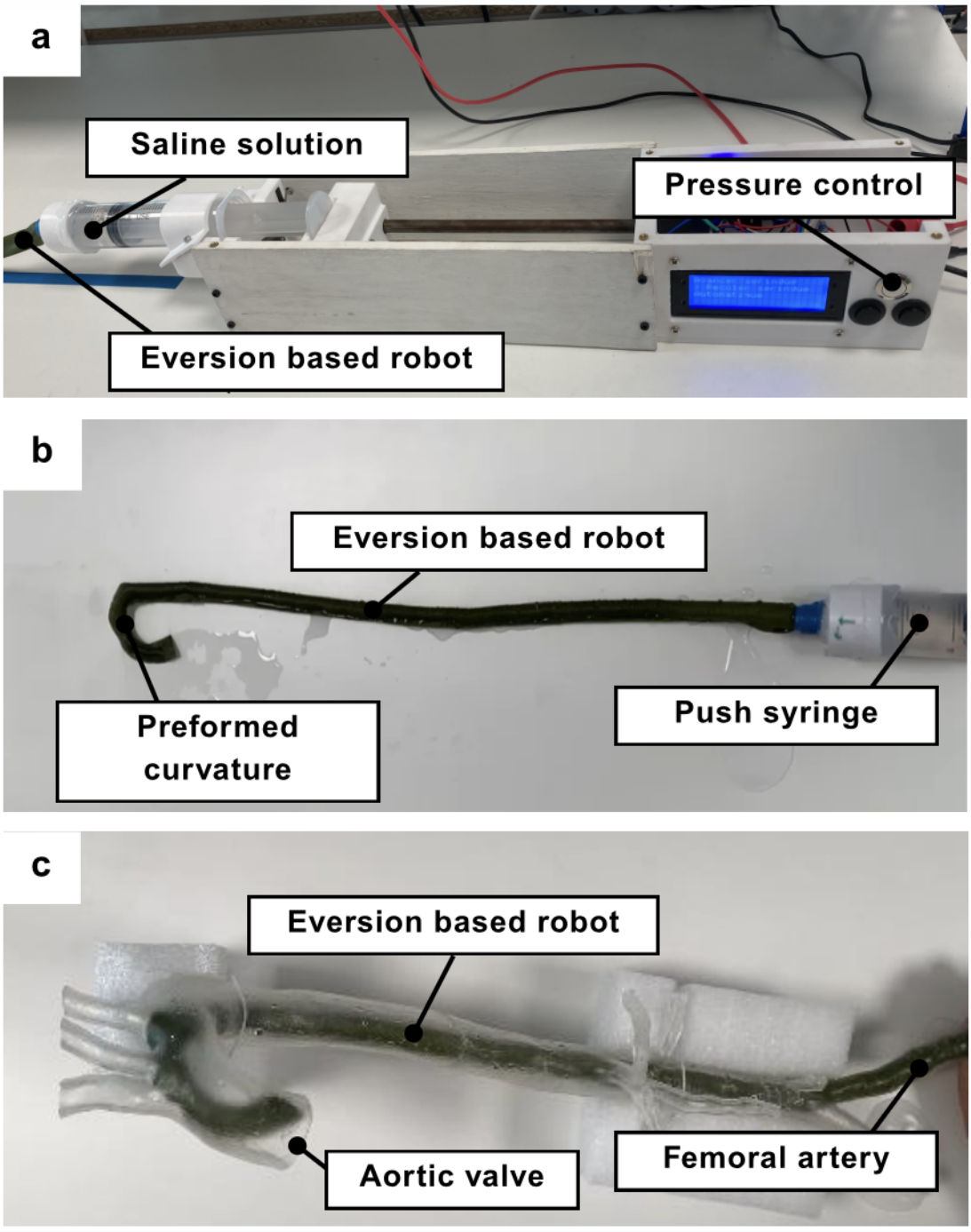


Figure 2.14: (a) Syringe pump injecting saline solution into the eversion-based robot, enabling generation and control of internal pressure. (b) Trial in a free environment showing the deployment of the preformed robot using a syringe pump, demonstrating continuous eversion along the programmed curvature. (c) Progression test in a rigid phantom reproducing an arterial pathway from the femoral artery to the aortic valve.

complications. Although pneumatic actuation is widely employed in the state of the art, its direct transposition to in vivo endovascular applications raises significant safety concerns. A physiologically compatible fluid was therefore required, leading to the selection of saline solution for these trials.

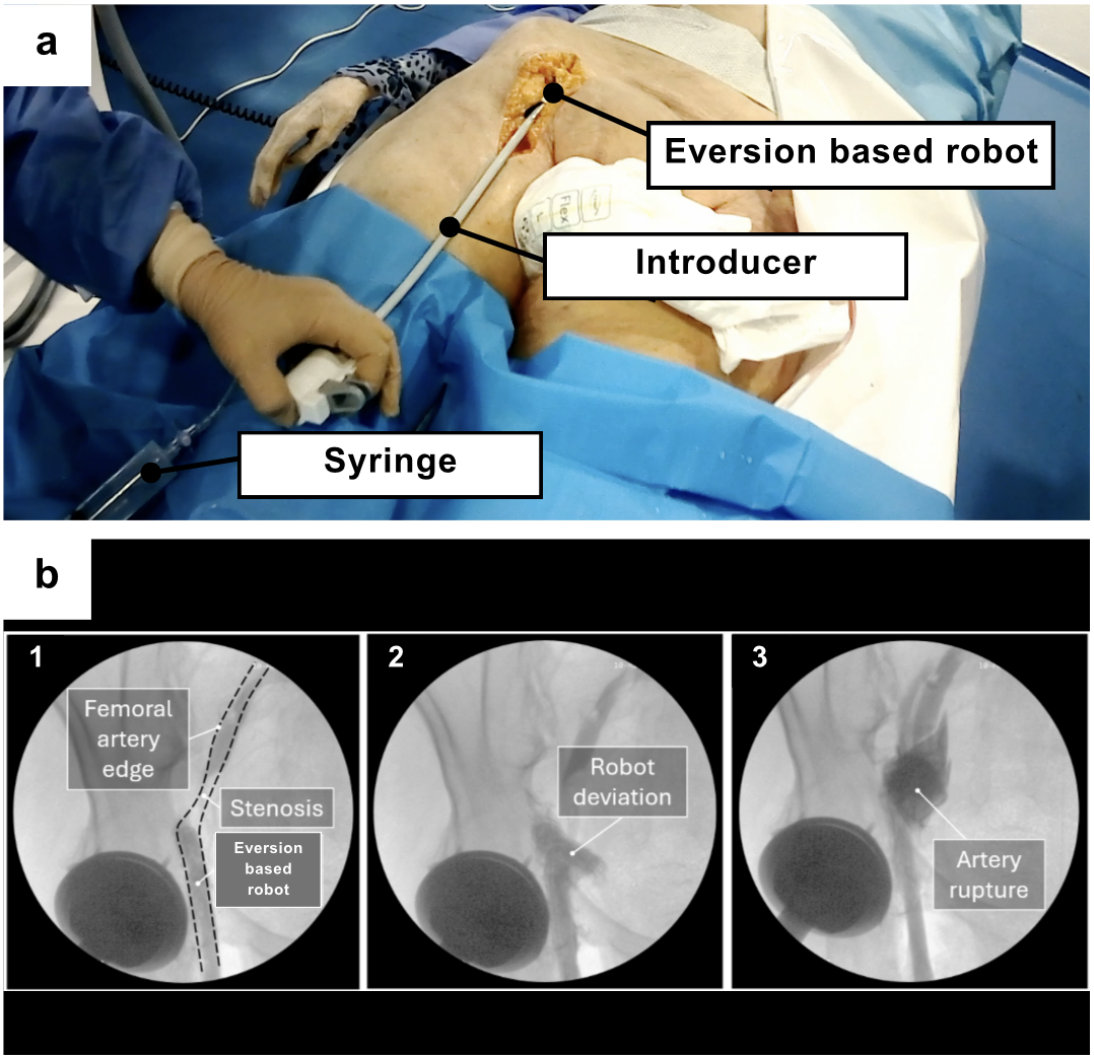


Figure 2.15: (a) Experimental setup of the cadaveric trial: eversion robot inserted into a 24F introducer and supplied with saline solution mixed with a contrast agent via syringe injection. (b) (1) View of the robot's progression in the femoral artery showing (2) the initial deviation at the level of a proximal stenosis, followed by (3) an arterial rupture on the femoral side, illustrating the constraints encountered when crossing pathological zones.

During progression, the robot encountered a proximal stenosis, leading to a deviation of its trajectory. To cross this narrowed area, an increase in injection

pressure was required, which resulted in a tear of the arterial wall (Figure 2.15-b). To ensure that the incident was not caused by device failure, the robot was removed and redeployed outside the artery, confirming the complete integrity of its membrane.

These experiments confirmed that the eversion principle works and enables effective deployment in constrained anatomical environments. However, the cadaveric trial revealed major limitations when the pathway includes pathological zones. The occurrence of a deviation followed by an arterial rupture while crossing a narrowing led to an in-depth analysis of this incident with medical specialists, who confirmed the likely presence of a proximal stenosis at the femoral access and emphasized the frequency of such lesions in TAVI patients.

These observations led us to hypothesize that this complication resulted from the interaction between the robot's material and the pressurization fluid. While the textile structure exhibits high compliance when empty or pneumatically actuated, its global mechanical response changes significantly when filled with an incompressible fluid. The resulting fluid–structure coupling increases the effective structural stiffness of the system and reduces its ability to conform to localized arterial narrowings. Under such conditions, the pressure increases required to overcome resistance may amplify stresses exerted on the vascular wall and contribute to vascular injury.

More broadly, this experiment revealed a regime that remains insufficiently addressed in the current literature: fluid-actuated eversion in severely constrained endovascular environments. Most existing systems rely on pneumatic actuation, while fluid-based approaches are typically evaluated in simplified or weakly constrained settings. The combined influence of fluid incompressibility, material extensibility, and pathological narrowing in clinically relevant conditions has not, to our knowledge, been systematically investigated.

This observation constitutes the scientific starting point of the present thesis. The following chapters will therefore focus on analysing the coupled influence of material behaviour and pressurization fluid on deployment stability and compliance, with the objective of identifying critical parameters and proposing design strategies compatible with safe endovascular navigation.

2.6 Research Objectives and Contributions

The cadaveric trial revealed that the transition to fluid actuation fundamentally modifies the mechanical behaviour of the robot in constrained vascular environments. The loss of conformability observed under saline pressurization highlighted the need to identify design parameters capable of restoring compliance while preserving deployment stability.

The central objective of this thesis is therefore to characterise and optimise the coupled regime of fluid-actuated eversion in clinically relevant endovascular conditions. This optimisation is governed by constraints intrinsic to the intended TAVI application.

First, the robot diameter must be compatible with the physiological dimensions of the targeted arterial pathway, from the femoral artery to the thoracic aorta, while remaining sufficiently compact to allow safe insertion. Second, the device must be capable of crossing stenotic segments without requiring pressure levels that could endanger the vascular wall. Third, the structure must preserve sufficient compliance to adapt to local anatomical variations and avoid excessive stress concentration. Finally, mechanical stability must be ensured during long-distance deployment under fluid loading.

The selection of materials, geometrical parameters, and pressurization conditions is therefore driven by these combined anatomical, clinical, and mechanical requirements. Materials must provide a balance between axial flexibility and structural integrity under incompressible fluid loading. Geometrical parameters, including diameter, wall structure, and preformed curvature, must ensure anatomical compatibility while limiting stress amplification during curvature and narrowing crossing. Pressurization conditions must enable controlled eversion while avoiding excessive stiffening induced by fluid incompressibility.

To address these challenges, a predictive numerical framework is developed within the SOFA environment, incorporating pressurized eversion, preformation, and interaction with representative vessel walls. This model enables systematic exploration and quantitative evaluation of the design space prior to fabrication. Its predictions are subsequently confronted with experimental trials in stenotic

vascular phantoms, allowing quantitative assessment of crossing pressure, deformation patterns, and deployment stability.

The cross-analysis of numerical and experimental results guides iterative optimisation, leading to a refined prototype specifically adapted to fluid endovascular deployment. The final objective is to demonstrate, in a clinically representative context, the feasibility and safety of fluid-actuated eversion for endovascular navigation in the setting of a TAVI procedure.

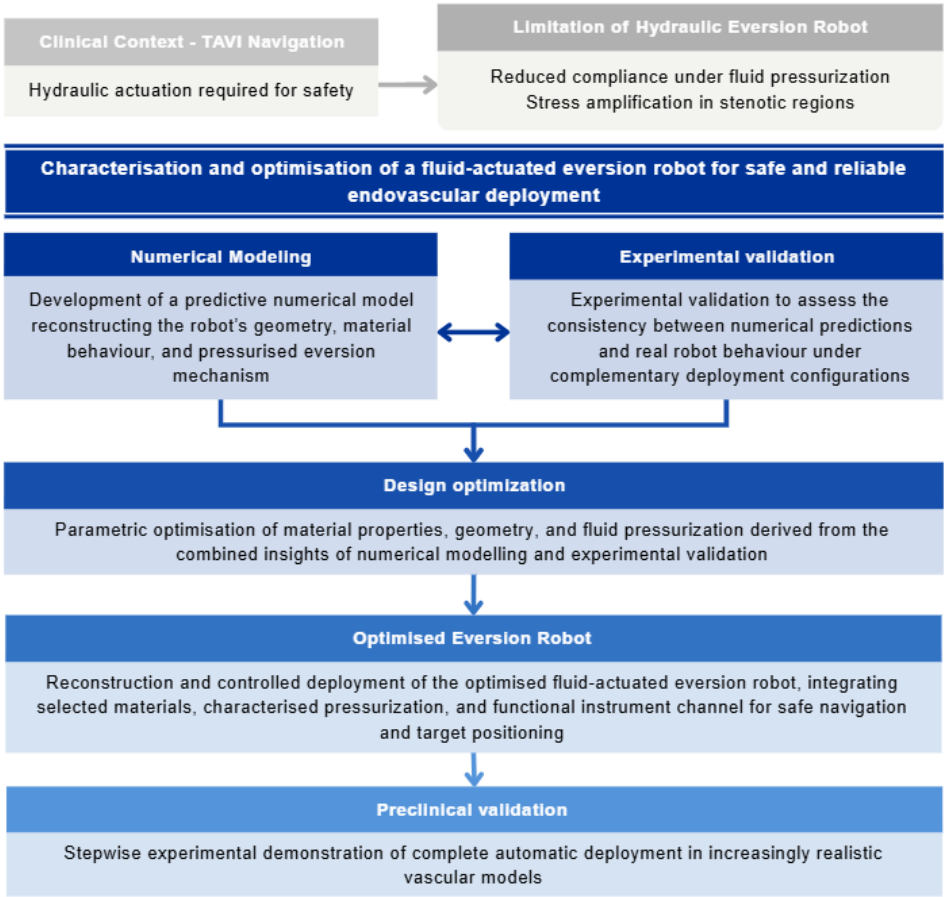


Figure 2.16: Methodological framework for the characterisation and optimisation of a fluid-eversion robot for safe and reliable endovascular deployment. Starting from clinical constraints identified in the context of TAVI navigation and the observed compliance limitations under fluid pressurisation, a predictive numerical model was developed and experimentally validated. The combined insights from modelling and experiments guided the parametric optimisation of material properties, geometry, and pressurisation conditions. An optimised robot was subsequently reconstructed and deployed under controlled conditions, followed by stepwise preclinical evaluation in progressively realistic vascular models.

Chapter 3

Parametric Modeling of the Eversion-Based Robot[1]

Ensuring the safe and atraumatic navigation of the robot during TAVI procedure requires a precise understanding of its mechanical behavior during deployment within the vascular system. Modeling, therefore, plays a pivotal role, as it enables the prediction of interactions with the anatomical environment and the optimization of design choices prior to clinical application. The proposed framework is based on the actual structure of the robot developed in this work, which relies on materials exhibiting contrasted mechanical behaviors, namely an extensible polymer (Thermoplastic Polyurethane (TPU)) and a non-extensible polymer (Low Density Polyethylene (LDPE)).

In the case of eversion-based robots, this task is particularly complex: their deployment relies on a singular mechanism based on the progressive turning inside-out of a stored material under the action of internal pressurization, while advancing through constrained environments. The resulting mechanical behavior is strongly dependent on initial conditions and design parameters such as proximal anchoring, preformed geometry, or pressurization strategy, in close interaction with the mechanical characteristics of the surrounding medium. In the proposed

[1]Content from this chapter was published as:
- Przybylski, F., Adagolodjo, Y., Cerruti, G., Mîra, A., Dequidt, Duriez, C., and Berthet-Rayne, P., "3D kinematics and quasi-statics of a growing robot eversion", In IEEE International Conference on Soft Robotics (RoboSoft), 2023. [98]

framework, this interaction is explicitly represented through boundary conditions and contact formulations, enabling the mechanical influence of the environment to be incorporated into the analysis. This consideration directly conditions the evaluation of deployment stability under constrained configurations. Capturing these coupled effects requires dedicated models capable of consistently representing the robot's behavior during eversion and progression.

Existing modeling approaches (described in Section 2.4.4) each provide valuable insights but remain limited. Simplified geometric models offer an efficient representation of the robot's overall shape and a first understanding of the deployment process. However, they fail to capture key parameters such as the role of material storage, the effect of pressurization on the membrane, or the influence of boundary conditions on the robot's progression. Full finite element models, on the other hand, would allow a detailed description of local deformations and complex interactions with the environment. Their descriptive richness makes them a powerful tool for analyzing complex mechanical behaviors, yet their implementation in the context of eversion remains particularly challenging. Beyond computational cost, achieving numerical stability under such boundary conditions (involving internal pressurization, strong self-contact, and high stiffness-to-mass ratios) is difficult. Moreover, the sudden buckling phenomena observed during the robot's eversion can induce additional numerical instabilities, further limiting the feasibility of a full FEM approach for this class of systems.

It therefore appears necessary to develop an approach that combines the accuracy required to account for these key parameters (storage, pressurization, preformation, boundary conditions) with the flexibility, numerical stability, and computational efficiency required to explore various deployment scenarios. The proposed approach constitutes a generic and adaptable framework rather than a patient-specific model at this stage. It captures the fundamental mechanical mechanisms governing eversion while remaining applicable to diverse environmental constraints, and is designed to support future extensions toward pre-operative simulations based on medical imaging, enabling the design of eversion-based robots adapted to individual vascular anatomies.

Beyond methodological considerations, the proposed modelling framework contributes to improving navigation by enabling a systematic assessment of the

robot's mechanical response under different pressurization levels and constraint configurations. By explicitly integrating the influence of the material behavior considered in this work, notably that of an extensible polymer (TPU) and a non-extensible polymer (LDPE), as well as the effects of preformation and internal pressure, the model allows the identification of stable deployment regimes and mechanically consistent configurations prior to experimental validation.

In this sense, modelling constitutes a decision-support tool for selecting design and operating parameters, promoting controlled and reproducible progression of the robot while reducing the probability of mechanically unfavorable configurations and enhancing overall control of the deployment process.

3.1 A New Modeling Approach

To address the specific challenges posed by eversion, a multi-level modeling strategy is introduced. Rather than relying on a single formalism, this approach aims to combine the tools best suited to the mechanical regimes involved in deployment. Two complementary theoretical frameworks are mobilized: Cosserat theory, well adapted for compact modeling of slender structures, and the finite element method, particularly effective for capturing complex interactions and localized phenomena. Their combination paves the way for a hybrid model specifically tailored to the characteristics of growth-by-eversion robots.

3.1.1 Cosserat Rod Model

Cosserat theory provides a powerful framework for describing the behavior of slender flexible structures such as rods or sheaths, simultaneously accounting for bending, torsion, extension, and shear deformations. Introduced into the field of continuum robotics to simulate the complex deformations of thin structures such as needles [99], cables [100], concentric tube robots [101], and constant-section pneumatic robots [102], the Cosserat model is now regarded as a reference framework for the modeling and control of soft robots, with well-established performance in the dynamic simulation of rod-type robots [103].

Unlike classical beam models, Cosserat theory treats each cross-section of the continuum robot as a rigid body with six degrees of freedom (three translations and three rotations), whereas traditional approaches typically describe only translational motion of material points. This representation as a continuum of rigid sections confers behavior close to articulated structures while preserving body continuity. The formalism thus captures all deformation modes of a rod—bending, torsion, extension, and shear—and provides an accurate kinematic description even under large deformations.

One of the major strengths of the Cosserat model lies in its use of local coordinates: each section is associated with a local reference frame in which the strain fields — curvature, torsion, shear, and extension — are defined as the generalized coordinates of motion. The global posture of the rod is then recovered through spatial integration of these local deformations from the base to the tip. This choice offers a direct and efficient description of deformations and a fundamental advantage: the deformation space becomes a vector space, facilitating coordinate interpolation and reducing the dimensionality of variables [103].

The Piecewise Constant Strain formulation [104], used in the present manuscript, discretizes the rod into constant-strain segments, significantly reducing the number of degrees of freedom while maintaining good accuracy. This approach improves computational efficiency and makes the model particularly well-suited to design and control needs. However, this formalism also has limitations. Piecewise Constant Strain formulation, relies on the assumption of constant strain per segment. While effective in capturing global deformations, the Cosserat rod theory assumes that each cross-section remains rigid and undeformed. This assumption limits its ability to accurately describe localized phenomena such as folds, local indentations, or complex contact interactions in highly constrained regions.

3.1.2 Fiber-based Geometric Representation

In this work, only the geometric scaffold inspired by Cosserat rod theory is retained. Rather than solving the full mechanical rod equations, the robot body is described through a set of longitudinal *fibers* that define its global geometry and orientation field. Each fiber carries local variables of position, orientation, and

curvature, enabling a continuous and compact reconstruction of the robot's tubular structure. This purely geometric adaptation provides the spatial organization necessary for the later introduction of a mechanical model, while maintaining a low computational cost.

3.1.3 FEM Model

The FEM is a numerical method that provides approximate solutions to partial differential equations over a spatial domain. While Cosserat models can also be formulated and solved using FEM [105], the term FEM in this work refers specifically to conventional 2D or 3D continuum models using tetrahedral, hexahedral, or triangular elements to capture local deformations and contacts. It has become a standard in many fields, with applications ranging from the simulation and validation of space structures during design and manufacturing phases [106] to fatigue life prediction of automotive components [107].

Its principle relies on discretizing the studied domain: rather than solving equilibrium equations continuously, the body is divided into a finite set of regions called elements, connected at points called nodes. The set of these nodes and elements forms the mesh. This approach simplifies resolution by ensuring local approximate equilibrium within each element [108, 109]. The main objective is to determine displacements at the mesh nodes. Once these displacements are calculated, stresses and strains throughout the domain can be deduced. Each element is characterized by mechanical properties defining its resistance to deformation, and the relationship between applied loads and resulting displacements is expressed as a coupled system of equations linking all mesh elements.

The FEM is particularly well suited to soft robotics, which is characterized by complex geometries, highly deformable materials, and nonlinear behaviors that are difficult to model analytically. FEM addresses these challenges thanks to several major strengths:

- **Geometric flexibility**: ability to model arbitrary, even very complex, shapes;

- **Local refinement**: possibility of refining the mesh in regions subject to large deformations to better capture mechanical gradients;
- **Rich material modeling**: support for hyperelastic, viscoelastic, and other nonlinear constitutive laws;
- **Consideration of complex interactions**: integration of contact, friction, and interactions with constrained environments.

However, this descriptive richness comes at a cost. Finer meshes and smaller time steps improve the accuracy of the results but significantly increase computational load and the risk of unstable behaviors arising from numerical errors. In addition, solvers must handle nonlinear behaviors for which convergence is not always guaranteed, and precise material characterization can be challenging. For these reasons, a compromise between model fidelity and computational feasibility is essential, particularly when rapidly exploring different configurations or preparing for applications in optimization or real-time control.

3.1.4 Hybrid Modeling through 1D/2D Coupling

Modeling flexible mechanical structures subjected to heterogeneous loading often involves mechanical behaviors of contrasting nature depending on the region considered. Some areas can be described with global models suited to regular, predictable deformations, while others require more detailed local formulations to capture strongly nonlinear phenomena such as contacts, folds, or geometric instabilities. In this context, relying on a single formalism is often insufficient: compact models struggle to reproduce fine phenomena, while high-fidelity approaches induce heavy numerical complexity.

Model coupling, particularly between local and global coordinate approaches, offers an effective strategy to overcome this limitation. It enables combining the advantages of geometrically compact models, providing efficient kinematic representation, with those of richer numerical methods capable of finely capturing local interactions and complex material behaviors. This strategy is commonly

adopted in multi-scale contexts or in the modeling of highly deformable biomechanical systems, where a balance between local precision and global efficiency is required.

In this perspective, Adagolodjo et al. [110] proposed a coupling method between a Discrete Cosserat Model and a FEM formulation based on tetrahedra, applied respectively to one-dimensional structures (actuators, cables, pre-curved rods) and to soft three-dimensional volumes. The Discrete Cosserat Model, formulated in local coordinates, provides an efficient representation of internal actuators while keeping reduced complexity, whereas FEM, expressed in global coordinates, describes the nonlinear behavior of soft material and its interactions with the environment. The joint use of these two descriptions, linked by kinematic constraints without requiring a common mesh, enriches the physical representation of the system while maintaining real-time simulation capabilities. Applied to devices such as soft fingers or multi-actuated tentacles, this coupling has proven particularly well suited to the simulation and control of complex soft structures.

This coupling principle finds a direct application in the growth-by-eversion robot studied here. The functional analysis of the system highlights three mechanically distinct zones, each associated with characteristic deformation regimes (Figure 3.1):

- **Stored zone**, corresponding to the material contained within the robot's body, compressed and subjected to internal stresses without interaction with the environment;
- **Eversion zone**, where the membrane turns inside out under pressurization, concentrating localized phenomena such as folds, contacts, and friction;
- **Deployed zone**, corresponding to the externalized portion of the robot, exposed to distributed loading and continuous contact with the environment.

The mechanical contrast between these regions justifies a hybrid modeling strategy (Table 3.1). The global geometry of the robot is represented with a fiber-based geometric model, inspired by the spatial structure of Cosserat rod theory but without its mechanical formulation. This 1D framework discretizes the robot

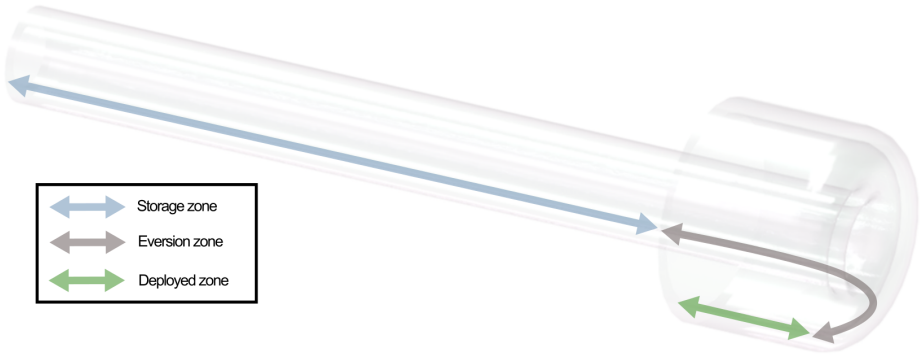


Figure 3.1: Representation of the three functional zones of the growth-by-eversion robot: stored zone (contained material), eversion zone (turning inside out under pressurization), and deployed zone (externalized body in contact with the environment).

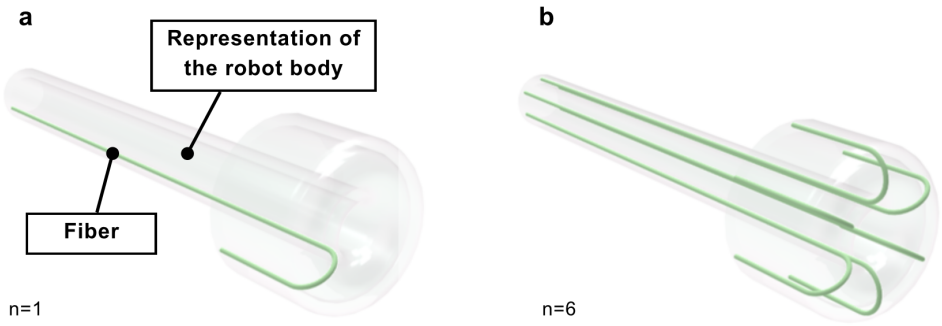


Figure 3.2: Fiber-based representation inspired by the geometric structure of Cosserat rod theory. (a) A single fiber showing its local reference frame and contribution to the robot's tubular envelope. (b) Arrangement of multiple fibers around the central axis, reconstructing the global geometry and kinematics of the robot.

into longitudinal fibers that collectively reconstruct its tubular shape and overall kinematics (Figure 3.2). Each fiber is defined by local variables of position, orientation, and curvature, providing an efficient description of smooth, large-scale deformations with low computational cost. This representation serves as the geometric backbone of the robot and is particularly suitable for the stored and deployed regions, where deformations are regular and smooth.

In contrast, the eversion zone involves strong nonlinearities, self-contact, and frictional effects that cannot be captured by a purely geometric model. This region is therefore modeled using a two-dimensional finite element formulation,

accurately reproducing the local mechanical response of the membrane and its interactions during eversion. The fiber-based and FEM models are geometrically coupled, ensuring smooth kinematic continuity and consistent stress transmission between regions.

This hybrid organization concentrates the descriptive richness where it is most needed—within the eversion zone—while simplifying the treatment of peripheral regions. It significantly reduces the number of degrees of freedom and computational cost without compromising the physical fidelity of the results.

Alternative strategies could have been considered, such as a purely Cosserat-based description of the entire structure or, conversely, a full FEM model with adaptive meshing. However, the former would fail to capture the localized nonlinearities and complex contact phenomena at the eversion front, while the latter would entail prohibitive computational costs. The proposed hybrid coupling thus represents a deliberate compromise, exploiting the complementary strengths of both formalisms to balance precision, efficiency, and robustness—an essential condition for the modeling of eversion-based soft robotic systems.

Functional zones	**Model used**	**Justification**
Stored	Fiber-based (1D)	Smooth global deformations, low complexity, negligible environmental interactions
Eversion	FEM (2D)	Localized nonlinear deformations, folding, contact, friction
Deployed	Fiber-based (1D)	Continuous kinematics, distributed loading, compatibility with control strategies

Table 3.1: Distribution of models according to the functional zones of the robot.

3.1.5 Fiber-based Geometric Model

Definition of Fiber Geometry

The initial geometry of the robot is constructed using a discrete representation based on a set of longitudinal fibers, denoted F. This approach represents the robot not as a continuous volume but as a geometric skeleton composed of reference lines from which its shape and deformations can be reconstructed. Each fiber, denoted F_i where $i \in [0, F-1]$, follows the shape of the robot and describes its local geometry through its position, orientation, and curvature. Once these fibers are defined, the robot surface is obtained by interpolation between neighboring fibers and then converted into a triangulated mesh representing the membrane. This method provides the geometric foundation of the robot, used as the initial state for simulating the eversion process.

In our implementation, the arrangement of the fibers at the robot base is defined in the transverse plane (y, z), perpendicular to the deployment axis x. This plane corresponds to the robot cross-section at its base, where the fibers are initialized. They are distributed uniformly along a circle of radius R centered on the x-axis to ensure axial symmetry of the model. Each fiber F_i is associated with an angle θ_{F_i}, which determines its position on the circular section (Equation 3.1).

$$\theta_{F_i} = \frac{2\pi i}{F} \tag{3.1}$$

From this angle, the coordinates of each fiber base are computed in the (y, z) plane (Equation 3.2).

$$x_i = 0, \qquad y_i = R\cos(\theta_{F_i}), \qquad z_i = R\sin(\theta_{F_i}) \tag{3.2}$$

The positions (x_i, y_i, z_i) thus obtained define the first node $N_{F_i,0}$ of each fiber, expressed in the global reference frame of the robot. This node corresponds to the fixed point in the base plane and serves as an anchor for the fiber construction (Figure 3.3).

Each fiber is then discretized into a set S of elementary sections, whose number -identical for all fibers- is defined by the user according to the desired modeling resolution (Figure 3.4). These sections, denoted $S_{F_i,j}$ for $j \in [0, S-1]$, are

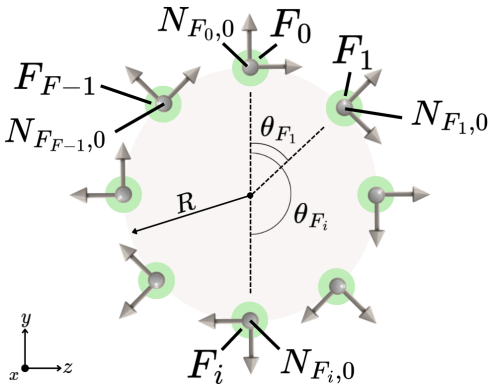


Figure 3.3: Definition of the initial fiber arrangement at the robot base. The robot geometry is constructed from a set F of fibers F_i, uniformly distributed along a circular section of radius R in the transverse (y, z) plane. The global reference frame is defined such that the x-axis corresponds to the robot's deployment direction, while the (y, z) plane represents the base cross-section. Each fiber F_i is associated with an angle θ_{F_i} defining its position on the circle. The first node $N_{F_i,0}$ of each fiber lies on this circular section and serves as the fixed anchor point in the base plane. The schematic illustrates the notation used for boundary fibers (F_0, F_{F-1}) and intermediate ones (F_i), as well as their corresponding base nodes ($N_{F_0,0}$, $N_{F_i,0}$, $N_{F_{F-1},0}$).

connected by nodes $N_{F_i,j}$ with $j \in [0, S]$, distributed along the fiber length L_{F_i}.

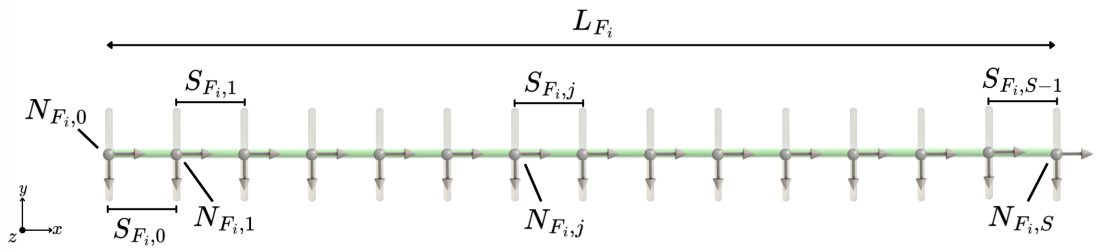


Figure 3.4: Definition of the fiber discretization. Each fiber F_i, of total length L_{F_i}, is divided into a set S of sections $S_{F_i,j}$ with $j \in [0, S-1]$, connected by nodes $N_{F_i,j}$ with $j \in [0, S]$. The schematic illustrates the notation used for intermediate (j) and boundary indices $(0,\ 1,\ S-1,\ S)$ along the fiber.

In the initial configuration, the robot is fixed at its base: a portion of the membrane is already inverted (deployed zone), while the rest remains non-inverted (storage zone). Between these two regions lies the eversion zone, which represents the geometric transition between the two states. To represent this transition in the model, a local curvature is imposed on each fiber (Figure 3.5). This curvature reproduces the geometric fold associated with the eversion phenomenon.

Its position and extent are delimited by two specific nodes, $N_{F_i,BE}$ (Beginning of Eversion) and $N_{F_i,EE}$ (End of Eversion), defining the eversion section, denoted S_e. The curvilinear distance separating these two nodes corresponds to the total length L_e of this section.

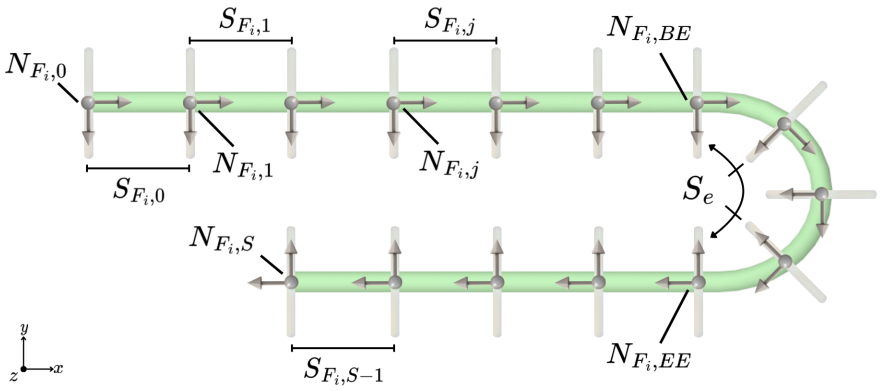


Figure 3.5: Fiber representation of the eversion zone. The fiber consists of sections $S_{F_i,j}$ connected by nodes $N_{F_i,j}$. The base is represented by $S_{F_i,0}$ and $N_{F_i,0}$. The eversion zone is represented by S_e, starting at $N_{F_i,BE}$ and ending at $N_{F_i,EE}$.

The local deformation of each fiber is described by the curvature vector $\mathbf{q}(s) = (q^x, q^y, q^z)$, defined in the local reference frame of the fiber, following a geometric formulation inspired by Cosserat rod theory. In the initial configuration, only the component q^y is nonzero, as the bending is applied in the (x, y) plane. The curvature associated with the eversion zone, denoted q_e^y, is constant along the length L_e and defines a 180° fold (π radians) (Equation 3.3).

$$q_e^y = -\frac{\pi[rad]}{L_e[m]} \tag{3.3}$$

The value of L_e directly controls the shape of the fold: a short length produces a sharp curvature, while a longer length results in a smoother and more gradual transition.

The section S_e can, if necessary, be further discretized into multiple sub-sections of elementary length l_e. When several sub-sections are used, the sum of their lengths reconstructs the total length L_e, and the sum of their angular contributions must

recover the global 180° rotation (Equation 3.4).

$$\sum_{i=0}^{j} q_{e+i}^{y} L_{e+i} = -\pi. \tag{3.4}$$

Each fiber, therefore, describes a local half-circle corresponding to the initial eversion fold. Once these curvatures are defined for all fibers, the complete robot geometry is reconstructed by integrating the local orientations, providing a coherent geometric basis for generating the membrane mesh and initializing the mechanical simulation.

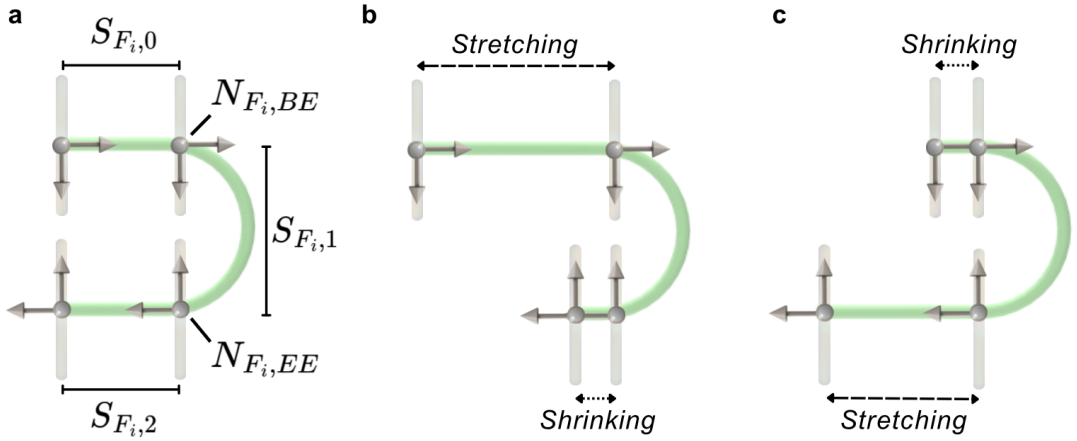


Figure 3.6: (a) The fiber of the robot is divided into three sections: $S_{F_i,0}$ (pre-eversion), $S_{F_i,1}$ (eversion), and $S_{F_i,2}$ (post-eversion). (b) Forward motion is obtained by increasing the distance between $N_{F_i,BE}$ and $N_{F_i,EE}$, which results in $S_{F_i,0}$ stretching and $S_{F_i,2}$ shrinking. (c) Conversely, backward motion is obtained by decreasing this distance, leading to $S_{F_i,0}$ shrinking and $S_{F_i,2}$ stretching.

Creation of eversion movement

To reproduce the robot's eversion motion, the curvilinear coordinates associated with nodes $N_{F_i,BE}$ and $N_{F_i,EE}$ are dynamically adjusted (Figure 3.6): their increase reflects forward progression of the robot, while their decrease corresponds to retraction. The discretization of each fiber is then updated accordingly. Since membrane points are distributed along the fibers according to their curvilinear abscissa, shifting the eversion zone forward or backward naturally produces the progressive turning of the membrane, thereby reproducing the eversion phe-

nomenon. In practice, a discretization into three sections $S_{F_i,j}$ per fiber proved sufficient to describe the global kinematics: $S_{F_i,0}$ corresponds to the pre-eversion portion, $S_{F_i,1}$ to the eversion zone itself, and $S_{F_i,2}$ to the already deployed portion.

Geometric Implementation in SOFA[2]

The numerical implementation of the fiber-based geometric model in SOFA relies on a progressive construction, starting from independent elementary units and leading to a global structure that can later be exploited within an FEM framework (Figure 3.7) (Appendix B – Algorithm 1).

1. **Definition of the fiber bases:** Each fiber is initialized within a hierarchical block named *Base*, inside which the base of the fiber is represented by a `Rigid3d MechanicalObject` (*baseMO*). In SOFA, the `MechanicalObject` defines and stores the degrees of freedom of a model, namely the positions and orientations of its elements. A `FixedConstraint` is applied to this base to keep it immobile, simulating the anchoring of the robot to its pressurization base. All bases are regularly distributed around the circumference of the structure to recreate the tubular geometry of the robot (Section 3.1.5). Each fiber therefore has its own local frame and acts as an autonomous entity within the scene.

2. **Local coordinates for each fiber:** From the base, each fiber is extended with a block named *FiberCoordinate*. This block contains a `Vec3d MechanicalObject`, which stores the local geometric parameters of the fiber, including its position, orientation, and curvature. In this formulation, these variables are limited to bending and torsion components, which dominate the deformation of the fibers during eversion. The constitutive law `BeamHookeLawForceField` computes the internal elastic forces by establishing the relationship between strain (bending and torsion) and stress, expressed as the density of internal forces along the fiber.

[2]For readers interested in reproducing the implementation or exploring the simulation in greater detail, a comprehensive description of the SOFA hierarchical architecture, as well as the algorithms developed in this work, is provided in Appendices A and B.

3. **Reconstruction of fiber frames:** For each fiber, the local coordinates are used to reconstruct a series of three-dimensional frames within a block named *FiberFrame*. This block contains a `Rigid3d MechanicalObject` describing the frames distributed along the fiber, together with a `DiscreteFiberMapping`. In SOFA, a mapping transfers mechanical quantities such as positions, velocities, or forces between different representations. Here, it converts the local strain coordinates (bending and torsion) into global kinematic quantities (positions and velocities) of the reconstructed frames. As a result, each section of the fiber is represented by a well-defined position and orientation in the simulation space, forming a complete geometric description of the structure.

4. **Assembly via mapping:** Once the fibers are individually reconstructed, they are synchronized within a block named *FiberMappingGeneral*. This block contains a global `Rigid3d MechanicalObject` (*generalMO*), associated with a `SubsetMultiMapping` that aggregates the frames of all fibers to provide the global position of the robot. From this representation, an *OriginalMesh* block is introduced and linked to the fiber-based model through an `IdentityMapping`, which directly copies the positions from one object to another. This mapping converts the global `Rigid3d MechanicalObject` into a `Vec3d MechanicalObject`, whose coordinates define the vertices of the surface mesh in `MeshTopology`.

5. **Eversion motion:** The coordinated movement of the fibers is implemented by a Python `Controller`, which enables user-defined updates during the simulation. The controller sequentially accesses the *Base*, *FiberCoordinate*, and *FiberFrame* blocks, allowing the eversion zone to progress by incrementing the curvilinear abscissas between the start and end eversion nodes until the total length is reached. Beyond this limit, it imposes a distal preformation by canceling torsion and bending while adjusting curvature around the z-axis. Conversely, the controller can retract the eversion zone by decrementing the curvilinear abscissae or by releasing the preformation. After each update, the `DiscreteFiberMapping` is reset to propagate the modifications to the reconstructed frames and the global mesh.



Figure 3.7: Illustration of fiber deployment during the eversion motion simulated in SOFA. Panel (a) shows the initial stage of deployment at the onset of eversion, while panel (b) depicts the advanced stage, where the fibers are deployed.

3.1.6 Definition of the FEM on the Fiber-based Geometry

General concept of the membrane

From a mechanical perspective, the quasi-static equilibrium of the membrane results from four types of forces (for a 3D position of the nodes $\mathbf{x}$):

- Internal forces, denoted $\mathbf{F}(\mathbf{x})$, which depend on the constitutive material of the membrane;
- Pressure forces, denoted $\mathbf{P}(\mathbf{x})$, applied inside the structure and responsible for deploying new material at the eversion point;
- Self-collision forces of the membrane and associated friction, denoted $\mathbf{H}^T\boldsymbol{\lambda}$;
- Boundary conditions $\mathbf{B}(\mathbf{x})$, which also play a determining role. In some eversion robot concepts, a motor is placed at the robot's base to counteract the eversion pressure and precisely control the eversion point.

The internal forces of the membrane are computed using FEM model based on triangular elements. A linear elastic constitutive law is assumed under the small strain, large displacement framework, where elements can undergo significant rigid body motion while material strains remain small. Only in-plane forces are considered, and each element is allowed to rotate freely with respect to its neighbor along the shared edge, thereby reproducing the natural flexibility of thin materials. However, this approach introduces a dependency on mesh resolution. Although the FEM implementation supports advanced constitutive laws

such as hyperelasticity or viscoelasticity, a linear elastic formulation was deliberately adopted at this stage. This choice ensures numerical tractability of the hybrid fiber–FEM framework and provides a sufficient first-order approximation to capture global deployment dynamics. The simplification is assumed as part of a progressive modeling strategy: once the hybrid framework has been validated in its global functioning, more complex constitutive laws (e.g., hyperelastic formulations required for deformable elastomers) may be introduced in subsequent stages to refine the prediction of local stresses and contact forces.

Pressure forces are distributed proportionally to the surface area of each triangle. Self-collisions are handled through Lagrange multiplier constraints [111]. Finally, boundary conditions are defined by the coupling model.

The complete set of forces is computed in the 3D space of FEM nodes by solving the quasi-static nonlinear equilibrium, i.e., by determining $\mathbf{x}$ such that:

$$\mathbf{F}(\mathbf{x}) + \mathbf{P}(\mathbf{x}) + \mathbf{H}^T\boldsymbol{\lambda} + \mathbf{B}(\mathbf{x}) = 0 \tag{3.5}$$

Coupling between the membrane and the fibers

The FEM model is then coupled to the fiber-based geometric representation through a direct node-to-node correspondence and the introduction of springs ensuring the link between the two representations (Figure 3.8). The FEM analysis is restricted to the eversion zone ($S_{F_i,1}$), considered quasi-static, where the balance between elasticity, pressure, and local membrane constraints must be accurately evaluated. The pre-eversion ($S_{F_i,0}$) and post-eversion ($S_{F_i,2}$) zones, whose geometry remains relatively stable from one configuration to another, are described by the fiber-based representation and therefore constitute the so-called kinematic regions.

The kinematic model also provides the initial configuration of the FEM mesh as well as continuous boundary conditions ensuring coherence across zones. Both models share the same discretization step, which establishes a direct correspondence between nodes. Each membrane point k is therefore associated with a kinematic position $\mathbf{p}_k$ and an FEM position $\mathbf{x}_k$. The link is ensured by introduc-

ing springs:

$$\mathbf{B}(\mathbf{x}) = \sum_k \mathbf{k}_k(\mathbf{p}_k - \mathbf{x}_k) \tag{3.6}$$

where $\mathbf{k}_k$ is defined as a scalar coefficient identical in the three directions, allowing control over the degree of constraint between models.

In the kinematic zones, a high stiffness is assigned to $\mathbf{k}_k$, forcing $\mathbf{x}_k$ to closely follow $\mathbf{p}_k$ (Figure 3.1). In the quasi-static zone, the stiffness is set to zero, allowing the membrane to reach equilibrium under the combined effects of elastic forces, internal pressure, and self-collisions. This coupling scheme concentrates computational resources on the critical zone while maintaining a consistent description of the global behavior.

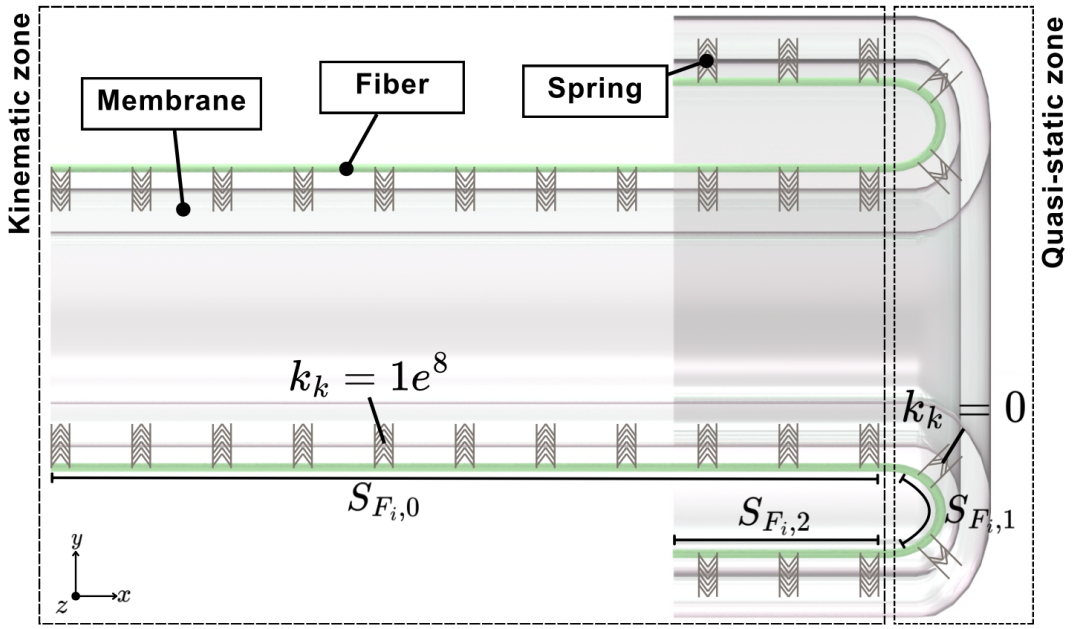


Figure 3.8: The coupling model ensures the interaction between the fiber and the membrane. Rigid springs ($\mathbf{k}_k = 10^8$) are used in the kinematic zones, corresponding to the pre-eversion ($S_{F_i,0}$) and post-eversion ($S_{F_i,2}$) regions, in order to tightly constrain the FEM nodes to the prescribed kinematic motion. In contrast, the eversion zone ($S_{F_i,1}$) is treated as quasi-static: relaxed springs ($\mathbf{k}_k = 0$) are applied to allow the membrane to deform freely under elastic, pressure, and self-collision forces. This relaxation avoids over-constraining the system and enables natural eversion.

FEM implementation in SOFA[3]

The FEM layer is implemented in the *MeshSurfacic* block in order to physically model the membrane, relying on the *OriginalMesh* block that provides the surface representation of the structure derived from the fiber-based geometry (Figure 3.9) (Appendix B - Algorithm 2).

1. **Geometric support:** The *OriginalMesh* block, linked to the fiber-based structure (Sec. 3.1.5), provides the nodal coordinates that serve as the geometric reference for the surface mesh. These coordinates are then used in the *MeshSurfacic* block to construct the visible envelope of the robot.

2. **Solvers and integration:** The *Solvers* block defines the numerical resolution scheme of the simulation. It combines an `EulerImplicitSolver`, which performs time integration of the mechanical equations, with Rayleigh damping (`rayleighStiffness` = 0.2, `rayleighMass` = 0.1) to stabilize the dynamic response. A `SparseLDLSolver` ensures efficient linear resolution, and a `GenericConstraintCorrection` manages the Lagrangian constraints. The time step is set to $\Delta t = 0.01$ s, providing a balance between precision and computational cost.

3. **Surface mesh:** The *FEMMesh* block contains a `Vec3d MechanicalObject` (*femMO*) that stores the positions of the finite element mesh vertices. Their connectivity is defined by a `MeshTopology`, which specifies how nodes are connected to form triangular elements. To maintain geometric coherence with the fiber-based structure, a `RestShapeSpringsForceField` links *femMO* to the reference configuration of *OriginalMesh*, ensuring a consistent coupling between the fiber-based representation and the deformable membrane.

4. **Mechanical behavior and pressurization:** The membrane response is simulated using a `TriangleFEMForceField`, parameterized with a thickness $t = 0.005$, a Young's modulus $E = 5 \times 10^{10}$ and a Poisson's ratio $\nu = 0.46$,values representative of LDPE chosen here to model a commonly

[3]For readers interested in reproducing the implementation or exploring the simulation in greater detail, a comprehensive description of the SOFA hierarchical architecture, as well as the algorithms developed in this work, is provided in Appendices A and B.

used polymer material. Internal pressure is applied through a uniform `SurfacePressureConstraint` set at 10 Pa, corresponding to the pressurization required for robot deployment.

5. **Collisions and numerical robustness:** Contact interactions are managed by the `CollisionPipeline`, which orchestrates the different stages of collision handling. Broad-phase detection (`BruteForceBroadPhase`) identifies potential contacts, followed by narrow-phase refinement (`BVHNarrowPhase`) and local distance evaluation (`LocalMinDistance`). The `DefaultContactManager` then generates the necessary constraints to resolve contacts. The membrane is equipped with collision models (`Triangle`, `Line`, and `PointCollisionModel`) that enable accurate detection and stable physical response across multiple scales.

6. **Spring control:** The Python controller also governs the coupling between the fiber-based geometric model and the surface mesh by defining a spatially varying stiffness field for the spring system. A stiffness array is created, with a baseline value applied globally, and locally adjusted to reinforce specific regions or relax the central area while stiffening the ends. The controller can record mesh positions to monitor and analyze deformation. In this way, it simultaneously drives the forward or backward eversion, applies distal preformation, and dynamically tunes the stiffness of the surface mesh to ensure smooth and stable behavior during simulation.

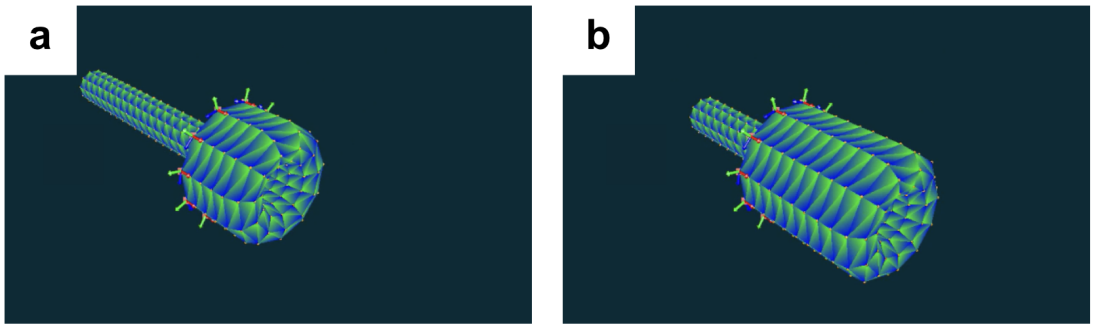


Figure 3.9: Illustration of mesh deployment during the eversion motion simulated in SOFA. Panel (a) shows the initial stage of deployment at the onset of eversion, while panel (b) depicts an advanced stage, where the mesh is deployed.

3.2 Preliminary Numerical Validation

Before addressing realistic vascular scenarios, preliminary validations were carried out to verify two key aspects of the hybrid model. The reproduction of characteristic eversion shapes confirms that the fiber-based representation of the stored and deployed zones provides a consistent kinematic input to the FEM eversion region, leading to morphologies in agreement with experimental observations. The test through a constrained passage, on the other hand, validates the ability of the FEM formulation to handle localized deformations and contacts, while ensuring that the spring-based coupling transmits forces correctly between zones. These steps represent a first principle validation, aimed at establishing the reliability of the model before extending its application to complex anatomical cases.

3.2.1 Validation on eversion shapes

Three eversion shapes frequently observed in experiments were selected as references: random, triangular, and linear. They correspond to distinct ways in which the robot body unfolds over itself, and can be grouped into two categories (Figure 3.10):

- **Free shape** (random): folds spontaneously appear at the eversion point without any particular constraint;
- **Imposed shapes** (triangular and linear): the deployment geometry is influenced by material conditions. The triangular shape is favored by compacting of the membrane or confinement constraints, while the linear shape emerges when a motorized drive enforces a straight-line deployment.

These experimental observations were then used as a basis to define sequences of eversion lengths L_e in order to reproduce them numerically. In this context, the robot body is represented by 16 fibers, where the eversion zone of each fiber is described by sections of length L_e. Three characteristic values ($L_{e,\min}$, $L_{e,\mathrm{mid}}$, $L_{e,\max}$) were defined to generate different configurations (Figure 3.11):



Figure 3.10: Reference eversion shapes experimentally observed in eversion-based robots : (a) random, (b) triangular, (c) linear. Shape (a) appears spontaneously, while shapes (b) and (c) result from specific storage or actuation conditions.

- **Random shape**: obtained when all elementary sections are assigned the same L_e value, without alternation of lengths;
- **Triangular shape**: obtained by alternating contrasted lengths ($L_{e,\min} - L_{e,\text{mid}} - L_{e,\max}$);
- **Linear shape**: obtained by a succession of long sections ($L_{e,\max}$), framed by shorter segments ($L_{e,\min}$).

3.2.2 Validation in constrained environments

The model was then evaluated in a restricted environment, simulating the traversal of narrowed passages. To this end, a localized constriction was introduced in the surrounding medium, locally reducing the available space according to different narrowing ratios τ_r (25%, 35%, and 45% of the robot's initial diameter). The robot membrane was represented as a thin material, characterized by a Young's modulus $E = 5 \times 10^9$ Pa, a Poisson's ratio $\nu = 0.45$, and a thickness $h = 30, \mu$m, values corresponding to the properties of LDPE, commonly used in the eversion robot literature.

During traversal, the membrane comes into contact with the walls and exerts a pressure proportional to the contact force F, whose intensity increases with the narrowing ratio (Figure 3.12). More specifically, simulations indicate that $F = 10.4$ N for $\tau_r = 25\%$, $F = 79.4$ N for $\tau_r = 35\%$, and $F = 167.9$ N for $\tau_r = 45\%$. The analysis shows a local redistribution of deformations: the vertical section V_s, directly constrained by the passage, compresses until it matches the imposed

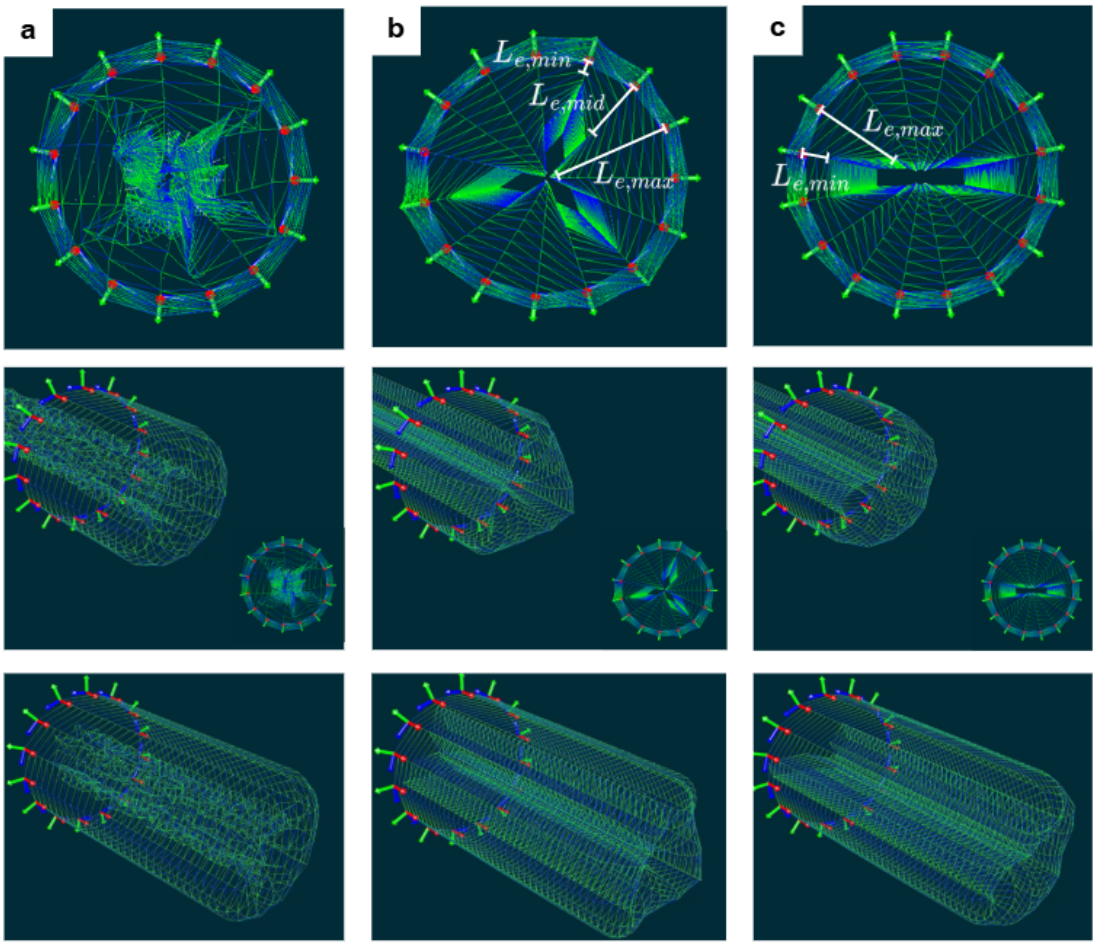


Figure 3.11: Numerical reconstruction of eversion shapes by combining elementary lengths $L_{e,\min}, L_{e,\mathrm{mid}}, L_{e,\max}$. Three configurations are obtained: (a) random, with constant L_e; (b) triangular, produced by alternating contrasted lengths; (c) linear, built from a succession dominated by long sections framed by shorter segments.

narrowing, while the horizontal section H_s, unconstrained by external contact, retains its initial dimension. This behavior is not only visible in simulation but was also qualitatively observed in experiments, where the robot exhibited the same diameter reduction at the constriction.

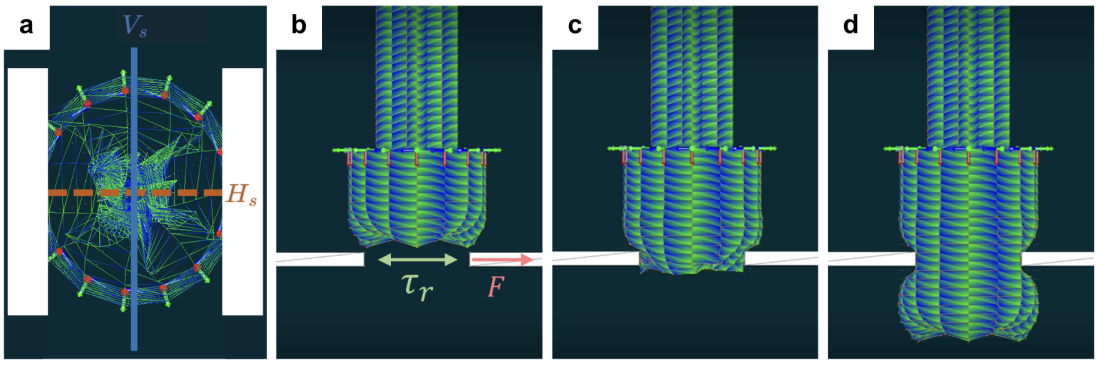


Figure 3.12: Simulation of the robot traversing a constrained passage: (a) identification of vertical section V_s and horizontal section H_s, (b) indication of the narrowing ratio τ_r and contact force F, (c) initial engagement phase of the robot into the slit, (d) complete passage through the constriction.

3.3 Conclusion

This chapter has established the foundations of a simplified, robust, and efficient numerical framework for simulating eversion. The objective was not merely to introduce an additional model, but to develop a tool specifically tailored to the analysis of mechanical constraints concentrated in the critical eversion zone, where saline pressurization increases membrane stiffness and raises the risk of vascular injury, as evidenced during cadaveric experiments.

The adopted strategy relied on a hybrid approach combining two complementary formalisms. The fiber-based representation was applied to the stored and deployed regions, characterized by continuous, large-scale bending and twisting and negligible local strain, making computational efficiency essential. In contrast, the finite element method was restricted to the eversion zone, in order to capture localized and highly nonlinear mechanisms such as membrane inversion, fold formation, and multiple contact interactions. This methodological compromise—concentrating complexity where it is indispensable while simplifying elsewhere—distinguishes the proposed approach from real-time simulators, which often sacrifice physical fidelity, and from full finite element models, whose prohibitive computational cost limits parametric exploration.

Implementation within the SOFA framework exploited the respective advantages of each formalism by assigning to each region of the robot the most appropriate

model. The geometry was defined through a radial bundle of fibers reconstructing the tubular envelope, whose discretization and curvature parameterization enabled explicit control of both shape and eversion motion. The "fiber–FEM" coupling was achieved by a node-to-node correspondence combined with springs of spatially varying stiffness: high in dynamic regions, reduced to zero in the quasi-static eversion zone. This configuration allowed the membrane to reach equilibrium under the combined effects of elastic forces, internal pressurization, and self-collisions.

Preliminary numerical validations confirmed the relevance of the framework. The model reproduced eversion patterns observed experimentally (random, triangular, linear) and revealed a redistribution of deformations when passing through constrained environments, with the vertical section compressed within the constriction while the horizontal section preserved its dimension—consistent with qualitative experimental observations.

These validations, however, were conducted under exploratory conditions, involving the use of a reference polymer (LDPE) and a range of internal pressures of limited amplitude, selected to stabilize the coupling and verify the consistency of force computation. Such conditions represent a methodological prerequisite, aimed at isolating the fundamental mechanisms of eversion before introducing more representative parameters. Future developments will incorporate materials relevant to the clinical application, physiologically realistic pressure ranges, and constitutive laws better suited to thin structures, thereby improving the representation of local stresses and curvature effects. Systematic comparison with experimental data will constitute a decisive step to confirm the robustness of the framework and to consolidate its clinical significance.

In this continuity, the next chapter deepens the framework by refining the balance between accuracy and computational performance, while engaging a first experimental validation to directly assess the concordance between simulation and reality.

Chapter 4

Modeling Elastic Wall Mechanics for an Everting Robot

This chapter details the enhancements implemented in the previous model to improve its accuracy and better capture the robot's mechanical behavior. Chapter 3 had introduced a hybrid framework combining a fiber-based geometric representation, which facilitated the kinematic and geometric definition of the robot, with a local finite element representation of the membrane. This approach provided an effective first step in structuring the modeling, but it revealed a major limitation: the mechanical description of the membrane remained approximate, particularly when capturing local phenomena.

In practice, the robot is fluid-actuated, which differs fundamentally from conventional pneumatic pressurization. The use of an incompressible fluid alters the way pressure is distributed along the wall and amplifies local deformation effects. As a result, internal pressurization induces complex membrane deformations and local variations in rigidity, particularly in contact regions where compliance plays a key role in reducing friction and ensuring smooth eversion. Accurately reproducing these elastic behaviors is therefore essential to predict the robot's mechanical response, improve contact realism, and guide the design toward safer and more controllable interactions within confined environments.

To address this limitation, a unified thin-shell finite element formulation is proposed. It offers a more faithful mechanical representation of the thin-walled

tubular structure of the robot, while retaining a similar level of numerical robustness and parameterization compared to the hybrid model. The improvements introduced are structured around three complementary axes:

- **Mesh geometry (Section 4.1):** The initial configuration of the robot, when resting on its base, is critical for mesh quality and simulation stability. To ensure precise control of membrane curvature and orientation, the fiber-based approach introduced in the previous chapter is used as a geometric generation tool. In this chapter, fibers serve exclusively for shape construction and are subsequently removed, without contributing to the eversion dynamics;

- **Mechanical modeling (Section 4.2):** The model relies on a thin-shell finite element formulation, particularly suited to thin-walled structures. A surface-based model such as the `TriangularFEMForceField` can represent membrane forces but neglects the contribution of out-of-plane bending moments, which are crucial for describing the behavior of a thin pressurized membrane. A shell model is therefore more appropriate, as it accounts for both membrane forces and bending stiffness, providing a more accurate representation of curvature, buckling, and local deformations associated with eversion [112, 113];

- **Eversion dynamics (Section 4.3):** The transition of the robot from a folded state to a deployed configuration under internal pressurization represents a major challenge. To model this process, specific zones are defined to progressively release mechanical constraints. This transition is controlled by a numerical guide, which ensures stable deployment consistent with mechanical laws, while preventing numerical instabilities.

These three optimizations mark a shift toward a unified thin-shell formulation that ensures a continuous and mechanically consistent representation of the membrane by integrating tensile and bending effects. This approach addresses the challenge of modeling a highly thin membrane undergoing local inversions while maintaining numerical robustness. Complexity is thus concentrated within the eversion zone, preserving the overall efficiency of the model.

4.1 Mesh geometry using fiber analogy

4.1.1 Principle & Requirements

In Chapter 3, the hybrid approach exploited fibers as dynamic entities, but they also played a decisive role in mesh generation. They enabled direct control over element density, orientation, and geometric accuracy, ensuring the production of nearly equilateral triangles, which is essential for the numerical stability of the model.

In the present chapter, this principle is retained but adapted: fibers are no longer used as mechanical entities, but solely as geometric scaffolds to define the initial shape of the robot and guide the mesh construction. They determine the overall position and orientation of the structure, allowing the generation of either a straight configuration or a preformed configuration with a predefined distal curvature [34] (Figure 4.1). In both cases, the robot is considered already everted and fixed to a base, consistent with its actual condition when attached to the pressurization station. Once the geometry is defined and the mesh is constructed, the fibers are removed and do not intervene in the physical simulation. This choice is motivated by the fact that keeping the fibers as dynamic entities entails a considerable computational cost, without providing any direct benefit to mechanical accuracy, which is now consistently described by the thin-shell formulation.

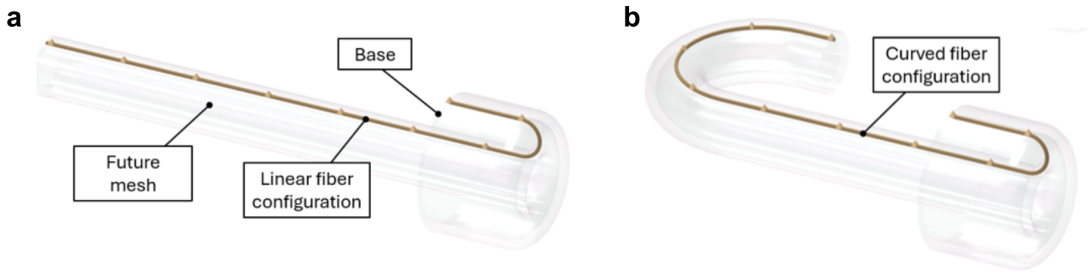


Figure 4.1: Fiber configurations defining the initial geometry of the eversion-based robot. Fibers serve as a temporary framework for shaping the future mesh. (a) The linear fiber configuration maintains a straight structure, while (b) the curved configuration introduces a predefined distal curvature. The robot is fixed to a base, reflecting its initial state in the simulation.

4.1.2 Modeling

For a straight robot, the geometric description follows that defined in Section 3.1.5, based on a set F of fibers F_i connecting their sections $S_{F_i,j}$ through nodes $N_{F_i,j}$ that describe the local position and orientation of the membrane. Each fiber is associated with a curvature vector along the y-axis, denoted q_e^y, representing the eversion zone of the robot in its initial state when fixed at its base.

Building on this reference description, the model was extended to include a curved distal portion of the robot (Figure 4.2), enabling the representation of preformed trajectories required for navigating tortuous or anatomically constrained environments. In this framework, the fiber F_0 is chosen as a reference fiber and associated with the desired radius of curvature, denoted R_{C_0}. Located laterally on the circumference, it serves only as a geometric reference: it allows the radii of curvature of the other fibers F_i to be deduced as a function of their transverse position y_i in the (y, z) plane. The objective is that all fibers, although vertically offset from one another, follow a coherent circular arc and end at the same level along the x-axis, thus forming a continuous body.

The radius of curvature of each fiber is then adjusted according to its relative position with respect to the reference fiber F_0 (Equation 4.1). This dependence on the sign of y_i ensures a geometric symmetry between the fibers located on either side of the mid-plane.

$$R_{C_i} = \begin{cases} R_{C_0} + (y_0 - y_i), & \text{if } y_i > 0 \\ R_{C_0} + |y_0 + y_i|, & \text{if } y_i < 0 \end{cases} \tag{4.1}$$

Once these radii are established, the corresponding arc length is derived for each fiber (Equation 4.2).

$$L_{C_i} = \pi \cdot R_{C_i} \tag{4.2}$$

This relationship follows from the geometric definition of the length of a circular arc, $L = R \cdot \theta$, considering here a curved portion covering an angle of π radians, i.e., a 180° curvature at the distal end of the robot.

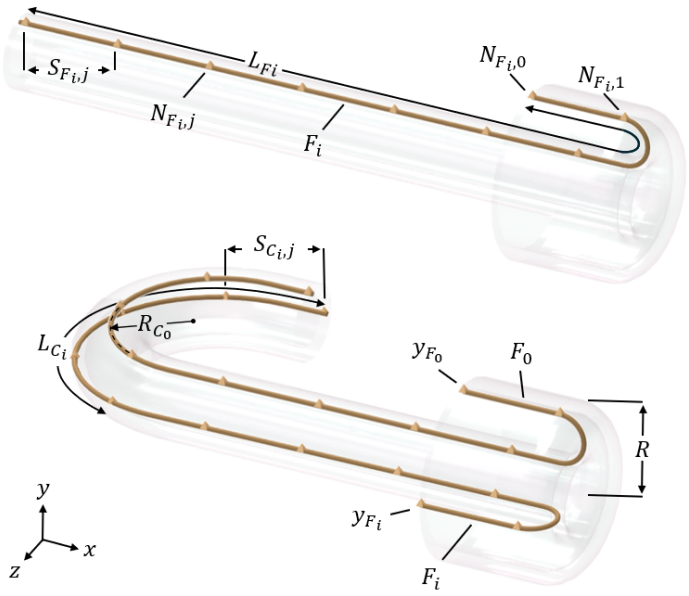


Figure 4.2: Schematic representation of the fiber-based robot structure. Each fiber F_i has a total length L_{F_i} and is discretized into $S_{F_i,j}$ sections, connected by nodes $N_{F_i,j}$, where $N_{F_i,0}$ is fixed at the base. When a distal curvature is introduced, the reference fiber F_0, positioned at y_{F_0}, is assigned a target curvature radius R_{C_0}. Each other fiber F_i is then evaluated relative to this reference in order to compute its own curvature radius R_{C_i}, arc length L_{C_i}, and curved sections $S_{C_i,j}$ composing the curved portion C_i.

To discretize this curved portion with a density equivalent to that of the straight region, the unit section length, denoted L_{unit}, is introduced. It corresponds to the average section length in the straight case (Equation 4.3).

$$L_{\text{unit}} = \frac{L_{F_i}}{S} \tag{4.3}$$

The number of sections S_{C_i} required to model the curved portion is then determined by the ratio between the arc length L_{C_i} and this unit length L_{unit} (Equation 4.4). This approach ensures consistent discretization between the straight and curved regions, guaranteeing mesh regularity across the entire geometry. Each curved portion C_i is thus discretized into S_{C_i} sections, denoted $S_{C_i,j}$, to preserve continuity with the straight region.

$$S_{C_i} = \frac{L_{C_i}}{L_{\text{unit}}} = \frac{\pi \cdot R_{C_i}}{L_{\text{unit}}} \tag{4.4}$$

Once the geometry is discretized, the spatial orientation of each fiber's curvature must be defined. To achieve this, the fiber geometry introduced in the previous chapter is reused. The set of fibers is distributed in the transverse (y, z) plane following a circular arrangement of radius R, centered on the main x-axis to ensure axial symmetry. Each fiber F_i is thus associated with an angle θ_{F_i}, expressing its angular position around the x-axis (Equation 4.5).

$$\theta_{F_i} = \frac{2\pi i}{F} \tag{4.5}$$

The bending direction is described using the curvature vector $\mathbf{q}(s) = (q^x, q^y, q^z)$, characterizing the local rotation of the fiber section along the arc length. This vector does not affect the magnitude of the curvature, already defined by R_{C_i}, but rather its spatial orientation in the global frame. It is then instantiated for each fiber F_i along its curved portion, denoted C_i, previously defined by its radius R_{C_i} and arc length L_{C_i}.

For each fiber F_i, the projected components of the curvature vector, denoted $\mathbf{q}^y_{C_i}$ and $\mathbf{q}^z_{C_i}$, are calculated based on its angular position θ_{F_i} in the transverse (y, z) plane (Equation 4.6).

$$\begin{aligned} \mathbf{q}^y_{C_i} &= \sin(\theta_{F_i}) \left[\left(\frac{S_{C_i}}{L_{C_i}} \right) \pi \right] \\ \mathbf{q}^z_{C_i} &= -\cos(\theta_{F_i}) \left[\left(\frac{S_{C_i}}{L_{C_i}} \right) \pi \right] \end{aligned} \tag{4.6}$$

The factor $\left(\frac{S_{C_i}}{L_{C_i}}\right)\pi$ expresses the local distribution of curvature along the S_{C_i} sections of the curved portion C_i, ensuring a total rotation of π radians for each fiber. Consequently, each fiber is characterized by its own bending direction, oriented according to its circular position around the main axis.

The combination of these local curvatures defines a continuous three-dimensional field ensuring the spatial coherence of the bending in the preformed robot. This field governs the global geometry of the tube and provides the geometric foundation for reconstructing the complete preformed robot prior to mesh generation.

4.1.3 Implementation in SOFA[1]

In this approach, the implementation in SOFA still relies on the same geometric mapping as in Algorithm 1, but without simulating the mechanical part of the fiber model. At the beginning of the simulation, predefined curvatures can be specified, from which the geometric model generates a set of nodes with six degrees of freedom. These nodes are then connected to form a surface mesh that serves as the structural support for the thin-shell model.

This procedure fully preserves the robot's preformed geometry while simplifying the numerical process. The fiber model, therefore, acts only as a geometric initializer, providing the spatial organization of the nodes before the shell-based mechanical computation begins (Figure 4.3).

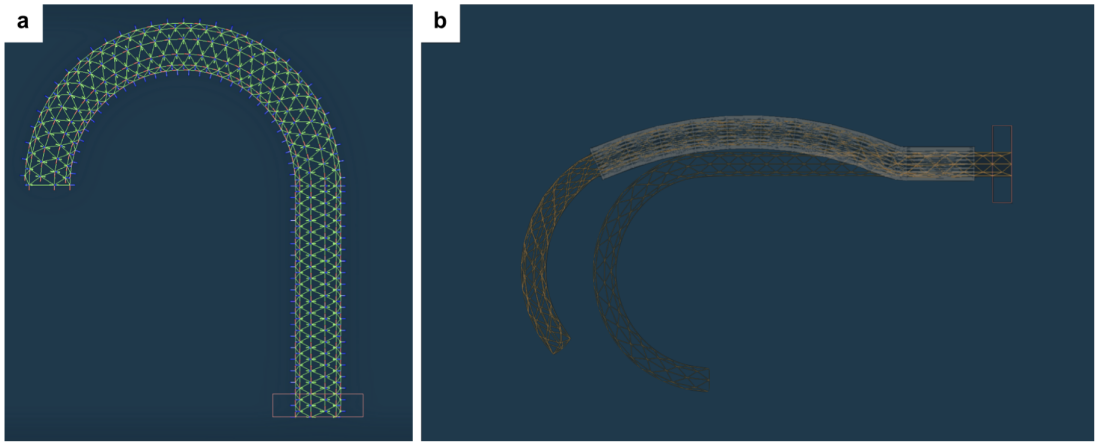


Figure 4.3: Numerical implementation of the fiber-based geometry in SOFA. (a) Initial configuration of the eversion-based robot generated from the fiber analogy, with a predefined distal curvature ensuring a controlled and stable mesh discretization. (b) Validation test performed in a constrained tubular environment to verify the proper functioning of the collision module and the preservation of the preformed geometry with pressurization.

[1]This implementation builds upon the DKT-Andes shell formulation originally developed by Olivier Comas in his PhD thesis and later extended by Tomáš Golembiovský for surgical simulation applications [114]. For readers interested in reproducing the implementation or exploring the simulation in greater detail, a comprehensive description of the SOFA hierarchical architecture and the algorithms developed in this work is provided in Appendices A and B.

4.2 Mesh topology and thin-shell modeling

4.2.1 Principle & Requirements

The hybrid model presented in Chapter 3 only provided a partial representation of the robot, which limited both mechanical realism and the ability to reproduce local deformations. To overcome this limitation, the membrane was reformulated using a thin-shell finite element description. This choice offers several advantages in the context of the eversion-based robot: it is naturally suited to thin-walled structures, it coherently integrates membrane and bending contributions, and it enables the capture of local mechanical phenomena such as instabilities or sharp curvature variations. Moreover, it establishes a direct link with the measured material properties (E, ν, h), and provides a surface-based representation that is better adapted to the contact-rich interactions with walls, where local deformations and stresses must be accurately reproduced.

The formulation assumes a homogeneous equivalent material across the membrane thickness. Multilayer or composite configurations involving spatially varying constitutive properties are therefore not explicitly represented in the present framework and would require a dedicated layered shell formulation.

This refinement is particularly important in the biomedical context, as it allows the consideration of local phenomena such as buckling or excessive bending. These behaviors correspond directly to the difficulties encountered experimentally during the crossing of stenoses (Section 2.5): a localized instability of the membrane can block deployment and prevent passage, which the previous hybrid model was unable to faithfully reproduce. By enabling the simulation of such scenarios, the thin-shell formulation strengthens the predictive value of the model for analyzing the robot's navigation in constrained anatomical environments.

A modification of the bending stiffness scaling was nevertheless required to prevent instabilities at very small thicknesses. Validated through a sensitivity analysis, this adjustment ensures a robust compromise between fidelity and numerical stability, which is essential for reliable simulations.

4.2.2 Modeling

Since the mesh is associated with a thin-shell model, its structure must produce equilateral triangles to guarantee numerical stability. Consequently, the configuration of fibers F_i described previously adopts an asymmetric arrangement: odd fibers F_{odd} are shifted along the X-axis (Equation 4.7), while even fibers F_{even} retain their initial position (Equation 4.8).

$$F_{\text{odd}} = \begin{cases} x = (L_{F_i}/S_{F_i})/2 \\ y = R \cdot \cos\left(\frac{2\pi F_i}{F}\right) \\ z = R \cdot \sin\left(\frac{2\pi F_i}{F}\right) \end{cases} \tag{4.7}$$

$$F_{\text{even}} = \begin{cases} x = 0 \\ y = R \cdot \cos\left(\frac{2\pi F_i}{F}\right) \\ z = R \cdot \sin\left(\frac{2\pi F_i}{F}\right) \end{cases} \tag{4.8}$$

The topology layout is applied to both straight and curved mesh configurations. However, in the case of a preformed curved configuration, an additional adjustment is required to preserve equilateral triangles in the curved region. The arc length L_{C_i} must be adjusted according to the edge length of the triangles L_T used to discretize the shell surface (Equation 4.9). By determining the number of triangles T that can be placed along this curvature (Equation 4.10), an adjusted length $L_{C_i'}$ is obtained (Equation 4.11). This ensures a uniform distribution of equilateral triangles across the entire mesh, including the curved region.

$$L_T = \frac{L_{F_i}}{S_{F_i}} \tag{4.9}$$

$$T = \frac{R_{C_i} \cdot \pi}{L_T} \tag{4.10}$$

$$L_{C_i'} = \frac{L_{C_i}}{T} \tag{4.11}$$

Once the mesh geometry is defined, it is crucial to model its mechanical properties in order to accurately represent its physical behavior [113]. To this end, a stiffness matrix $\mathbf{K}$ is defined (Equation 4.12).

$$\mathbf{K} = \frac{E}{1-\nu^2}\begin{bmatrix} 1 & \nu & 0 \\ \nu & 1 & 0 \\ 0 & 0 & \frac{1-\nu}{2} \end{bmatrix} \tag{4.12}$$

From this matrix, two specific matrices are derived to account for shell thickness: the membrane stiffness matrix $\mathbf{K}_{\text{mesh}}$ (Equation 4.13), which describes in-plane resistance, and the bending stiffness matrix $\mathbf{K}_{\text{bending}}$ (Equation 4.14), which models resistance to bending forces and moments.

Without delving into the details of shell element formulation, both matrices integrate Hooke's law $\mathbf{C}$; however, one scales linearly with thickness, while the other scales with the cube of the thickness.

$$\mathbf{K}_{\text{mesh}} \propto h \cdot \mathbf{C} \tag{4.13}$$

$$\mathbf{K}_{\text{bending}} \propto \frac{h^3}{12} \cdot \mathbf{C} \tag{4.14}$$

For meshes with very small thicknesses ($h \leq 100\,\mu\text{m}$), the contribution of bending becomes negligible compared to that of the membrane, which leads to an ill-conditioned system matrix and convergence difficulties during simulation. To prevent this instability, the cubic term is replaced by an adjusted thickness-dependent coefficient, $\mathbf{K}_{\text{bending}} \propto h^2 \cdot \mathbf{C}$, ensuring a minimal contribution of the bending term while preserving its mechanical structure.

This adjustment is primarily a numerical measure, but its physical impact remains nondeterminant: within the considered thickness range, bending contributes several orders of magnitude less than the membrane, and the global behavior remains governed by membrane strain energy, in line with thin-shell theory. A sensitivity analysis confirms that global displacements and contact forces remain invariant within standard tolerance ranges, thereby validating the chosen approximation. The full analysis is provided in Section 5.2.1, where it is discussed in detail.

It should nevertheless be noted that in certain specific situations, the contribution of bending could locally play a more significant role. This is particularly the case in the presence of highly localized instabilities, such as sharp buckling phenomena, or in contact regions where the load is concentrated over a very limited surface.

In such contexts, a dedicated sensitivity analysis would be required to refine the validity of the approximation. In the present study, however, which is focused on predicting global deployment and dominant contact forces in anatomically realistic scenarios, the chosen simplification remains fully consistent with the intended objectives.

4.2.3 Implementation in SOFA[2]

The FEM-based thin-shell model is implemented within a dedicated hierarchy to simulate the dynamics of the pressurized membrane during eversion. This structure relies on a set of coupled sub-blocks, ensuring both mechanical resolution and interaction management (Appendix B - Algorithm 3).

1. **Initialization:** The *Fibers* block, defined from the geometric framework presented in Algorithm 1, is integrated at the first level solely for initialization. It provides the geometric backbone required to link the continuous description to the shell representation.

2. **Solvers and constraint management:** The *Solvers* block gathers the components required for the numerical resolution of the mechanical problem. Time integration is performed by an `EulerImplicitSolver`, with a time step fixed at $\Delta t = 0.01\,\text{s}$, coupled with Rayleigh damping (`rayleigh Stiffness` $= 0.08$, `rayleighMass` $= 0.08$) to limit numerical oscillations and stabilize the dynamics, but also to reproduce the mechanical behavior of the material, which is not purely elastic but exhibits viscoelastic characteristics. Linear system resolution relies on a `SparseLDL Solver`, optimized for sparse matrices arising from finite element discretization. Finally, a `GenericConstraintCorrection` computes the compliance in the space defined by the Lagrangian constraints, ensuring consistent enforcement of these constraints throughout the simulation. The combination of

[2]This implementation builds upon the DKT-Andes shell formulation originally developed by Olivier Comas in his PhD thesis and later extended by Tomáš Golembiovský for surgical simulation applications [114]. For readers interested in reproducing the implementation or exploring the simulation in greater detail, a comprehensive description of the SOFA hierarchical architecture and the algorithms developed in this work is provided in Appendices A and B.

these components ensures robust and stable convergence, even under large deformation regimes.

3. **Definition of the shell mesh:** The *ShellMesh* block defines the surface discretization of the membrane. It contains a `Rigid3d MechanicalObject` (*shellMO*) that stores the nodal positions, a `MeshTopology` specifying the connectivity of the elements, and a `TriangleShellForceField` that computes the elastic response of the shell in both bending and stretching, using material parameters such as Young's modulus E, Poisson's ratio ν, and thickness h. Boundary conditions are imposed by a `FixedConstraint` applied to the first ring of nodes, corresponding to the robot base, to reproduce the anchoring of the membrane during pressurization.

4. **Coupling with pressurization:** A dedicated sub-block, *PressureMesh*, is associated with the shell to model the effect of internal pressure. It contains its own `MeshTopology` and a `Vec3d MechanicalObject` (*shellMOTransfo*) linked to the main shell configuration (*shellMO*) through an `IdentityMapping`. This mapping ensures that both meshes remain geometrically consistent throughout the simulation. A uniform `SurfacePressureConstraint` is then applied to *shellMOTransfo*, generating an internal pressure P that drives inflation and reproduces the mechanical effects of eversion.

5. **Collision handling:** The *PressureMesh* block also incorporates collision models at different levels of detail (`TriangleCollisionModel`, `LineCollisionModel`, and `PointCollisionModel`), allowing robust detection of contacts with the environment and stable interaction between the membrane and external obstacles.

4.3 Eversion modeling

4.3.1 Principle & Requirements

The modeling of the eversion-based robot raises several challenges, particularly in representing the eversion process, where the structure transitions from an internal storage state to an eversion zone before being deployed outward.

In Chapter 3, eversion could be simulated, but only at the cost of a very high computational load. This was because the mesh elements were attached to the geometric fibers, all of which had to be computed, including those located in the storage zone. This internal region, where the membrane folds onto itself, accumulates a large number of nodes and generates multiple contact points. A fully detailed simulation would require complex self-collision management, further increasing computational cost without significantly improving accuracy, since the influence of this zone on the global dynamics remains limited until the elements reach the eversion region.

In the present chapter, the fiber-based representation is no longer used in the simulation. However, to maintain the structural consistency of the internal nodes and to guide their motion during eversion, a numerical guide is introduced. This central structure manages the storage zone by constraining the elements with a network of springs, ensuring their stability without the need for expensive contact computations. This strategy simplifies the representation of the storage zone, focuses computational resources on the eversion zone, and does not compromise the accuracy of the global results.

By contrast, the eversion zone plays a crucial role, since it is in this region that the mesh elements progressively transition from the inside to the outside. Unlike the storage phase, a precise modeling of this step is essential to correctly capture the mechanical interactions. This requires the reactivation of collisions and self-collisions, while maintaining a smooth transition to avoid numerical instabilities that could compromise robustness.

To achieve a faithful representation of the eversion process, two complementary tools are implemented (Figure 4.4):

- A numerical guide, which centralizes and stabilizes the nodes in the storage zone using a network of springs;
- Dynamic storage and eversion zones, which define the conditions for the progressive release of springs, ensuring a smooth transition between the different phases of deployment.

The mechanism operates as follows: as long as the elements remain in the storage

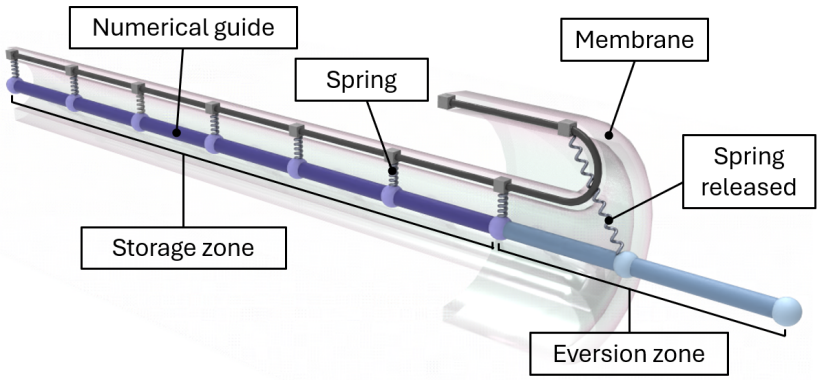


Figure 4.4: Numerical guide regulating the deployment of the membrane during eversion through dynamic zones. In the storage zone, the mesh is attached to the numerical guide by springs, ensuring its stability before deployment. As the mesh progresses, it enters the eversion zone, where the springs are released.

zone, they are constrained by the numerical guide. Once they reach the eversion zone, the springs are released, allowing the shell elements to detach, recover their natural mechanical behavior, and deploy outward. This controlled buffer mechanism stabilizes the eversion zone, reduces numerical artifacts, and enables a faithful representation of self-contacts and the forces exerted on the vascular environment.

This focus on the eversion zone is particularly relevant in our biomedical context, as it is precisely in this region that the robot interacts with vascular walls. Concentrating computational resources on this critical zone improves the ability to reproduce contact forces and local deformations that govern the robot's navigability and safety. This is essential not only for assessing its capacity to cross stenotic segments, but also for analyzing its behavior in tortuous pathways, or in regions with fragile walls where the risk of trauma must be minimized.

4.3.2 Modeling

The numerical guide G, composed of several sub-guides G_i, is designed to coordinate the motion of the mesh during eversion (Figure 4.5). Each sub-guide must be spatially aligned with its associated fiber F_i to preserve geometric consistency during eversion. To achieve this alignment, a rotation is applied to each sub-guide so that its orientation matches that of the corresponding mesh fiber.

The alignment process relies on quaternion algebra. Each sub-guide G_i and each fiber F_i are initially defined by their respective orientation quaternions, $\mathbf{q}_{G_i}$ and $\mathbf{q}_{F_i}$. The relative quaternion $\mathbf{q}_i$ represents the rotation required to align the orientation of the guide with that of the fiber (Equation 4.15).

$$\mathbf{q}_i = \mathbf{q}_{F_i} \cdot \mathbf{q}_{G_i}^{-1} \tag{4.15}$$

From this relative quaternion, the corresponding rotation matrix $\mathbf{R}_i$ is obtained using the operator $\mathcal{R}(\cdot)$, which converts a quaternion into its equivalent rotation matrix (Equation 4.16).

$$\mathbf{R}_i = \mathcal{R}(\mathbf{q}_i) \tag{4.16}$$

This rotation is applied to each sub-guide G_i to update its spatial orientation before coupling with the mesh nodes. This ensures that all guidelines share the same local orientation as their associated fibers, maintaining geometric continuity throughout the eversion process.

After this alignment step, each sub-guide is discretized into a set S of sections $S_{G_i,j}$, where $j \in [0, S-1]$, matching the discretization of the mesh $S_{F_i,j}$ to ensure consistent topological alignment between both structures. For each section, every mesh node $N_{F_i,j}$ is connected to its corresponding guide node $N_{G_i,j}$ by a spring element, where $j \in [0, S]$.

The stiffness $\mathbf{k}$ of these springs varies depending on their position along the system. In the storage zone, high-stiffness springs ($\mathbf{k}_{1e9}$) constrain the mesh elements to the guide, preventing premature motion. As they enter the eversion zone, the stiffness of the springs is gradually reduced until it reaches zero ($\mathbf{k}_0$), allowing the mesh to detach and deploy freely into the external environment.

The guide itself moves at a constant velocity v, while the eversion front progresses at a reduced velocity $v/2$, consistent with the effective kinematics of mesh deployment in everting robots. This velocity difference ensures a smooth and stable release of the mesh elements, in accordance with the mechanical constraints imposed by the system design.

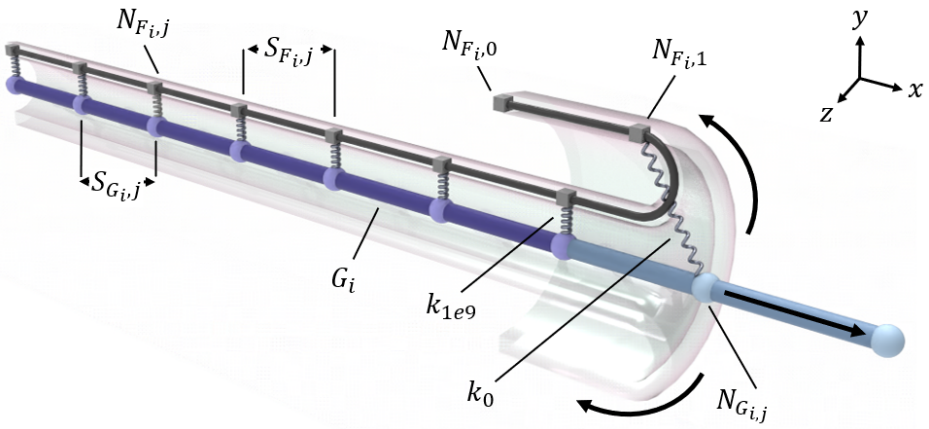


Figure 4.5: The numerical guide is composed of sub-guides G_i, each aligned with its corresponding mesh fiber F_i. The guide and the mesh are discretized into corresponding sections $S_{G_i,j}$ and $S_{F_i,j}$. Each node $N_{G_i,j}$ of the numerical guide is connected to its corresponding mesh node $N_{F_i,j}$ by springs whose stiffness varies according to their position: in the storage zone, high-stiffness springs ($\mathbf{k}_{1e9}$) prevent premature motion, while in the eversion zone, the stiffness progressively decreases to zero ($\mathbf{k}_0$) to enable controlled release of the elements.

4.3.3 Implementation in SOFA[3]

The *Shell* layer complements the geometric description by introducing a meshed envelope in which eversion is represented and controlled. Here, the structure integrates the guides, attachment points, and controller, ensuring that the shell evolves consistently with the previously defined internal geometry (Figures 4.6 and 4.7) (Appendix B - Algorithms 4 and 5).

1. **Initialization:** The *Fibers* block, inherited from the initial geometric hierarchy (Appendix B - Algorithm 1), is instantiated only to provide geometric initialization and ensure consistency of nodes coordinates.

2. **Eversion zones:** Two arrows (`ArrowObject`) are integrated in the *Shell* block to facilitate visual tracking of the eversion process. One represents the portion of the robot already deployed, while the other indicates the portion still stored, allowing real-time localization of the eversion zone.

[3]This implementation builds upon the DKT-Andes shell formulation originally developed by Olivier Comas in his PhD thesis and later extended by Tomáš Golembiovský for surgical simulation applications [114]. For readers interested in reproducing the implementation or exploring the simulation in greater detail, a comprehensive description of the SOFA hierarchical architecture and the algorithms developed in this work is provided in Appendices A and B.

3. **Shell mesh:** This block contains the discrete envelope of the structure (Appendix B - Algorithm 3). It is coupled to attachment points instantiated in a loop within the *Attachment* sub-block, where each element includes:

   - a `MechanicalObject` (*attachmentMO*);
   - a `RestShapeSpringsForceField` linking the attachment to the reference geometry from the sub-guides (from *attachmentMO* to *orientedSubGuideMO*);
   - a `SubsetMapping` transferring nodes from the global mesh to the attachment (from *shellMO* to *attachmentMO*). This operation allows targeting a subset of points for the local application of attachment springs while preserving topological consistency with the global mesh.

4. **Controller:** The `Controller` governs the global motion of the membrane by imposing the kinematic progression of the guides. It ensures synchronization between sub-guide displacement, shell mesh deformation, and eversion progression, thereby guaranteeing a consistent and controlled evolution of the model.

5. **Guide – even indices:** The *EvenGuide* block defines the guide structure associated with even indices. Its hierarchy is organized as follows:

   - a `Rigid3d MechanicalObject` (*baseGuideMO*) storing the guide's base coordinates;
   - a *GuideCoordinate* sub-block, containing its own `Vec3d Mechanical Object` (*coordinatesGuideMO*) and a `BeamHookeLawForceField` describing elastic behavior along the guide;
   - a *GuideFrame* sub-block, where local frames (*framesGuideMO*) are generated and linked through a `DiscreteGuideMapping`;
   - an internal *EvenSubGuide* block, which for each index instantiates:
     - a local base *EvenSubGuideBase* with its `Rigid3d MechanicalObject` (*baseSubGuideMO*);
     - a `SubGuideFrame` sub-node, in which local frames (*framesSubGuideMO*) are obtained by a `DiscreteSubGuideMapping` from *baseSubGuideMO*;

- a *OrientedSubGuide* sub-block including a `Rigid3d MechanicalObject` (*orientedSubGuideMO*) and a `RigidMapping`. The latter applies an initial quaternion-based transformation, computed between the non-everted state and the partially everted state, to realign the orientation of the sub-guides. This realignment ensures compatibility with the membrane and coherent connection for motion transfer and boundary condition enforcement;
- a *SubGuideCoordinate* block with a `Vec3d MechanicalObject` (*coordinatesSubGuideMO*) and a `BeamHookeLawForceField` describing elastic behavior along the sub-guide.

6. **Guide – odd indices:** The *OddGuide* block replicates the same structure as *EvenGuide*, but applied to odd indices, thereby ensuring symmetry of the guiding system across the entire shell.

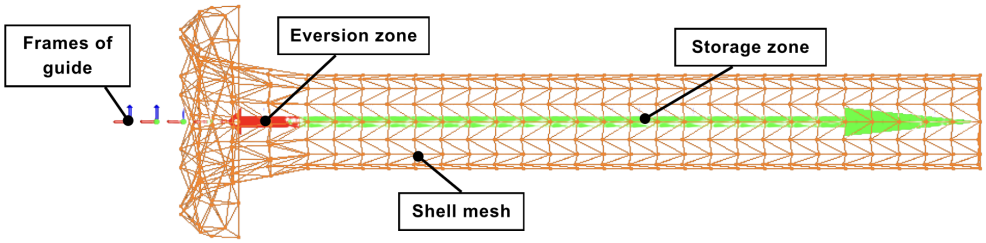


Figure 4.6: The numerical visualization shows the guide frames ensuring the robot's deployment, the shell mesh representing the robot membrane, and the two functional zones governing its motion: the storage and the eversion zone.

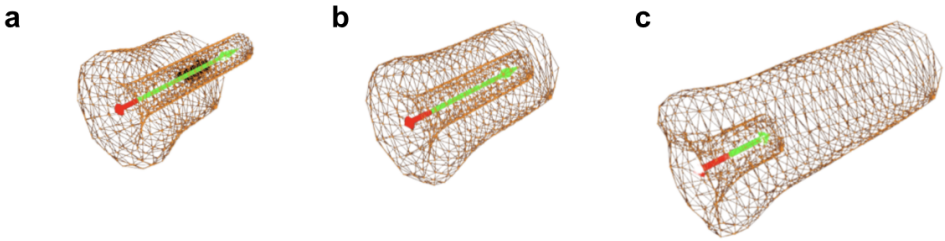


Figure 4.7: Progressive eversion process from (a) to (c), where the storage zone gradually diminishes as the robot deploys. The advancing shell illustrates controlled membrane growth and the stable progression of the eversion front in a free environment.

4.4 Conclusion

Building on the model developed in Chapter 3, this chapter introduced structural and geometric optimizations to overcome identified limitations and to provide a more faithful description of the behavior of the eversion-based robot.

First, the geometric generation of the initial mesh was refined using an analogy with geometric fibers. No longer employed as dynamic elements but rather as construction supports, these fibers enabled the reconstruction of the robot's tubular envelope with precise control of curvature and orientation. This method allows for the definition of either straight or preformed configurations, adapted to complex constraints such as those of the aortic arch, while ensuring mesh quality favorable to numerical stability.

Second, the mechanical representation of the membrane was reinforced through the adoption of a thin-shell finite element formulation. This approach, particularly well-suited to thin-walled structures, consistently integrates both membrane and bending contributions. It thus captures phenomena of buckling, curvature, and local deformation characteristic of pressurized membranes. To ensure numerical stability in the case of extremely small thicknesses, a discretization was implemented to generate nearly equilateral triangles, thereby improving system conditioning. Furthermore, an adjusted scaling coefficient was introduced in the bending stiffness matrix, ensuring sufficient numerical weighting of this term without altering the physical dominance of membrane energy.

Finally, the modeling of eversion dynamics was substantially enriched by introducing a numerical guide and dynamic storage and release zones. This mechanism, based on a network of springs with spatially varying stiffness, ensures a progressive and stable transition of the robot's elements from the folded state to the deployed configuration. By reproducing the specific kinematics of eversion, this approach stabilizes the deployment process, limits numerical instabilities, and improves the management of self-collisions.

The proposed implementation brings together three complementary components: the geometric construction based on fibers and sub-guides, the mechanical modeling of the thin-shell membrane, and the kinematic control ensuring a stable eversion process. By combining these elements, the objective was to overcome

the limitations observed in previous models, which either prioritized computational efficiency over physical realism or achieved high mechanical accuracy at the cost of numerical instability. The present model establishes a new balance between local geometric accuracy, realistic mechanical behavior of the membrane, and stable control of the eversion kinematics.

The resulting model therefore represents a step forward, capable of realistically reproducing the mechanical behavior and kinematic evolution of the eversion-based robot in varied contexts and under realistic anatomical constraints (Figure 4.8). Beyond the technical refinements, this simulation architecture itself constitutes a methodological contribution: by combining controlled geometric initialization, a stabilized thin-shell formulation, and a kinematic guide for eversion, it opens the way to a more robust and faithful analysis of eversion-based robots, compared to existing approaches that either prioritize speed over fidelity, or accuracy at prohibitive computational cost.

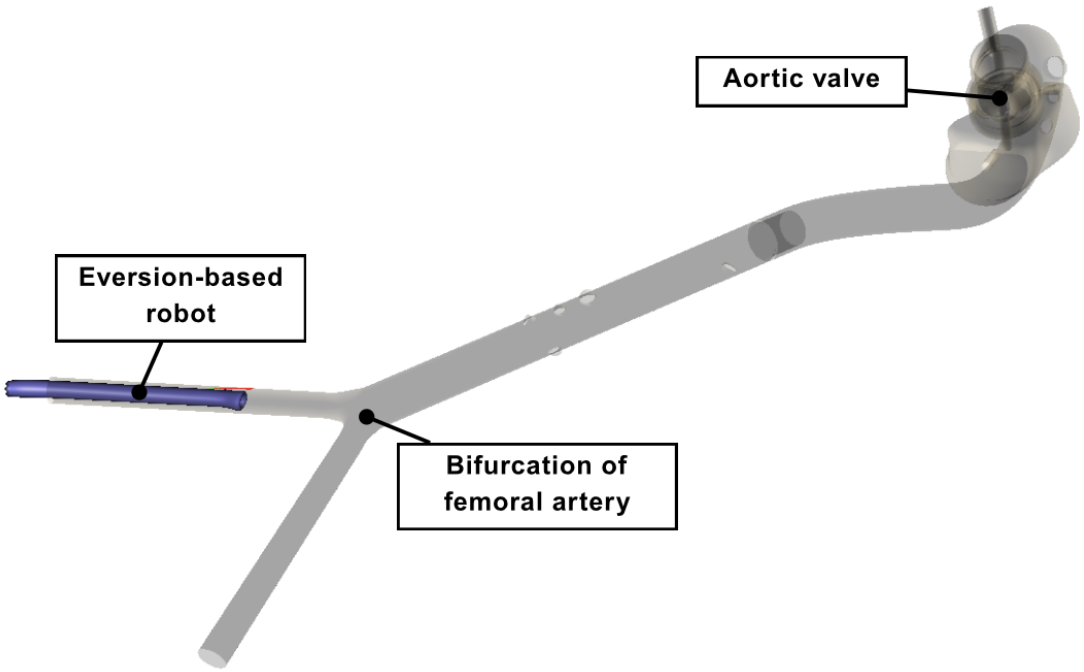


Figure 4.8: Preliminary SOFA simulation of an eversion-based robot's deployment within the Pangolin phantom, a vascular model replicating the anatomical pathway from the femoral artery to the aortic valve.

Nevertheless, challenges remain when targeting large-scale and anatomically realistic scenarios. In such cases, the computational cost associated with collision

handling increases markedly, due to the accumulation of self-contacts along the robot and continuous interactions with the phantom walls. This limitation does not contradict the improvements achieved in this chapter: rather, it reflects the intrinsic complexity of reproducing highly realistic deployments. Optimizing collision management, therefore, emerges as a critical step toward extending the applicability of the simulation to long trajectories and preclinical validation.

To address these constraints, two strategies seem particularly suitable. The first consists of explicit collision filtering, which restricts robot/guide calculations to regions where precise contact is required, namely at the eversion zone. The second relies on the use of multi-resolution collision models: the already deployed sections, relatively stable and far from the eversion zone, can be represented by simplified geometries, while the active zone retains a detailed mesh to accurately describe local interactions.

Chapter 5

Design, control and experimental validation

Experimental validation establishes the link between the hybrid numerical model and its clinical application. Building on the fiber-based FEM framework and the refined mechanical description introduced in the previous chapters, this chapter compares numerical predictions with physical experiments. The goal is to verify the model's predictive accuracy, determine the most suitable material and design parameters for safe deployment, and confirm the robot's relevance within the TAVI procedure.

The comparison between numerical predictions and physical experiments requires clarification of the level of correspondence between the modeling framework developed and the robot that was actually fabricated. The geometry implemented in the simulation reproduces the overall dimensions of the device, its membrane thickness, and its configuration. The mechanical parameters used in the model are derived from measurements performed on the materials employed in fabrication, ensuring consistency between the numerical description and the behavior observed within the pressure range under consideration. The pressurization conditions adopted in the model correspond to the stable eversion pressure identified experimentally. In specific configurations, particularly during traversal of stenotic environments, the simulation maintains this stable eversion pressure without attempting to reproduce pressure variations that may occur in real conditions, as

the objective is to represent the dominant mechanical trends governing deployment stability.

The eversion zone is described in a manner consistent with the physical phenomenon observed. Its spatial extent is selected to enable a continuous representation of membrane turning while ensuring numerical stability. The model is therefore intended to reproduce the global deformation patterns and the principal mechanical evolutions associated with pressurized deployment, rather than to resolve local stress concentrations or strongly nonlinear material effects. The simplifications adopted, including the use of a linearized constitutive behavior within the operating pressure range, the omission of viscoelastic effects, and an idealized treatment of contact interactions, are consistent with the purpose of the model, which is to provide a predictive tool for structural optimization and safety assessment.

Regarding interaction with the surrounding environment, contact is modeled through a mechanically consistent formulation allowing the membrane to adapt to constrained geometries and redistribute stresses under narrowing conditions. This approach captures the global diameter reduction and the associated increase in contact forces observed during stenotic traversal. However, the surrounding medium is represented in an idealized manner, without incorporating detailed vascular anisotropy, complex frictional behavior, or fluid–structure coupling. Within the intended scope of the model, this level of description is sufficient to reproduce the dominant mechanical interaction patterns while maintaining computational tractability.

5.1 Experimental System

To compare the results obtained from numerical simulations with those from physical tests, it was first necessary to design and implement an experimental platform capable of providing stable actuation conditions, precise pressurization, and reproducible measurements. This section first presents the architecture of the setup before introducing the materials selected for their contrasting mechanical behaviors and their potential to ensure atraumatic navigation within the endovascular environment. These materials serve as the basis for prototype fabrication,

which in turn forms the foundation for the comparison between numerical and experimental data, ensuring a coherent and rigorous analysis of the robot's behavior.

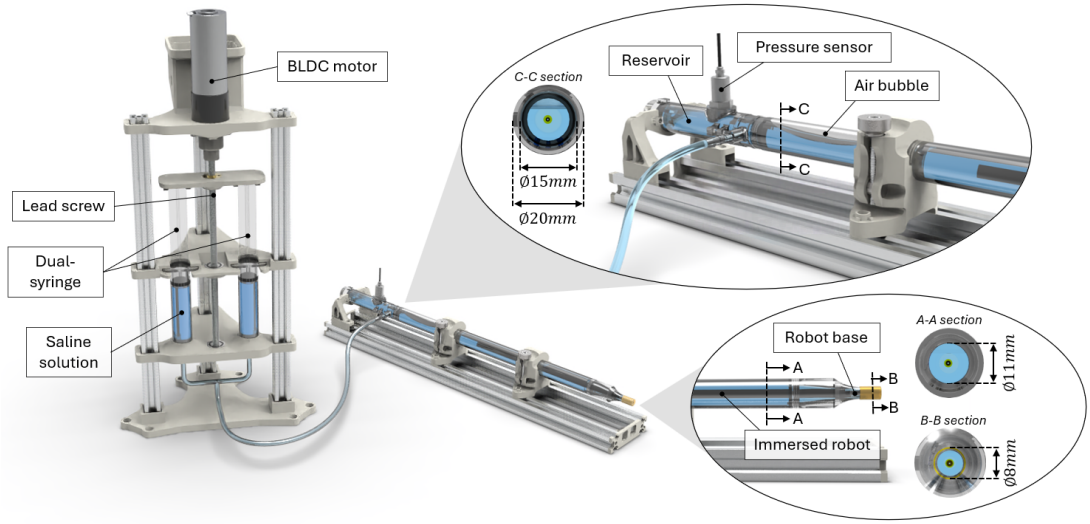


Figure 5.1: The experimental setup includes a dual-syringe pump driven by a brushless DC (BLDC) motor and a lead screw mechanism to inject physiological saline solution into the reservoir. The pressure sensor is mounted on the first tube, which also serves as the fluid injection point. A widened 15mm (C-C section) diameter segment creates a passive air chamber that stabilizes internal pressure by damping fluctuations. The tubing then returns to 11 mm (A-A section) before narrowing to 8 mm at the robot base (B-B section), where the robot is immersed. Air bubbles are trapped at the interface between the 15 mm and 11 mm sections, contributing to pressure regulation during deployment.

5.1.1 Experimental Actuation System

The experimental actuation system (Figure 5.1) forms the core of the robot's operation and control by ensuring precise pressurization regulation and stable deployment control. To fulfill these essential functions, the system is designed around two complementary modules: (1) a pressurized reservoir and (2) a pressurization system.

(1) The pressurized reservoir plays a critical role in maintaining the robot's structural integrity and mechanical stability during deployment. Two key aspects must be considered: the internal environment and the physical design of the system.

First, the robot is immersed in a 0.9% NaCl physiological saline solution within the reservoir. This solution provides several crucial advantages for optimal deployment:

- Reproduces the conditions encountered in the human vascular environment, thereby reducing the risk of gas embolism in the event of accidental leakage;
- Ensures chemical compatibility with soft polymers, preserving their mechanical properties;
- Provides natural lubrication, minimizing internal friction, allowing smooth and uniform robot eversion.

Additional tests were conducted using a water-based lubricant (*Gel Lubricant water-based*, Astroglide) in place of saline, owing to its higher viscosity, which was expected to reduce internal friction and potentially lower the eversion threshold pressure. The lubricant was tested both in its pure form and diluted 1:1 with water to assess the influence of concentration. In both configurations, the fluid was injected following the same pressurization protocol as the saline solution. The recorded pressure profiles and visual observations revealed no improvement over saline solution: eversion pressure and unfolding behavior remained identical. As no improvement was observed, either in terms of hydrodynamic friction reduction or decreased eversion pressure threshold, this option was not retained for subsequent experiments.

Finally, the physical design of the reservoir introduces a heterogeneous pressurized environment in which air bubbles play a stabilizing role during deployment. Instead of being completely filled with liquid, the configuration intentionally includes a chamber where air can be trapped to act as a compressible damping medium. This is achieved through the assembly of a series of resin tubes (*Clear Resin*, Formlabs), each 150 mm long and 20 mm in outer diameter. The first segment, which serves as the interface for pressure monitoring and fluid injection, has an inner diameter of 11 mm. It is followed by an expanded segment with an inner diameter of 15 mm. During filling, the change in diameter causes air bubbles to rise and accumulate in this region, forming a passive air chamber whose empirically adjusted volume helps stabilize the internal pressure during eversion. This discontinuity forms a passive air chamber that cushions pressure and volume

fluctuations during fluid injection. Downstream, the tube returns to an 11 mm inner diameter, trapping the air volume within the reservoir. The final segment, to which the robot is attached, gradually tapers from an inner diameter of 11 mm to 8 mm. This final narrowing acts as a geometric barrier, minimizing the risk of air bubble migration into the robot chamber and thus maintaining actuation stability.

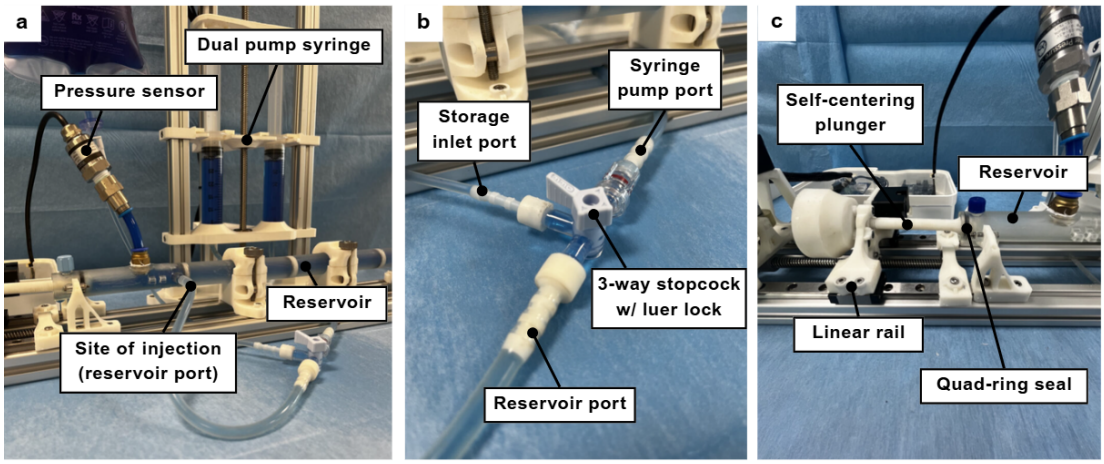


Figure 5.2: (a) Global view of the setup, comprising the pressure sensor mounted on the reservoir inlet tube, the dual-syringe pump, the pressurized reservoir filled with saline solution, and the main injection site (reservoir port). (b) Detailed view of the reservoir port equipped with a three-way Luer lock stopcock, enabling three distinct connections: the storage inlet port for filling with saline solution, the syringe pump port for controlled injection, and the reservoir filling port ensuring hydraulic continuity during experiments. (c) A dynamic actuation module designed to generate sinusoidal pressure profiles, consisting of a self-centering plunger equipped with quad-ring seal, sliding along a linear rail within the reservoir to minimize friction.

(2) To monitor the deployment process and analyze the robot's mechanical response, a pressure sensor (*SEN0257*, DFRobot) was installed on the first tube of the reservoir, which also serves as the main injection site (Figure 5.2). The assembly includes a three-way luer lock valve that enables: (i) filling of the pressurized reservoir from a saline storage tank, (ii) filling of the syringe pump, and (iii) progressive injection of fluid from the syringe pump into the reservoir. This injection of 0.9% NaCl solution pressurizes the reservoir and thereby ensures controlled robot eversion. It is performed using a dual-syringe pump (2×30 ml) driven by a lead screw coupled to a brushless DC motor (*EC-max 40*, Maxon Motor). This setup guarantees a stable and continuous saline flow during eversion.

Under standard operation, the motor speed is adjusted to maintain a constant pressurization profile and enable real-time monitoring of the robot's mechanical response. The different pressure quantities monitored within the actuation system and used for subsequent analyses are summarized in Table 5.1, serving as reference definitions for the experimental results presented later in this chapter.

This continuous mode was occasionally complemented by a pulsatile modulation to investigate the robot's response under dynamic pressurization conditions (Figure 5.2). The pressure pulses, sinusoidal in shape and ranging from 2.5 to 10 Hz, were generated by a self-centered two-part plunger printed in resin (*White*, Formlabs) and equipped with a quadrilobe Ethylene Propylene Monomer seal. This type of seal reduces friction by approximately 50% compared to a conventional O-ring configuration, thereby improving motion regularity. The piston moves along a linear rail at a maximum speed of 3–5 m/s, ensuring dynamic operation without mechanical play within the reservoir.

In addition, a solenoid valve (*USS2-00051*, US Solid) was tested as an alternative to the syringe-pump system, allowing direct fluid injection through rapid opening and closing of the flow. Various pressurization profiles (square, triangular, sinusoidal) were applied by modulating the frequency and duty cycle to evaluate the effects of dynamic pressurization on the robot's progression. Although the solenoid valve enabled comparable pressure amplitudes to those achieved with the syringe pump, the system proved unstable in practice: circuit purging was difficult, and recurrent uncontrolled air bubbles appeared, disrupting pressure regulation. Unlike the single, intentionally introduced air bubble in the main reservoir—which acts as a damping element—these parasitic microbubbles induced undesirable variability and hindered reproducibility. For these reasons, the solenoid valve approach was not retained for subsequent experiments.

Symbol	**Name**
P_i	Initiation pressure
P_e	Stable eversion pressure
P_r	Rupture pressure
P_c	Crossing pressure
P_d	Deformation threshold

Table 5.1: Characteristic pressures used for the robot experiments.

5.1.2 Material Range

To study the influence of material properties on the eversion process and deployment stability, several candidate materials were considered for the fabrication of the robot. Their selection followed a comparative rationale aimed at covering a representative range of mechanical behaviors, within the framework of homogeneous membrane materials as assumed in the model. The objective was to target contrasting regimes of compliance and stiffness in order to evaluate their influence on eversion stability and the ability to navigate through constrained geometries. Four materials were therefore selected: TPU (*HTM-1001 Polyether Polyurethane*, American PolyFilm), representative of semi-extensible polymers, characterized by high axial deformability; LDPE (*LFT8120STK*, Polybags), illustrating a stiffer and less extensible response; Polytetrafluoroethylene (PTFE) (*StreamLiner*, Zeus), much more rigid, representing an extreme case with virtually no axial deformation; and a woven textile (*Ripstop Nylon 6.6*, Extremtextil), already used in previous studies (Section 2.15), which exhibits an overall stiff behavior with some residual radial extensibility.

A mechanical characterization campaign was carried out to determine the pressurization thresholds associated with each tested material. The first threshold corresponds to the initiation pressure P_i, defined as the minimum pressure required to trigger membrane detachment and initiate the eversion process. The second is the stable eversion pressure P_e, i.e., the average pressure that must be maintained to ensure continuous robot progression once eversion has started. Finally, the rupture pressure P_r defines the threshold beyond which the membrane fails, while the ratio P_e/P_r quantifies the safety margin relative to the steady eversion phase.

The material selection was guided by a set of criteria designed to ensure the relevance of the evaluation. The initiation pressure (P_i) had to remain moderate, reflecting the material's ability to initiate eversion without excessive mechanical stress. The stable eversion pressure (P_e) needed to be as low as possible, as it directly determines the load transmitted to the vascular wall and represents a key factor in minimizing traumatic risk. Excessive eversion pressure leads to increased wall contact forces, which may in turn elevate the risk of vascular injury. The safety margin against rupture was quantified by the ratio P_e/P_r, with a low

value indicating that the operating pressure remains well below the material's mechanical limit. Airtightness was also a critical criterion to ensure deployment safety and exclude any leakage of fluid into the vascular environment. Finally, a well-defined contrast in mechanical stiffness between the soft and rigid materials was required to support model validation and allow for a meaningful comparison of deployment strategies.

The results (Table 5.2) highlight variations in the behavior of the tested materials. The TPU exhibits a very low initiation pressure ($P_i = 3$ kPa) and a moderate stable eversion pressure ($P_e = 18$ kPa). Its apparent rupture pressure ($P_r = 60$ kPa) reflects the semi-extensible nature of the material: it withstands significant deformation before failure, so that actual rupture only occurs after severe membrane swelling. The LDPE is characterized by a slightly higher initiation pressure ($P_i = 5$ kPa) and a higher stable eversion pressure ($P_e = 39$ kPa). The PTFE represents an extreme case, with a very high initiation pressure ($P_i = 100$ kPa) and an eversion pressure of the same order ($P_e = 150$ kPa). Finally, the woven textile shows intermediate values, lying between those of TPU and LDPE ($P_i = 7$ kPa, $P_e = 26$ kPa, $P_r = 80$ kPa).

Material	E **[MPa]**	P_i **[kPa]**†	P_e **[kPa]**†	P_r **[kPa]**†	P_e/P_r
TPU	10–100	3	18	60††	0.30
LDPE	200–400	5	39	100	0.39
PTFE	0.5–1.0	100	150	300	0.5
Fabric	1–6	7	26	80	0.32

† *: Average value based on 10 tests*
†† *: Rupture threshold reached after severe deformation*

Table 5.2: Characteristic pressurization thresholds in an unconstrained environment for the different membrane materials: initiation pressure P_i, stable eversion pressure P_e, rupture pressure P_r, and corresponding safety margin P_e/P_r.

The comparative analysis leads to the exclusion of certain materials for safety and experimental relevance reasons. The PTFE, whose initiation and maintenance pressures reach 100 kPa and 150 kPa respectively, requires mechanical stresses far exceeding those of the other samples. These levels, well above the more moderate pressures measured for TPU, LDPE, and the woven textile, appear unsuitable for the goal of atraumatic navigation. The woven textile, despite its intermediate values, was also excluded due to its intrinsic porosity, which induces the formation

of microbubbles on its surface during eversion—an indication of poor sealing incompatible with safe application under realistic conditions. Conversely, TPU and LDPE were selected to cover a moderate pressure range and to provide a mechanical contrast for validation. While TPU combines manageable operating pressure with safety against rupture, LDPE was included as a stiffer reference material to assess the influence of reduced compliance on deployment. They were therefore retained for subsequent experiments, the former representing a soft, semi-extensible behavior and the latter a stiffer, less deformable response.

Manufacturing Process of the TPU Robot

The fabrication process of the TPU robot consists of three main steps: (1) modeling and laser cutting of the substrate, (2) thermoforming of the TPU layers, and (3) final cutting and substrate removal. The equipment used includes a textile substrate (*Ripstop Nylon 6.6 tent fabric*, Extremtextil), a heat press (*Power Heat Press*, VEVOR), and a laser cutter (*Pro Laser*, Glowforge).

(1) The preforming process begins with a 3D CAD model of a substrate representing the robot's geometry, followed by laser cutting (power 11.25 W and speed 14.17 mm/s) (Figure 5.3). In the context of an endovascular procedure, the robot's dimensions are based on average anatomical characteristics of human vascular pathways. To ensure smooth navigation within vessels of approximately 8 mm in diameter, a width l of 9.42 mm corresponding to an internal diameter D of 6 mm ($l = (\pi \cdot D)/2$) was selected for the robot structure.

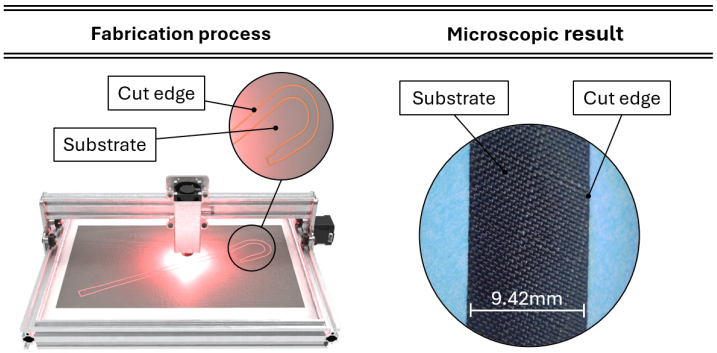


Figure 5.3: The robot's geometry is first defined and transferred to a laser cutting device to shape the substrate. To achieve the desired internal diameter of 6 mm, the substrate is cut with a width of 9.42 mm between the cut edges.

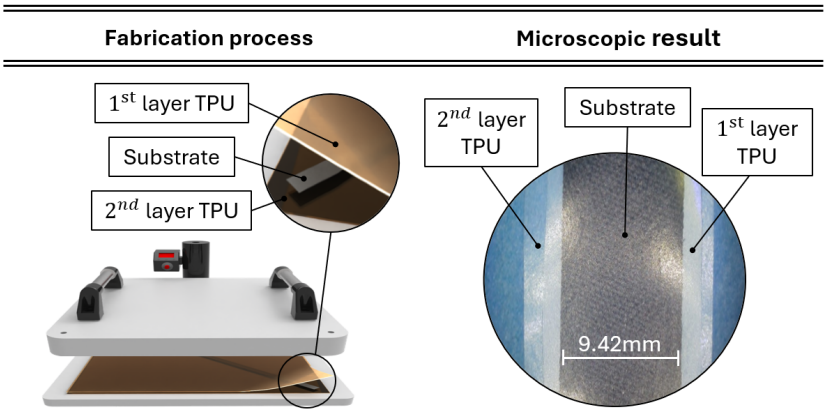


Figure 5.4: Thermo-compression is performed between a first and a second TPU layer, with the substrate placed in between to define the robot's shape and limit heat diffusion during the process.

(2) Various TPU films were evaluated to identify the material most suitable for robot fabrication. The selection criteria primarily concerned thermoformability, interlayer adhesion, mechanical strength under pressurization, and the flexibility required for the eversion mechanism. Four thicknesses h were tested: 25.4 μm (*MT-2001 Polyether Polyurethane*, American PolyFilm), 50.8 μm (*MT-1001 Polyether Polyurethane Natural*, American PolyFilm), 76.2 μm (*HTM-1001 Polyether Polyurethane*, American PolyFilm), and 127 μm (*HTM-850 Polyether Polyurethane*, American PolyFilm). The thinner films (h = 25–50 μm) proved fragile after thermoforming, exhibiting surface deformations such as wrinkles and irregularities likely to compromise structural uniformity. Conversely, the thicker films ($h \geq 127$ μm) showed satisfactory mechanical strength but excessive rigidity, which limited the flexibility required for smooth eversion.

The tests showed that the intermediate film with a thickness of h = 76.2 μm (*HTM-1001 Polyether Polyurethane*, American PolyFilm) offered the best compromise and was therefore selected for subsequent fabrication steps. Based on this choice, the thermo-compression process was established (Figure 5.4): the substrate is placed between two TPU layers to limit heat diffusion, and pressing is performed for 5 seconds at 105 °C. This temperature, lower than the melting range of TPU (154–171 °C), preserves its structural integrity while ensuring sufficient adhesion, as confirmed by a peel test yielding a maximum force of 30 N (*Force Gauge FK100*, Sauter).

(3) After cooling to room temperature (≈ 21 °C), the TPU structure is laser-cut (power 9 W, speed 72.26 mm/s) along an outer contour offset relative to the substrate edges. Experimental results (Table 5.3) for a robot with a diameter of 6 mm and a length of 50 mm show that a 1 mm offset is insufficient (50% rupture rate), while a 3 mm offset promotes the formation of air pockets due to TPU folding, leading to early deformations. A 2 mm offset represents the optimal compromise, reducing the rupture rate to 33.3%.

Fused TPU offset [mm]	**Minimum critical pressure [kPa]†**	**Maximum critical pressure [kPa]†**	**Rupture rate [%]†**	**Deformation rate [%]†**
1	10.1	30.6	50	66.66
2	27.1	37.9	33.33	100
3	24.7	28.8	16.66	100

† : *Average value based on 6 tests*

Table 5.3: Influence of the fused TPU cutting offset on the mechanical integrity of a robot. Critical pressures define the failure range, and rupture and deformation rates quantify the percentage of affected samples.

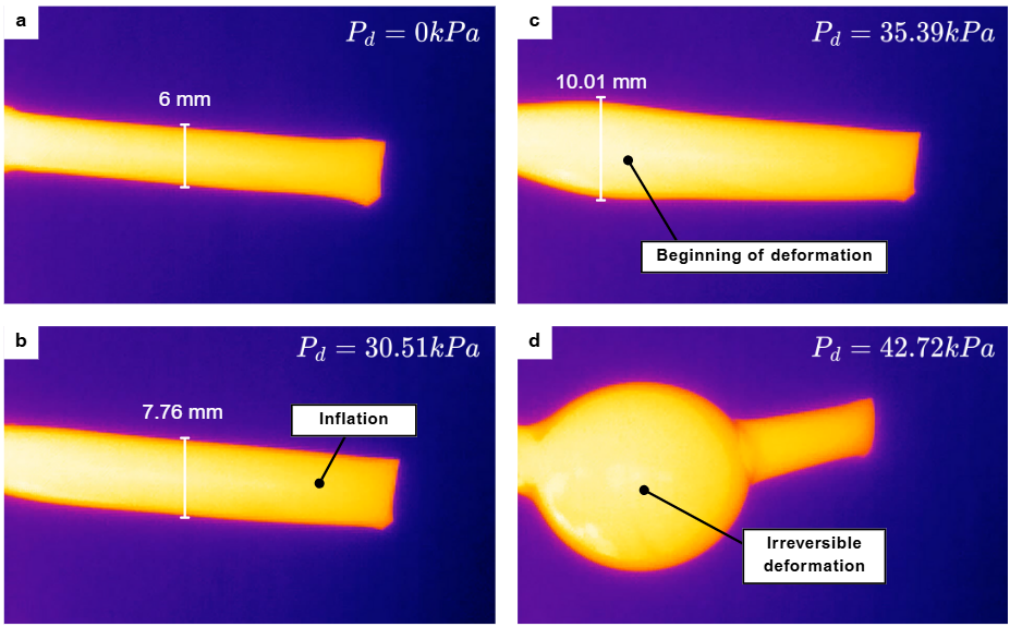


Figure 5.5: Evolution of the mechanical behavior of a TPU sample during pressurization: (a) initial state after complete eversion (⌀ = 6 mm), (b) uniform swelling phase (⌀ = 7.76 mm), (c) appearance of a localized deformation zone (⌀ = 10.01 mm), and (d) severe deformation phase, marking the onset of an irreversible regime that may lead to rupture.

Furthermore, the analysis of these tests highlights a characteristic deformation pattern for TPU (Figure 5.5). The tube first exhibits uniform swelling, increasing its initial diameter by up to approximately 1.5 mm. Beyond this regular deployment, a localized deformation zone appears at a characteristic pressure $P_d \approx 35$ kPa, reflecting the semi-extensible response of the material. Finally, as the loading continues, the structure enters a phase of severe and irreversible deformation, which in some cases evolves toward rupture, generally observed beyond 60 kPa. Once the cutting process is completed, the substrate is manually removed, and the TPU structure retains the imposed geometry corresponding to the final shape of the robot (Figure 5.6).

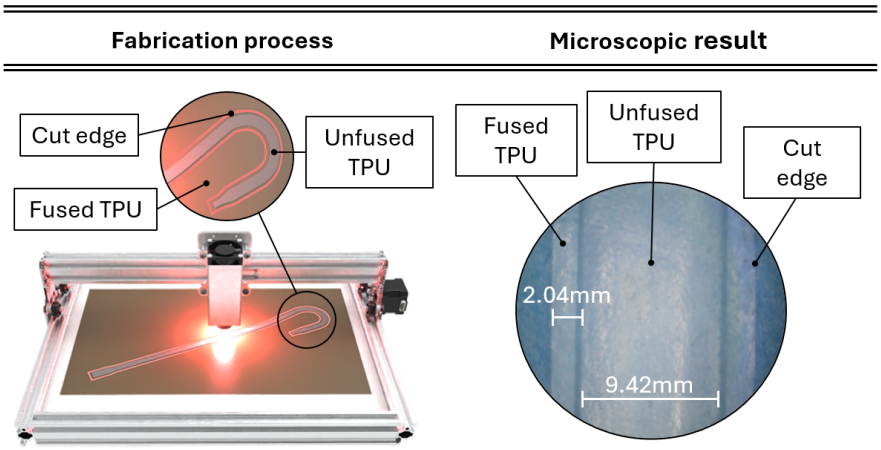


Figure 5.6: After thermocompression, the robot shape is defined by the unfused TPU area. To ensure optimal sealing, the surrounding fused TPU is cut with an offset of approximately 2.04mm.

Manufacturing Process of the LDPE Robot

The fabrication process of the LDPE robot, based on the literature [40, 115], consists of two main steps: (1) welding of the LDPE layers and (2) trimming of the robot edges. The materials and equipment used include two LDPE (*LFT8120STK*, Polybag) films of 30.5 μm thickness and a thermal sealer (*F-300*, Nestling).

(1) The robot structure is formed by applying a sealing time of 1.5 s to create two parallel welds along the plastic film. These welds define the sealed zone, leaving between them a width l corresponding to the robot's diameter. To ensure

consistency with the dimensions described in Section 5.1.2, l was set to 9.42 mm, corresponding to a robot diameter of 6 mm.

(2) The thermal sealer is equipped with a 3 mm-wide heating element, which by default defines a 3 mm offset for the robot. However, to maintain consistency with the 2 mm offset used for the TPU structure, the sealed zone is manually trimmed to 2 mm. This adjustment preserves the sealing quality while maintaining the mechanical performance of the structure, with the rupture pressure remaining around 87.99 kPa.

5.2 Experimental Evaluations

5.2.1 Material Inflation

To validate the accuracy of the numerical model described in Chapter 4, an initial experimental evaluation was conducted to compare simulated predictions with the actual mechanical response of the membrane during inflation. This series of tests focused on free tubular inflation to isolate the intrinsic behavior of TPU and LDPE in the absence of environmental constraints. The objective was to assess the model's ability to predict diameter variations as a function of internal pressure for materials exhibiting distinct mechanical properties (Table 5.4).

Material	L **[mm]**	$\varnothing$ **[mm]**	h **[μm]**	E **[MPa]**	ν
TPU	50	6	76.2	5	0.45
LDPE	50	6	30.5	200	0.45

Table 5.4: TPU and LDPE tubular sample properties.

The tested samples had a length of $L = 50$ mm, chosen as an average sampling dimension, and an initial diameter $\varnothing = 6$ mm corresponding to the configuration envisioned for navigation. The wall thickness h was 76.2 μm for TPU and 30.5 μm for LDPE. From a mechanical standpoint, TPU exhibits a Young's modulus of $E \approx 5$ MPa, characteristic of a semi-extensible behavior, while LDPE reaches $E \approx 200$ MPa, indicative of limited axial deformation. In both cases, the Poisson's ratio was set to $\nu = 0.45$.

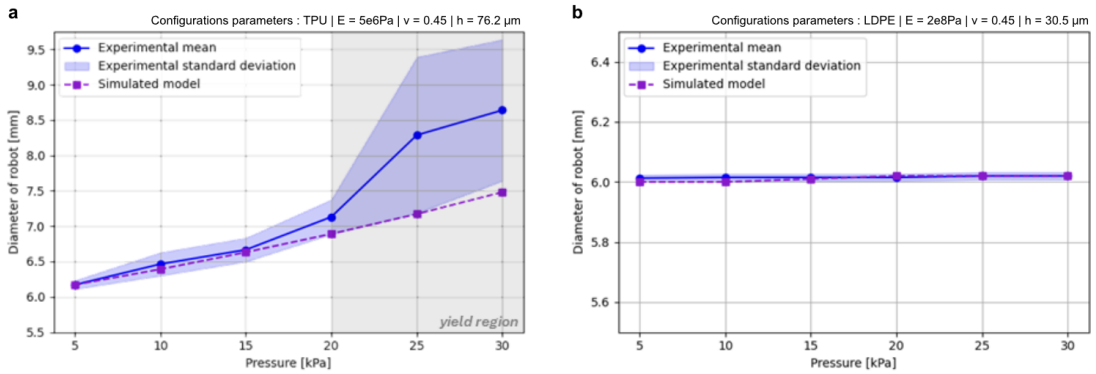


Figure 5.7: Correlation between simulated and experimental results for the inflation of TPU (a) and LDPE (b) meshes under applied pressure. The mean deviation between simulation results and experimental data is 0.46 mm for TPU and 0.01 mm for LDPE, with consistent deviations in both cases.

The results (Figure 5.7) show a correlation between simulations and experimental measurements, indicating that the model accurately reproduces the relative behavior of TPU and LDPE. For TPU, the simulation correctly captures the evolution of the diameter as a function of applied pressure, with a mean deviation of 0.46 mm. This deviation remains relatively stable under moderate deformations, reinforcing the robustness of the thin-shell model under typical operating conditions. However, at higher pressures, experimental variability increases significantly, and the model's ability to predict average behavior diminishes. This suggests that beyond a certain deformation threshold, the assumptions underlying Hooke's linear law and the classical thin-shell formulation are no longer valid, and that more advanced constitutive models or geometric nonlinearities would be required to improve predictive accuracy.

This trend, however, was not observed for LDPE, whose stiffer behavior limits the magnitude of deformations. In this case, the simulation remains in close agreement with the experimental data across the entire tested pressure range, with a mean deviation of 0.01 mm, indicating a particularly accurate representation of its mechanical response.

Although these results support the validity of the model, they rely on a formulation in which the bending stiffness term was intentionally modified to improve numerical stability. This adjustment was necessary because the FEM model describes the state of each node by six degrees of freedom—three translations and

three rotations—whose equilibrium configuration minimizes the total deformation energy of the shell. When the bending energy becomes several orders of magnitude smaller than the membrane energy, certain rotational degrees of freedom are poorly conditioned, and the solver can no longer converge accurately. Increasing the bending contribution slightly, therefore, improves numerical stability without affecting the physical relevance of the results. As detailed in Section 4.2.2, the classical cubic term was replaced with an adjusted coefficient $\alpha \propto h^2$ to maintain a minimal bending contribution for very thin meshes. To ensure that this adjustment did not alter the predicted mechanical behavior, a sensitivity analysis was conducted by varying the value of α over one order of magnitude around its nominal value.

The analysis focused on the impact of these variations on the global displacement d_{global} as well as its directional components d_x, d_y, and d_z. As shown in Table 5.5, all displacement metrics remain nearly constant despite variations in the bending energy amplitude, confirming that the system's behavior is primarily governed by membrane deformation energy. Specifically, the relative variation of d_{global} remains below 0.003%, and the directional components show similarly minimal deviations. Slight fluctuations are observed in d_y and d_z, but they remain negligible at the scale of the overall deformation.

α	$\mathbf{d_{global}}$ [cm]	$\Delta\mathbf{d_{global}}$ [%]	$\Delta\mathbf{d_x}$ [%]	$\Delta\mathbf{d_y}$ [%]	$\Delta\mathbf{d_z}$ [%]
3.9e-5	2.61680	0.00283	0.00353	-0.01092	-0.01091
4.4e-5	2.61676	0.00124	0.00157	-0.00527	-0.00545
4.9e-5	2.61672	0.0	0.0	0.0	0.0
5.4e-5	2.61670	-0.00088	-0.00118	0.00489	0.00500
5.9e-5	2.61667	-0.00214	-0.00274	0.00979	0.00954

Table 5.5: Sensitivity analysis of the adjusted bending coefficient α on the predicted displacements.

These results confirm that the bending term, adjusted for numerical stability, has a negligible influence on the mechanical response predicted by the model. The system's behavior is therefore governed almost entirely by membrane deformation energy, in accordance with thin-shell theory. The numerical modification introduced here specifically addresses a conditioning issue inherent to the FEM

formulation: since each node is defined by six degrees of freedom (three translations and three rotations), the bending energy is required to guide the rotational components of motion. When its magnitude becomes too small compared to the membrane energy, the solver cannot accurately resolve these directions, leading to numerical instabilities. The adjusted coefficient $\alpha \propto h^2$ ensures sufficient bending contribution to maintain numerical stability without altering the physical interpretation of the results.

5.2.2 Eversion under Unconstrained Conditions (Free deployment)

Building on the material calibration and model validation performed during the inflation stage, the next step was to examine how internal boundary conditions influence the robot's deployment dynamics in a free environment. In the numerical formulation described in Section 4.3, eversion is modeled as a sequential release of mesh elements, simulating the gradual transition from a stored to a deployed state. In the proposed model, particular attention is given to the eversion zone — the region where the membrane progressively turns inside out under internal pressure. This zone represents the active front of motion and concentrates most of the mechanical transformations occurring during deployment. Proximal to this region, the material remains stored and does not contribute to the deformation process, while downstream, once eversion is completed, the structure behaves as a deployed tube mainly subjected to contact interactions. Accurately identifying and modeling this eversion zone is therefore essential to reproduce the mechanical stability of the process.

Within this framework, the length of the eversion zone determines the portion of the mesh released at each time step and directly affects the balance between deformation and numerical stability. Since internal pressure only acts as a secondary driver in free-deployment conditions, the analysis focused exclusively on this geometric parameter. A series of simulations was conducted using different eversion zone lengths, and the stability of the deployment was evaluated by computing the standard deviation of the robot tip displacement (Figure 5.8).

For TPU, a small eversion zone corresponding to 5% of the robot's total length

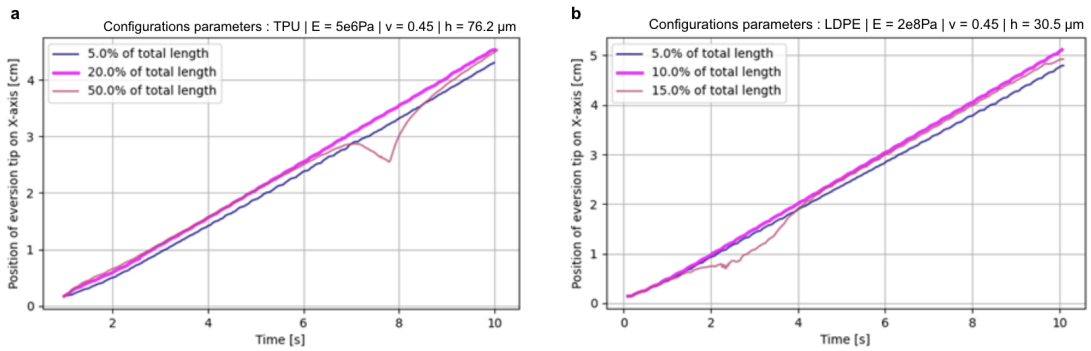


Figure 5.8: (a) For TPU, a small eversion zone (5% of total length) leads to localized stress concentrations and fluctuations ($\bar{x} = 0.045$ mm, $\sigma_x = 0.021$ mm), whereas a large zone (50%) induces oscillations and loss of guidance ($\bar{x} = 0.055$ mm, $\sigma_x = 0.044$ mm). An intermediate zone (20%) minimizes instabilities ($\bar{x} = 0.048$ mm, $\sigma_x = 0.018$ mm). (b) For LDPE, a 10% eversion zone optimizes stability ($\bar{x} = 0.049$ mm, $\sigma_x = 0.019$ mm).

results in local stress concentrations and mesh fluctuations ($\bar{x} = 0.045\,\text{mm}$, $\sigma_x = 0.021\,\text{mm}$). Conversely, a large eversion zone of 50% generates parasitic oscillations and a loss of guidance ($\bar{x} = 0.055\,\text{mm}$, $\sigma_x = 0.044\,\text{mm}$). An intermediate configuration of 20% provides a more favorable compromise, reducing instabilities ($\bar{x} = 0.048\,\text{mm}$, $\sigma_x = 0.018\,\text{mm}$) while maintaining a moderate computation time (371,980 ms).

For LDPE, a similar trend is observed, although the optimal range is narrower due to the higher stiffness of the material. Excessively large eversion zones increase mechanical stress and induce unwanted oscillations while raising computational cost. A smaller eversion zone of 10% reduces instabilities ($\bar{x} = 0.049\,\text{mm}$, $\sigma_x = 0.019\,\text{mm}$) and keeps the simulation time within acceptable limits (462,658 ms).

5.2.3 Eversion in a Constrained Environment

After the evaluation of the robot in a free environment, the analysis focused on its ability to progress through a constrained medium. The objective was to examine the influence of mechanical properties such as flexibility and stiffness on the ability to traverse narrowed passages representative of vascular stenoses. To this end, a stenotic environment mimicking the progressive narrowing of a vessel caused by stenosis was implemented both in simulation and experiment.

The constrained region consisted of a tubular channel 70 mm in length, initially 12 mm in diameter, gradually narrowing between 30 mm and 40 mm along its length.

Two target diameters were selected for the study: 5 mm, representing a moderate constriction, and 4 mm, corresponding to a severe stenosis still compatible with a TAVI-type procedure. A more extreme diameter of 3 mm was not considered, as it represents an excessive obstruction generally regarded as a clinical contraindication to the procedure. Since the constriction was modeled as non-deformable in simulation, the corresponding physical prototype was fabricated in resin (*Clear Resin*, Formlabs) to impose comparable structural constraints.

In both simulation and experimental setups, eversion was driven by progressive internal pressurization. In simulation, this was implemented by dynamically adjusting the pressure in proportion to the everted volume, following a linear relation calibrated from the eversion pressure. This formulation ensured a gradual increase in the internal load as the mesh unfolded, maintaining consistent eversion dynamics throughout the process. Experimentally, pressure was gradually increased using the system described in Section 5.1.1, following a specific protocol designed to reproduce the simulation conditions and allow direct comparison of results.

For the tests conducted with the LDPE robot, both the simulation and the physical experiments failed to cross the 5 mm stenosis (Figure 5.9). In simulation, the initial pressurization induced localized swelling near the robot base, followed by a *double-growth* phenomenon: internal membrane segments appeared to advance while the distal tip remained stationary. This behavior, incompatible with realistic eversion mechanics, indicated excessive internal constraint and a high likelihood of rupture. Consistently, the physical experiments also failed, with membrane rupture observed around 90 kPa. The correspondence between the instability predicted numerically and the experimental failure suggests that the rigidity and low compliance of LDPE are major limiting factors, reducing its ability to navigate through severe stenoses.

In the numerical model, the TPU robot successfully traversed both stenoses (Figure 5.10). At the exit of the constriction, the effective crossing pressure P_c reached approximately 35 kPa. During traversal, a contact-induced bending appeared up-

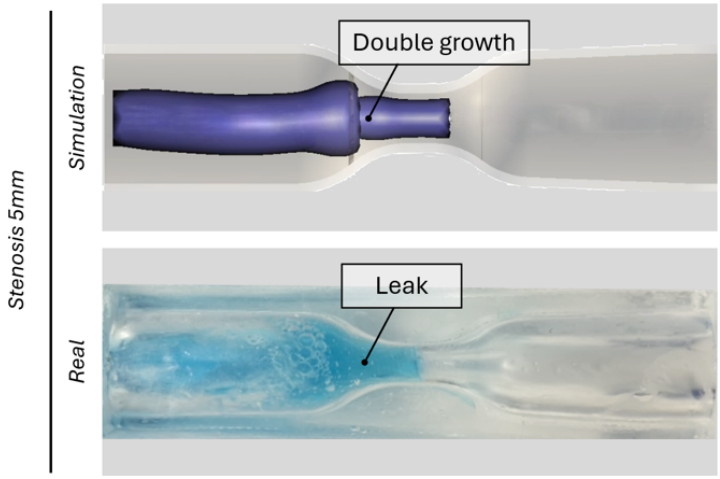


Figure 5.9: Comparison between simulated and experimental behavior of the LDPE robot in a 5 mm stenosis, where eversion failure is observed in both cases. The simulation exhibits a non-physical double-growth effect, with mesh progression occurring without distal displacement. Experimentally, excessive pressure causes upstream swelling and rupture, leading to leakage.

stream of the constriction, allowing the mesh to conform to the reduced lumen. No significant radial expansion was observed, indicating that the robot adapted geometrically to the constraint without additional inflation.

Experimental tests confirmed the ability of the TPU robot to pass through both constrictions, while revealing notable differences in the pressure regimes and associated deformation modes. For the 5 mm stenosis, traversal occurred at a mean crossing pressure ($P_c = 33.1 \pm 2.5$ kPa, $n = 5$), slightly below the characteristic deformation threshold ($P_d \approx 35$ kPa). At this level of stress, moderate upstream swelling was observed but did not compromise the robot's structural integrity; it recovered its initial geometry after passage, without residual deformation.

However, crossing a severe 4 mm stenosis required much higher pressure ($P_c = 67 \pm 3.1$ kPa, $n = 5$), far exceeding the irreversible deformation threshold. This loading caused pronounced radial expansion upstream, leading to full contact with the inner walls of the phantom, whose initial diameter was 12 mm. Under these conditions, deformation exceeded the elastic range of TPU, inducing permanent alterations of the structure. Although eversion continued and traversal was achieved, the high stress levels indicated an increased risk of local weakening, highlighting the material's safety limits under severe stenotic conditions.

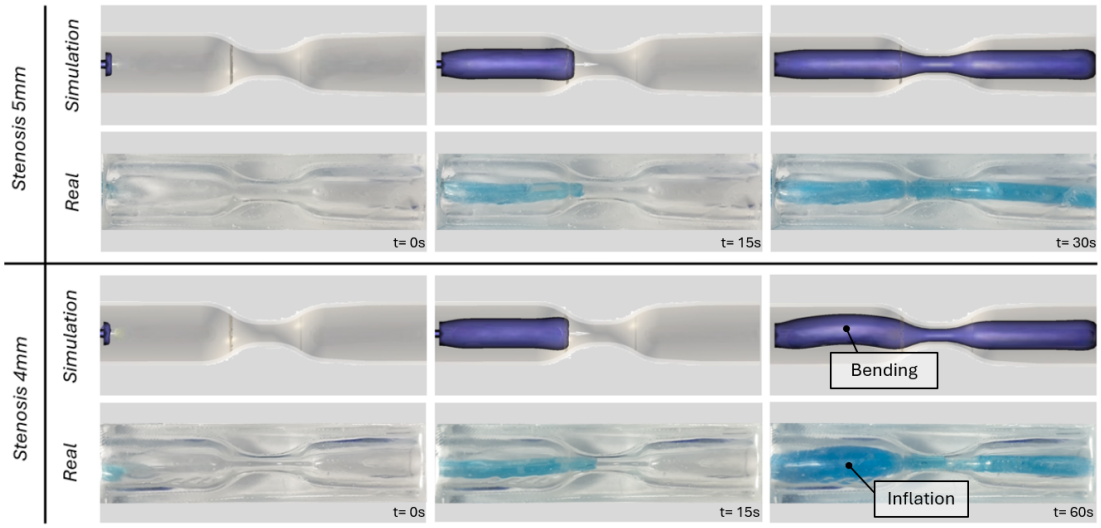


Figure 5.10: Comparison between simulated and experimental deformation profiles of the 6 mm-diameter TPU robot during eversion in stenotic geometries. In both cases, traversal is successful for constrictions of 5 mm and 4 mm. The simulation shows contact-induced bending without radial expansion, indicating geometric adaptation to the lumen. In contrast, the experiment reveals upstream swelling, particularly pronounced in the 4 mm case due to higher internal pressure, leading to temporary or irreversible mesh deformation.

These experimentally observed behaviors, however, contrast with the simulation results, where no upstream swelling was predicted. This discrepancy directly stems from the modeling assumptions: the wall was considered perfectly rigid and the contact frictionless. In experimental conditions, the finite stiffness of the conduit and surface friction modify the internal pressure distribution, promoting localized expansion upstream of the constriction. This deviation underscores the importance of contact conditions in accurately reproducing observed behavior and suggests that a more realistic contact model would be required to fully capture the experimental dynamics.

Beyond mechanical and numerical considerations, the potential clinical evaluation of the pressure levels reached is a key aspect. To place them in perspective, these values were compared with the Nominal Pressure (NP) and Rated Burst Pressure (RBP) typically reported for coronary stent deployment (Table 5.6) [116]. In a free environment, the stable eversion pressure of TPU remains low ($P_e = 18$ kPa), reflecting moderate internal stress. In the presence of constrictions, crossing pressures increase with stenosis severity, averaging 33.1 kPa for a 5 mm diameter

and 67.0 kPa for a 4 mm stenosis. Even in the latter case, the maximum recorded value remains about seventeen times lower than the minimum nominal pressures required for coronary stent deployment ($\geq$ 1117 kPa).

System	**NP [kPa]**	**RBP [kPa]**
Medtronic Resolute Onyx [117]	1216	1824
Boston Scientific Promus ELITE [118]	1117	1827
Boston Scientific Synergy [119]	1117	1827

Condition	P_c **[kPa]**	**NP [kPa]**	P_c**/NP**
Stenosis 5 mm	33.1	1117	1 : 34
Stenosis 4 mm	67.0	1117	1 : 17

Table 5.6: (Top) Nominal Pressure (NP) and Rated Burst Pressure (RBP) of commercial coronary stents. (Bottom) Ratio between the crossing pressure P_c of the TPU robot and the nominal stent deployment pressure.

This comparison shows that the robot maintains stress levels well below those typically required for intravascular device deployment, even when locally exceeding its elastic limit. This behavior suggests a potential clinical advantage, as the interaction with vessel walls remains gentler and is therefore less likely to induce critical complications such as ruptures or dissections during TAVI. Nevertheless, this interpretation should be nuanced, as the experimental conditions were based on rigid models, whereas real vessels exhibit heterogeneous compliance, often altered by atherosclerotic plaques or calcifications.

Under continuous pressurization, the TPU robot successfully traversed stenoses, although the pressures required in constricted regions were markedly higher than in free conditions, reflecting the additional mechanical constraints associated with crossing. To further reduce these threshold pressures, the actuation strategy was modified. Pulsed pressurization profiles were evaluated as an alternative, under the hypothesis that cyclic variations could help overcome distal friction and facilitate eversion in confined geometries. A dedicated dynamic actuation module was therefore developed (Section 5.1.1), capable of generating sinusoidal pressure cycles between 2.5 and 10 Hz.

Tests conducted on the TPU did not reveal any improvement compared to con-

tinuous pressurization: neither the crossing pressure nor the eversion kinematics showed significant variations, and no reduction of upstream swelling phenomena was observed. The LDPE, although part of the selected materials, was not included in this series of tests, as previous experiments had already demonstrated its early rupture during moderate stenosis crossings, preventing any meaningful evaluation under pulsed loading conditions. Conversely, PTFE was selected for its high mechanical resistance. The objective was to determine whether, in a regime where the material could tolerate high pressures without immediate failure, a pulsed modulation of pressure could facilitate progression through the constrained region. Once again, the results were negative: pulsed pressurization failed to ensure stable eversion and led to the onset of irreversible deformations in the early deployment phases. The convergence of these observations for two materials with contrasting mechanical behaviors suggests that, under the tested conditions, pulsed pressure modulation is unlikely to provide significant benefits for the traversal of stenotic regions. As no improvement was observed in either case, this approach was not further explored in subsequent experiments.

5.3 Preclinical validation

The previous results demonstrated that TPU, owing to its low eversion pressure and high compliance, is a particularly suitable material for TAVI applications. Consequently, the preclinical phase aimed to confirm this suitability under anatomically realistic conditions by assessing the feasibility of complete deployment up to the aortic valve while maintaining a traversable lumen for the introduction of instruments[1].

The validation strategy followed a stepwise approach in which each stage added a new layer of anatomical or physiological complexity. This progression was intended to evaluate the robot's performance under conditions gradually approaching those of an actual TAVI procedure. Three complementary models were therefore used: (1) anatomical phantoms, allowing initial exploration of the robot's behavior in controlled vascular geometries, with or without fluid circulation; (2) a

[1]In cadaveric and porcine models, the exact condition of the arteries (possible presence of stenoses, calcifications, etc.) cannot be defined a priori, which limits the ability to specifically target stenotic cases.

human cadaveric model, introducing the complexity of a realistic arterial network while remaining free from hemodynamic flow; (3) and a live porcine model, combining physiological anatomy with pulsatile circulation. The evaluation focused on several complementary aspects: the feasibility of continuous navigation up to the aortic valve, the maintenance of a traversable central lumen, the stability of pressure regulation around a setpoint value, as well as safety and performance metrics including deployment time, absence of leakage, and preservation of the robot's structural integrity.

5.3.1 Mechanical Integration with the Delivery Channel

The TPU robot, shaped to replicate the geometry of the human aorta, was fabricated following the process described in Section 5.1.2. The substrate was cut to a length of 700 mm, corresponding to the pathway between the femoral artery bifurcation and the beginning of the aortic arch. At its distal end, a curvature radius of 50 mm was integrated to reproduce the configuration of the aortic arch. Once completed, a microtube made of Polyurethane (PU) was thermally bonded to the distal end of the robot at 180°C for 5 seconds (Figure 5.11). The strength of this junction was evaluated through five manual traction tests, yielding an average maximum load of 7.99 N (*Force Gauge FK100*, Sauter), confirming its mechanical integrity under pressure.

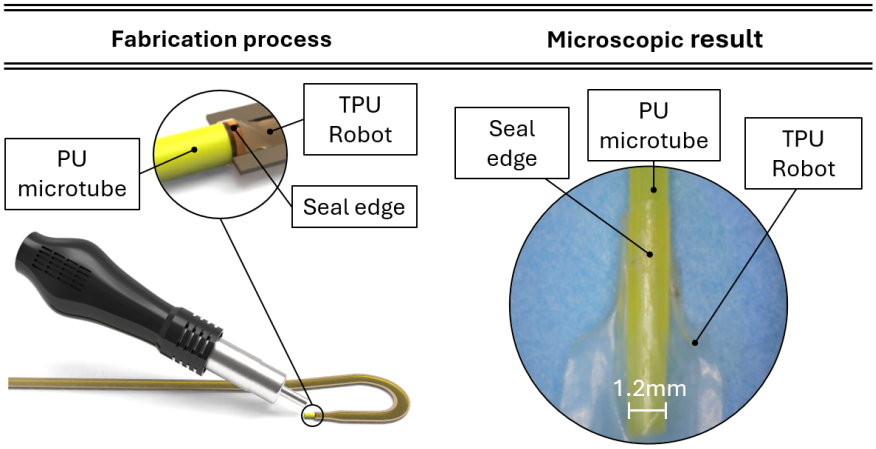


Figure 5.11: Sealing interface between a PU microtube and the TPU robot. The microtube is thermally bonded to the distal end of the TPU robot, forming a robust sealing interface.

A delivery channel (*OACL-7-9*, Oasis) made of Polyethylene and suitable for instrument insertion was then inserted into the microtube. The mechanical connection between the microtube (inner diameter: 1.2 mm) and the delivery channel (outer diameter: 1.67 mm) relies on the radial tension generated by stretching the microtube around the channel. Moreover, the combination of the rough surface properties of PU and the rigidity of Polyethylene increases friction between the two components, thereby reducing the risk of slippage. This configuration ensures optimal sealing and prevents any displacement even under high pressure.

To prevent fluid leakage while allowing the advancement of the delivery channel, a dynamic occlusion module was developed (Figure 5.12). This module uses a flexible silicone tube whose ends are subjected to adjustable torsion via a servomotor (*XL330-M288-T*, Dynamixel). Initially, a 360° rotation reduced the internal diameter of the tube from 10 mm to 0 mm, but this torsion proved insufficient to ensure effective sealing under the applied pressures. Consequently, an increased torsion of 900° (two and a half turns) was adopted, providing reliable sealing capable of withstanding pressures exceeding 100 kPa. Although this additional torsion increases friction between the tube and the channel, it remains low enough to allow longitudinal motion of the channel without deformation.

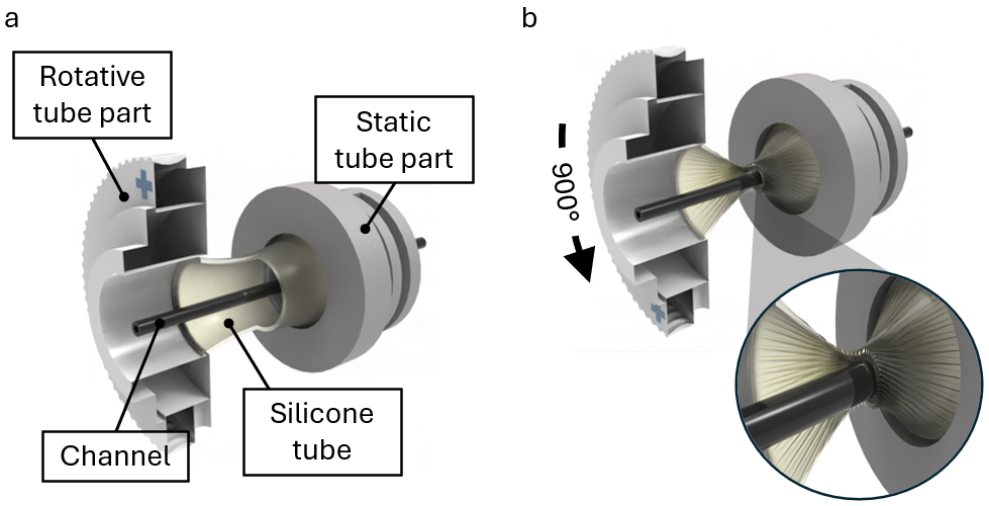


Figure 5.12: (a) Dynamic occlusion module using a silicone tube connected to two distinct parts: a fixed section and a rotating section. (b) To ensure sealing, the rotating part performs a 900° rotation, inducing controlled torsion of the silicone tube. This blocks fluid passage around the channel while allowing its longitudinal movement.

To move the delivery channel through the occlusion module, a drive system using opposing PU wheels was implemented (Figure 5.13). Each wheel is actuated by a servomotor (*XL330-M288-T*, Dynamixel). With a Shore A90 hardness, PU provides sufficient rigidity to generate the friction required for channel movement while remaining flexible enough to avoid damaging it. A centering hole keeps the channel aligned upstream and downstream of the wheels, minimizing the risk of slippage or lateral deviation and ensuring stable positioning throughout its displacement.

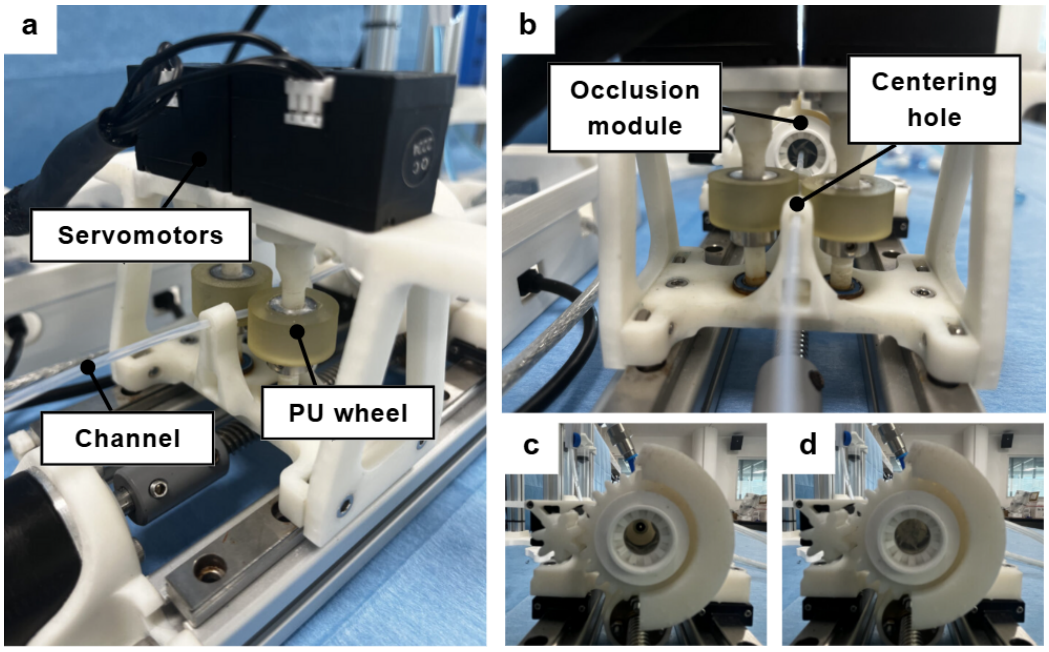


Figure 5.13: (a) Drive system composed of servomotors actuating opposing PU wheels, ensuring controlled longitudinal displacement of the channel. (b) Occlusion module in operational configuration, integrating a centering hole to maintain alignment during motion. (c) Module in open state, allowing free passage of the channel. (d) Module in closed state, providing effective sealing under internal pressurization.

5.3.2 Autonomous Deployment and Control

To validate the robot's deployment under clinically relevant conditions, the first experiments were conducted in three stages: in a free environment, within a static anatomical phantom, and within a dynamic phantom simulating physiological blood flow. The anatomical phantom (Figure 5.14) reproduces the human

vascular pathway from the femoral artery to the aortic valve, with an average diameter of 8 mm and a curvature radius of 50 mm at the aortic arch. In the dynamic configuration, a saline circulation system driven by a 5 L/min pump (*DCS-1200*, Jecod) was used to mimic systemic flow conditions.

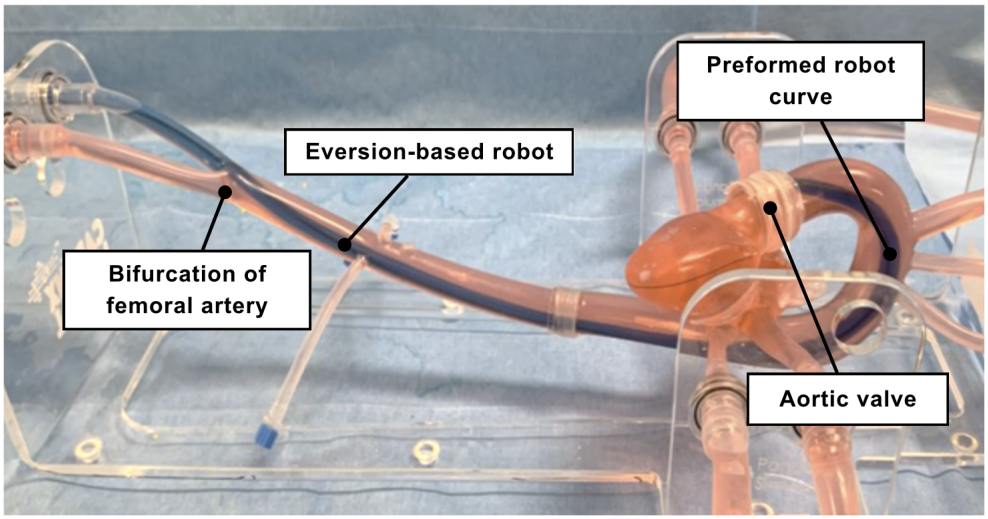


Figure 5.14: Autonomous deployment of the eversion-based robot within a dynamic vascular phantom reproducing the iliac–aortic pathway. The TPU eversion-based robot progresses from the femoral artery bifurcation to the aortic valve (∼600 mm), following the preformed curvature of the phantom, including a 50 mm radius at the aortic arch.

Eversion-based deployment requires precise coordination between internal pressurization and the advancement of the delivery channel to maintain adequate tension in the robot. To achieve this, a pressure-regulated actuation system was developed (Figure 5.15), combining the injection unit with the delivery channel mechanism. The system operates under a closed-loop control scheme based on a simple proportional law. The measured pressure is continuously compared to a fixed setpoint corresponding to the TPU eversion maintenance pressure, i.e., 18 kPa (Table 5.2), and reacts accordingly: when the pressure falls below the setpoint, the syringe pump injects additional fluid; when it exceeds the setpoint, the delivery channel advances, increasing the internal volume and thus reducing the excess pressure. Although the saline solution is incompressible, pressure variations arise from the geometric deformation of the robot. Within the tested range, these effects produce an approximately linear pressure–volume relationship, allowing for stable and predictable regulation.

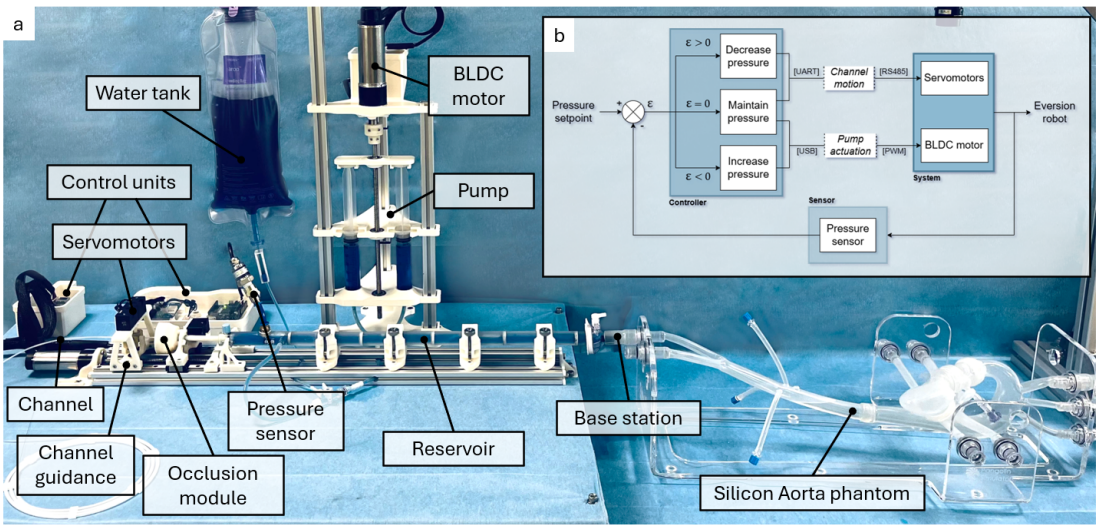


Figure 5.15: (a) The system includes a reservoir in which the robot body is stored prior to deployment. This reservoir is pressurized by a syringe pump module driven by a BLDC motor, allowing continuous fluid injection from an external tank. Internal pressure is monitored and regulated by a pressure sensor, ensuring stable and controlled eversion of the robot from its base station. In parallel, a channel guidance mechanism, actuated by servomotors, ensures synchronized advancement of the channel fixed to the distal end of the robot, maintaining coordinated motion throughout deployment. The entire system operates within a silicone phantom reproducing the geometry and compliance of the vascular environment. Electronic control units drive the actuators and sensors, providing precise regulation and data acquisition. (b) The system operates under a closed-loop control scheme based on a proportional controller. The measured internal pressure is continuously compared to a fixed setpoint (18 kPa). When the pressure drops below the setpoint, the syringe pump driven by the BLDC motor injects additional fluid; conversely, when the pressure exceeds the setpoint, the servomotor-driven channel guidance mechanism advances to increase the internal volume and reduce pressure.

The choice of a single proportional controller was motivated by a dual objective: ensuring implementation simplicity while providing sufficient robustness for proof-of-concept validation. This approach guarantees reliable regulation under standardized experimental conditions, where external disturbances and tissue variability remain limited. However, this control scheme also presents certain limitations. In particular, it does not account for potential variations in friction or tissue compliance that may arise in more realistic scenarios, which could affect regulation accuracy and deployment stability.

Experimental results show that the robot can automatically and reliably navigate the entire simulated pathway, from the iliac bifurcation to the aortic valve (≈60 cm), with performance variations depending on the environment (Figure 5.16). Deployment time was longest in the free environment (13:36 ± 1:39, min:s). In the absence of confining walls, the pressure regulation becomes less stable, as small variations in internal volume are not counterbalanced by external constraints. This results in transient pressure fluctuations that slow down the overall progression and induce slight lateral drifts, requiring continuous realignment of the robot's trajectory. In contrast, confinement within the static phantom significantly reduced the deployment time (10:57 ± 0:12, min:s) by limiting such drifts and promoting a more stable and linear trajectory. In the pressurized phantom, where hydrodynamic forces are introduced, deployment time slightly increased (12:29 ± 0:06, min:s) compared to the static phantom[2]. This delay highlights the influence of fluid dynamics, which introduces additional constraints that are continuously compensated for by the pressure-based control system. Finally, all tests confirmed that the central lumen remained fully traversable throughout deployment, enabling the insertion of a guidewire in the final position, thus demonstrating the robot's compatibility with standard endovascular use.

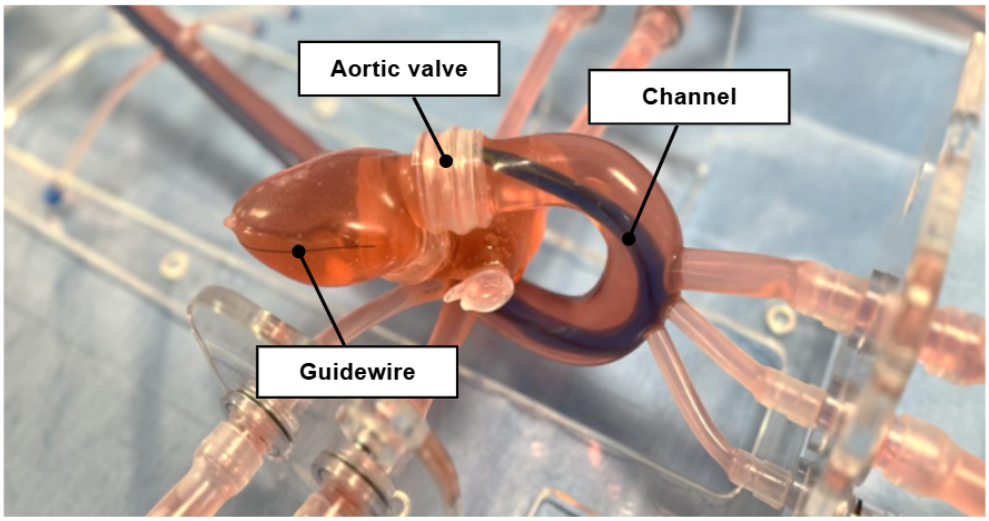


Figure 5.16: Autonomous deployment of the eversion-based robot within a dynamic vascular phantom reproducing the iliac–aortic pathway. A central lumen is maintained throughout the robot body, allowing guidewire insertion once the robot reaches its final position at the aortic valve.

[2]A video of the full deployment in a vascularized phantom, accelerated by a factor of 35, is available with the manuscript (file name: `Deployment_w_Vascularisation_x35`).



Figure 5.17: (a) Actuation system implemented on the cadaveric model, integrating the pressurization reservoir and the control unit, used to assess the feasibility of eversion within a human vascular anatomy. (b) Introduction of the eversion-based robot directly into the femoral artery, surgically exposed for access, and connected to the base station and the reservoir filled with saline solution and contrast agent.

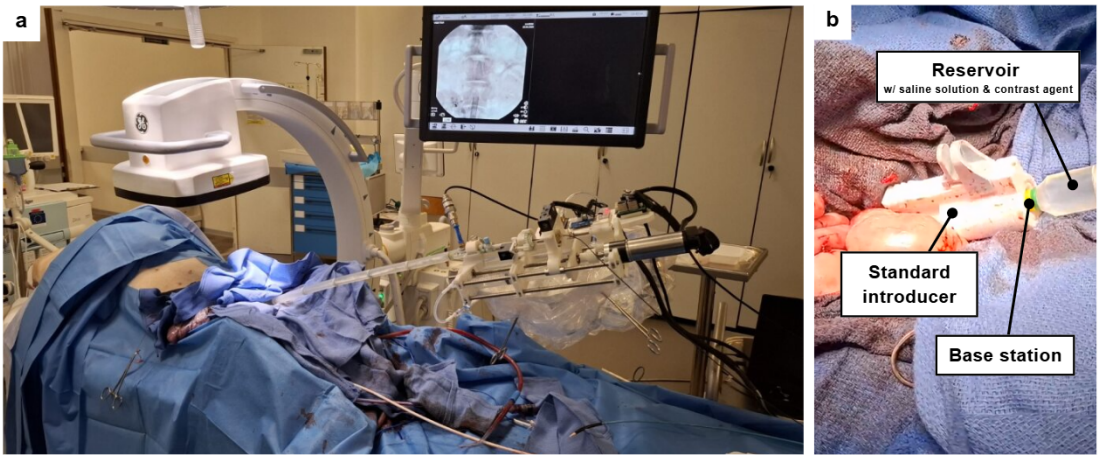


Figure 5.18: (a) Actuation system implemented on the porcine model, integrating the pressurization reservoir and the control unit, used to evaluate eversion feasibility under physiological conditions. (b) Femoral access of the robot through a standard 20 Fr (6.7 mm) introducer, connected to the base station and to the reservoir filled with saline solution and contrast agent.

5.3.3 Preclinical Evaluation in Biological Environments

Following the initial validations performed in synthetic phantoms, the evaluation was extended to a preclinical framework in order to confront the robot with more

representative biological environments. This stage relied on two complementary models : a human cadaver, allowing experimentation within a realistic vascular anatomy but without hemodynamic activity (Figure 5.17); and a live porcine model, providing a fully physiological context that integrates both vascular compliance and pulsatile blood flow (Figure 5.18). Human cadaveric experiments were conducted within authorized anatomical facilities in accordance with national regulations governing the use of donated bodies for research. All animal experiments were approved by the French Ministry of Research and the local Ethics Committee under protocol number APAFIS#38157, and all procedures were conducted in accordance with European and national regulations for the care and use of laboratory animals.

Vascular access was adapted to each model: direct dissection of the femoral artery for the human cadaver, and percutaneous femoral access through a standard 20 Fr (6.7 mm) introducer (*2064-HQS-20F*, Alcis) for the porcine model. This methodological progression—from a static cadaveric anatomy to a living organism—was designed to assess the feasibility of eversion-based deployment under increasingly complex conditions, while identifying the specific constraints associated with navigation in environments close to clinical practice.

In both setups, pressurization was performed using a mixture of 80% saline solution and 20% iodinated contrast agent (*Iomeron 350*), providing simultaneous internal pressurization and real-time fluoroscopic visualization. The closed-loop control system maintained the internal pressure around 18 kPa, with deployment durations of 6:28 (min:s) in the cadaveric model and 10:31 (min:s) in the porcine model. In the former, the robot advanced up to the iliac region without structural alteration, while in the latter it reached the proximal segment of the aortic arch, also without visible deformation or deviation from the intended trajectory (Figure 5.19).

The preclinical trials confirmed the feasibility of eversion-based deployment within biological environments, demonstrating that the robot could successfully initiate and sustain its progression in both models. However, they also revealed a recurring failure mode. Two ruptures occurred, respectively at 15 cm in the cadaveric model and at 40 cm in the porcine model. In both cases, they were located at the TPU junction, precisely in the region defined by the cutting offset (Figure 5.20).

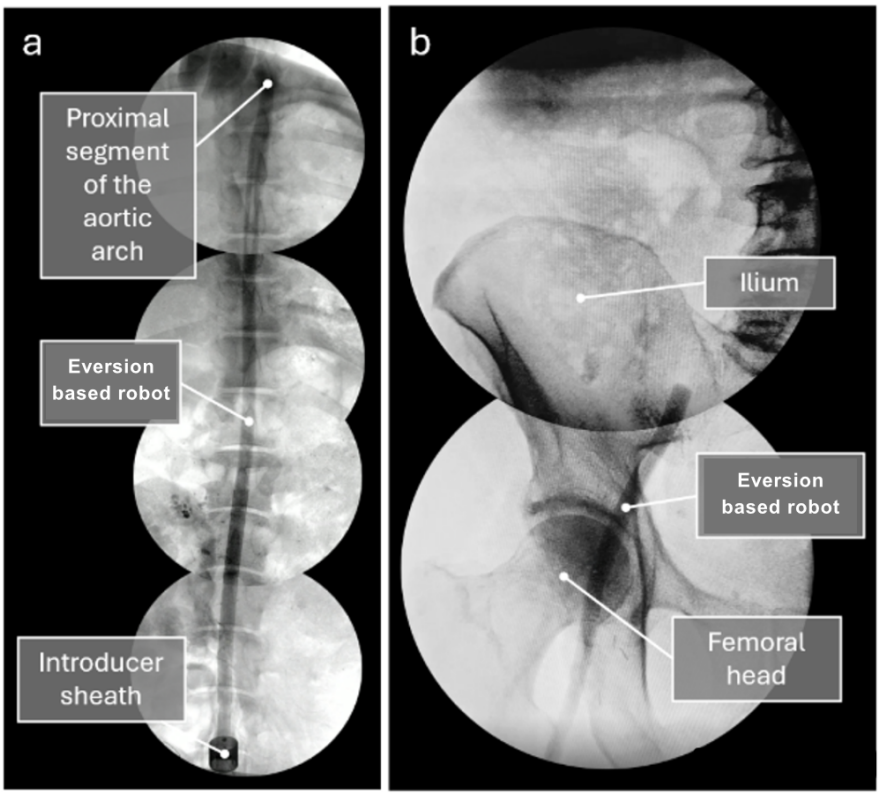


Figure 5.19: Anatomical tests reconstructed from combined fluoroscopic views. (a) Progression of the robot in the porcine model, from the introducer positioned in the femoral artery up to the proximal segment of the aortic arch. (b) Deployment in a human cadaver, advancing from the femoral artery to the iliac region.

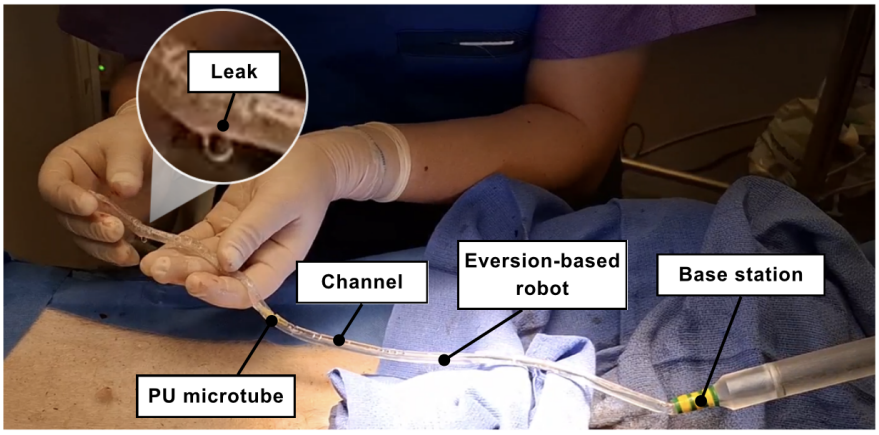


Figure 5.20: Post-deployment analysis on the porcine model showing the eversion-based robot on its base station, connected to the channel via the PU microtube. A leak was observed at the TPU junction, highlighting the structural weakness of the fusion line and leading to localized robot failure.

Designed to ensure impermeability, this area in practice concentrates the stresses generated during eversion, such that small irregularities in thickness or alignment are sufficient to weaken the weld. This structural vulnerability leads to local loss of integrity and, in a clinical context, could compromise sealing and cause fluid leakage, resulting in a loss of functional control. These results therefore identify the junction as a major weak point of the manufacturing process, justifying specific improvements to enhance the robot's reliability under preclinical conditions.

5.4 Conclusion

This fifth chapter represents a key milestone in the experimental validation of the design and control of the eversion-based robot, confronting modeling hypotheses with physical observations. The main objective was to establish the feasibility of a safe and automatic deployment within the context of TAVI.

The work began with the implementation of a dedicated experimental setup, integrating a modular test bench to ensure precise regulation of internal pressure and continuous fluid injection. The pressurized reservoir was filled with a physiological 0.9% NaCl saline solution and included a passive air chamber to stabilize the pressure and damp fluctuations during injection. The comparative material evaluation demonstrated the clear superiority of TPU over LDPE and other candidates, primarily due to its low stable eversion pressure ($P_e = 18$ kPa) and its high compliance. The thermo-compression manufacturing process, combined with laser cutting featuring an optimized 2 mm offset in the sealing area, proved essential to ensure both fluid tightness and mechanical strength of the junctions. Nevertheless, these results remain limited to preclinical evaluations in porcine and cadaveric models, and further testing will be required to confirm their robustness under clinical conditions.

The initial inflation evaluations confirmed a strong correlation between simulated and experimental results, with an average deviation of 0.46 mm for TPU and 0.01 mm for LDPE, attesting to the fidelity of the numerical model under these conditions. Sensitivity analysis further validated the predominance of membrane energy over bending energy in the mechanical predictions.

The tests performed in stenotic environments clearly revealed the limitations of LDPE, which failed to pass through a 5 mm stenosis, exhibiting non-physical deformations in simulation and membrane rupture during experiments. Conversely, the TPU robot successfully crossed severe constrictions of 5 mm and 4 mm. Although crossing the 4 mm stenosis required higher internal pressure, the maximum crossing pressures remained approximately seventeen times lower than the nominal deployment pressures of commercial coronary stent systems (minimum 1117 kPa). Continuous pressurization was confirmed to be sufficient for successful passage, as pulsed profiles provided no measurable benefit under the tested configurations. However, a notable discrepancy was observed between the model and the experiments: unlike the simulation, which predicted geometric adaptation without radial expansion, the experiments revealed an upstream swelling of the membrane, especially in the 4 mm stenosis. This divergence directly stems from simplifying modeling assumptions, such as rigid wall and frictionless contact, highlighting the need to refine the model by incorporating wall compliance and frictional effects in stress evaluation.

The preclinical validation demonstrated the TPU robot's ability to autonomously navigate within realistic anatomical and physiological environments. The integration of a Polyethylene delivery channel through a thermally bonded PU microtube provided a robust and leak-proof mechanical interface. Autonomous deployment was driven by a proportional closed-loop control system maintaining the internal pressure around the 18 kPa setpoint. Experiments conducted *in vivo* on a porcine model (up to the proximal segment of the aortic arch) and *ex vivo* on a human cadaver (up to the iliac region) confirmed the feasibility of navigation under realistic conditions. However, a recurrent failure mode was identified: localized ruptures occurred at the thermally bonded TPU junction (cutting offset zone), designating this area as a major structural weakness that requires further optimization of the fabrication process.

In summary, this chapter validated the eversion-based approach by establishing strong agreement between numerical predictions and experimental observations. This joint validation identified TPU as the most suitable material, demonstrating its ability to ensure controlled and atraumatic navigation within complex and stenotic vascular geometries. The results also confirmed the effectiveness of the closed-loop control system for autonomous deployment, reinforcing the relevance

of this technology for minimally invasive cardiovascular interventions.

Beyond these validations, several insights guide future developments. The discrepancies observed between simulation and experiments—particularly the proximal swelling absent from the numerical model—underline the limitations of current simplifying assumptions and the need to integrate wall compliance and frictional effects into the modeling. From a control perspective, the pressure-based proportional closed-loop regulation proved sufficient to establish the feasibility of autonomous deployment, but its adaptability remains limited in the face of anatomical variability. Exploring more advanced control strategies, such as PID or adaptive laws coupled with distal sensors, appears as a promising path to improve system robustness and precision. Finally, the localized ruptures observed at the thermally bonded junction confirm the need to optimize the manufacturing process, either through an adapted sealing geometry or by adopting alternative techniques such as ultrasonic or CO_2 laser welding [120, 121].

Chapter 6

Conclusion

The central objective of this thesis was to design and validate a soft eversion-based robot capable of navigating atraumatically within the vascular system, with the ultimate aim of application to TAVI.

6.1 Summary of Work and Contributions

Within this framework, a fundamental constraint arises: any solution intended for intravascular application must be actuated by a physiological fluid. The use of a pressurized gas would expose the patient, in the event of leakage, to a risk of gaseous embolism incompatible with clinical safety requirements. Fluid actuation using saline solution therefore constitutes a structural condition of the problem addressed in this work.

However, the initial experiments revealed a mechanical difficulty inherent to this configuration. The presence of an incompressible fluid inside the robot leads, under internal pressurization, to an increase in membrane tension during local geometric variations imposed by the vascular environment. Any reduction in cross-section or external constraint results in an immediate redistribution of stresses within the wall, thereby limiting the local adaptability that is one of the key advantages of the eversion mechanism. This reduction in effective compliance translated into elevated stresses transmitted to surrounding tissues, as illustrated

by an arterial rupture observed during a cadaveric experiment.

The scientific problem addressed in this thesis was therefore structured around the need to preserve the deformability and adaptability inherent to the eversion mechanism while integrating the mechanical effects induced by fluid pressurization imposed by endovascular safety constraints.

The work carried out led to three main contributions: (i) the development of a membrane-based modeling framework for eversion under internal pressurization, enabling predictive analysis of overconstraint phenomena; (ii) the establishment of a material design principle guided by numerical simulation and experimentally validated in order to restore effective compliance under internal pressure; (iii) the realization of a functional robotic system integrating an operating channel and a controlled pressure regulation strategy compatible with the mechanical and clinical requirements of the endovascular environment.

To address this challenge, a modeling framework was developed to explicitly represent the eversion mechanism as a pressurized membrane phenomenon, while preserving a coherent description of the global deployment kinematics. This approach enables characterization of the robot's behavior as a function of membrane material properties and analysis of the direct influence of these parameters on stress distribution, local stability, and adaptability in constrained environments. It thus constitutes a predictive tool designed to evaluate overconstraint effects induced by fluid pressurization, identify configurations prone to local instabilities, and guide design choices prior to experimental validation.

Based on insights obtained from the model, a material redesign of the robot was undertaken to control the stiffening induced by fluid pressurization. Simulation results highlighted the critical influence of membrane properties on the effective compliance of the device under internal pressure, thereby guiding the selection toward materials capable of maintaining local adaptability in constrained environments. This numerically informed choice was subsequently validated experimentally, confirming that a semi-extensible material limits the increase in effective stiffness observed in early prototypes and improves the ability to traverse severely constrained vascular geometries.

Building upon the selected material, a complete manufacturing process was de-

veloped to produce a functional robot integrating a central lumen dedicated to instrumentation. In parallel, a dedicated pressurization system was designed and implemented, incorporating pressure sensing and active regulation to ensure stable and controlled fluid actuation. A comprehensive experimental characterization of pressure regimes was then conducted to define operating conditions ensuring deployment stability, preservation of material integrity, and limitation of stresses transmitted to surrounding tissues. This approach made it possible to identify operating ranges compatible with endovascular use and to establish consistency between material design, actuation architecture, and clinical safety requirements.

All these developments were subsequently confronted with environments of increasing complexity. Following validation on an anatomical phantom reproducing the ilio-aortic tree, the system was evaluated in real biological environments, including a living porcine model and a human cadaveric model. These experiments aimed to assess the system under conditions approaching a complete procedural setting, incorporating anatomical, mechanical, and operational constraints characteristic of the clinical context. They enabled evaluation of the feasibility of fluid-actuated navigation in realistic conditions, while also revealing the performance achieved and the remaining technological barriers. Confronting the robot with real biological environments at this stage of development represents a significant step toward technological maturation and strengthens the credibility of its translational potential.

6.2 Future Research Directions

The results presented in this thesis demonstrate the feasibility of atraumatic navigation using a fluid-actuated eversion-based robot in constrained vascular environments. Nevertheless, several technological barriers remain and define clear directions for future work.

Localized ruptures observed at thermally bonded junctions, particularly in regions subjected to high stress concentrations, highlight assembly reliability as a critical issue. Future developments should therefore focus on optimizing junction geometry to improve stress redistribution, exploring more homogeneous bonding

techniques adapted to TPU, and implementing systematic quality control protocols including extended pressurization tests, standardized inspections, and fatigue characterization. Strengthening long-term durability and conducting thorough biocompatibility evaluations also constitute essential steps toward clinical application.

From a modeling perspective, improvements are required to better predict robot tissue interactions under realistic physiological conditions. Incorporating a nonlinear constitutive behavior for TPU would provide a more accurate representation of its mechanical response under pressurization. Explicit modeling of welded regions would improve the analysis of local stress concentrations. Moreover, contact handling remains computationally demanding during long deployments, calling for more efficient numerical strategies. Finally, explicitly accounting for vessel wall compliance and hemodynamic pulsatility would further bring the model closer to biological reality.

Beyond structural and numerical aspects, improving system observability represents an important development axis. Integration of embedded sensors could provide real-time information on pressure, deformation, and contact conditions, contributing to improved intraoperative monitoring and enhanced safety. These functionalities would primarily serve as decision-support and safety-enhancing tools rather than active control mechanisms.

6.3 Toward the Realization of a Complete TAVI Procedure

While the work presented demonstrates the feasibility of atraumatic endovascular navigation through fluid eversion, achieving a fully integrated TAVI procedure using such a device requires addressing several system-level integration challenges.

In its current configuration, the central lumen of the robot does not allow direct integration of a standard compressed prosthetic valve. Two architectural directions may be considered: either increasing the internal diameter to allow intraluminal transport of a crimped valve, or adopting an alternative configuration in which the prosthesis would be mounted at the distal end of the robot

and conveyed to the implantation site. Each of these options entails substantial geometric and mechanical reconfiguration of the device.

The primary challenge, however, lies in the valve deployment mechanism. Current TAVI prostheses rely on radial expansion mechanisms, either self-expanding or balloon-assisted. Integrating such a system at the tip of a pressurized membranous robot raises complex issues of mechanical interaction between the membrane and the prosthesis, management of radial forces transmitted to the aortic annulus, and longitudinal stability during the release phase.

In a coherent procedural scenario, the eversion mechanism would be interrupted once the target zone is reached, entering a stabilization phase prior to deployment. This step appears essential to ensure positioning accuracy compatible with clinical requirements, as implantation success depends on millimetric control relative to the aortic annulus. Coordination between internal pressure regulation, mechanical stability of the robot, and the deployment mechanism thus constitutes a central system-engineering challenge.

Repositioning also represents a critical issue. Contemporary TAVI systems incorporate partial recapture mechanisms allowing adjustment prior to definitive release. Transposing such functionality to an architecture based on an eversion membrane requires careful consideration of temporary prosthesis confinement strategies, controlled depressurization and withdrawal, as well as prevention of interference between the membrane and the valve during transitional phases.

Finally, the proposed architecture aims to replace the conventional catheter while maintaining compatibility with established interventional practices, including the use of standard guidewires and fluoroscopic guidance. Radiological visibility ensured by the use of contrast fluid represents an initial advantage; however, integration of dedicated radiopaque markers could further improve positioning accuracy and intraoperative readability.

6.4 Perspectives and Clinical Translation

Beyond targeted technical improvements, the principle of eversion-based navigation lies within a broader research domain already explored in several medical

specialties. Previous studies have demonstrated its relevance in neurosurgery, bronchoscopy, and colonoscopy, owing to its ability to progress atraumatically through fragile and sinuous pathways. These works confirm that the potential applications of this technology extend far beyond the cardiovascular field.

Building on these studies, exploratory work has also been initiated in the field of bariatric surgery (Appendix C). This adaptation illustrates the robot's capacity to be tailored to different anatomical environments, opening the door to various clinical uses depending on specific procedural requirements.

However, clinical translation of such a device does not rely solely on technological optimization. It requires thorough evaluation of long-term durability, compliance with regulatory frameworks, acceptance by practitioners, and medico-economic assessment to determine the real added value of the system compared with existing devices. Integration into surgical workflows and training of medical teams also constitute essential prerequisites.

Beyond specifically cardiovascular applications, the methods developed in this thesis have broader applicability. The membrane-based modeling framework under internal pressurization, as well as the simulation-guided design approach aimed at preserving effective compliance, can be transposed to other fluid-actuated soft devices. This methodology provides a generic tool for analyzing overconstraint phenomena and guiding material selection in progressively deploying systems.

Furthermore, the principle of eversion-based growing robots extends beyond the medical field. Potential applications include exploration of confined or hazardous environments, industrial inspection of complex conduits, and robotic exploration in constrained settings. In such contexts, the ability to progress atraumatically, continuously adapt geometry, and reduce contact forces represents a significant advantage.

References

[1] Goldstein, S., Jones, R., Sipe, J., Doppman, J., and Boretos, J. A miniature toposcopic catheter suitable for small diameter tortuous blood vessels. 1980.

[2] National Institutes of Health History of Medicine. Toposcopic catheter connected to a three-way stopcock. `https://nihhistory.catalogaccess.com/objects/326`, 1979. Accessed: 2025.

[3] Doppman, J. L., Goldstein, S. R., Jones, R. E., Boretos, J. W., and Bowman, R. The toposcopic catheter: a design for maneuvering through tortuous vessels. *Radiology*, 132(3):735–737, 1979.

[4] Ge, Q., Sakhaei, A. H., Lee, H., Dunn, C. K., Fang, N. X., and Dunn, M. L. Multimaterial 4d printing with tailorable shape memory polymers. *Scientific reports*, 6(1):31110, 2016.

[5] Zeng, H., Wani, O. M., Wasylczyk, P., and Priimagi, A. Light-driven, caterpillar-inspired miniature inching robot. *Macromolecular rapid communications*, 39(1):1700224, 2018.

[6] Tang, X., Li, K., Liu, Y., Zhou, D., and Zhao, J. A soft crawling robot driven by single twisted and coiled actuator. *Sensors and Actuators A: Physical*, 291:80–86, 2019.

[7] Cianchetti, M., Arienti, A., Follador, M., Mazzolai, B., Dario, P., and Laschi, C. Design concept and validation of a robotic arm inspired by the octopus. *Materials Science and Engineering: C*, 31(6):1230–1239, 2011.

[8] TolleyMichael, T., ShepherdRobert, F., GallowayKevin, C., WoodRobert, J., WhitesidesGeorge, M., et al. A resilient, untethered soft robot. *Soft robotics*, 2014.

[9] Plott, J. *Extrusion-based additive manufacturing of silicone elastomer parts*. PhD thesis, 2017.

[10] Hawkes, E. W., Blumenschein, L. H., Greer, J. D., and Okamura, A. M. A

soft robot that navigates its environment through growth. *Science Robotics*, 2(8):eaan3028, 2017.

[11] Sadeghi, A., Mondini, A., and Mazzolai, B. Toward self-growing soft robots inspired by plant roots and based on additive manufacturing technologies. *Soft robotics*, 4(3):211–223, 2017.

[12] Sadeghi, A., Mondini, A., Del Dottore, E., Mattoli, V., Beccai, L., Taccola, S., Lucarotti, C., Totaro, M., and Mazzolai, B. A plant-inspired robot with soft differential bending capabilities. *Bioinspiration & biomimetics*, 12(1): 015001, 2016.

[13] Blumenschein, L. H., Usevitch, N. S., Do, B. H., Hawkes, E. W., and Okamura, A. M. Helical actuation on a soft inflated robot body. In *2018 IEEE International Conference on Soft Robotics (RoboSoft)*, pages 245–252. IEEE, 2018.

[14] Agharese, N., Cloyd, T., Blumenschein, L. H., Raitor, M., Hawkes, E. W., Culbertson, H., and Okamura, A. M. Hapwrap: Soft growing wearable haptic device. In *2018 IEEE International Conference on Robotics and Automation (ICRA)*, pages 5466–5472. IEEE, 2018.

[15] Greer, J. D., Morimoto, T. K., Okamura, A. M., and Hawkes, E. W. A soft, steerable continuum robot that grows via tip extension. *Soft robotics*, 6(1):95–108, 2019.

[16] Luong, J., Glick, P., Ong, A., DeVries, M. S., Sandin, S., Hawkes, E. W., and Tolley, M. T. Eversion and retraction of a soft robot towards the exploration of coral reefs. In *2019 2nd IEEE International Conference on Soft Robotics (RoboSoft)*, pages 801–807. IEEE, 2019.

[17] Abrar, T., Putzu, F., Konstantinova, J., and Althoefer, K. Epam: Eversive pneumatic artificial muscle. In *2019 2nd IEEE International Conference on Soft Robotics (RoboSoft)*, pages 19–24. IEEE, 2019.

[18] Takahashi, T., Watanabe, M., Tadakuma, K., Konyo, M., and Tadokoro, S. Retraction mechanism of soft torus robot with a hydrostatic skeleton. *IEEE Robotics and Automation Letters*, 5(4):6900–6907, 2020.

[19] Jeong, S.-G., Coad, M. M., Blumenschein, L. H., Luo, M., Mehmood, U., Kim, J. H., Okamura, A. M., and Ryu, J.-H. A tip mount for transporting sensors and tools using soft growing robots. In *2020 IEEE/RSJ International Conference on Intelligent Robots and Systems (IROS)*, pages 8781–8788. IEEE, 2020.

[20] Satake, Y., Takanishi, A., and Ishii, H. Novel growing robot with inflatable structure and heat-welding rotation mechanism. *IEEE/ASME Transactions on Mechatronics*, 25(4):1869–1877, 2020.

[21] Kim, J.-h., Jang, J., Lee, S.-m., Jeong, S.-G., Kim, Y.-J., and Ryu, J.-H. Origami-inspired new material feeding mechanism for soft growing robots to keep the camera stay at the tip by securing its path. *IEEE Robotics and Automation Letters*, 6(3):4592–4599, 2021.

[22] Takahashi, T., Tadakuma, K., Watanabe, M., Takane, E., Hookabe, N., Kajiahara, H., Yamasaki, T., Konyo, M., and Tadokoro, S. Eversion robotic mechanism with hydraulic skeletonto realize steering function. *IEEE Robotics and Automation Letters*, 6(3):5413–5420, 2021.

[23] Gruebele, A. M., Zerbe, A. C., Coad, M. M., Okamura, A. M., and Cutkosky, M. R. Distributed sensor networks deployed using soft growing robots. In *2021 IEEE 4th International Conference on Soft Robotics (RoboSoft)*, pages 66–73. IEEE, 2021.

[24] Satake, Y. and Ishii, H. Pitch-up motion mechanism with heat welding by soft inflatable growing robot. *IEEE Robotics and Automation Letters*, 7(2): 5071–5078, 2022.

[25] Hausladen, M. M., Zhao, B., Kubala, M. S., Francis, L. F., Kowalewski, T. M., and Ellison, C. J. Synthetic growth by self-lubricated photopolymerization and extrusion inspired by plants and fungi. *Proceedings of the National Academy of Sciences*, 119(33):e2201776119, 2022.

[26] Wu, Z., Sadati, S. H., Rhode, K., and Bergeles, C. Vision-based autonomous steering of a miniature eversion growing robot. *IEEE Robotics and Automation Letters*, 8(11):7841–7848, 2023.

[27] Pi, X., Szczech, I. A., and Cao, L. A retractable soft growing robot with a flexible backbone. In *2023 IEEE/RSJ International Conference on Intelligent Robots and Systems (IROS)*, pages 2477–2484. IEEE, 2023.

[28] Jitosho, R., Simón-Trench, S., Okamura, A. M., and Do, B. H. Passive shape locking for multi-bend growing inflated beam robots. In *2023 IEEE International Conference on Soft Robotics (RoboSoft)*, pages 1–6. IEEE, 2023.

[29] Al-Dubooni, M., Wong, C., and Althoefer, K. Hybrid continuum-eversion robot: Precise navigation and decontamination in nuclear environments using vine robot. In *2024 IEEE/RSJ International Conference on Intelligent*

Robots and Systems (IROS), pages 12443–12449. IEEE, 2024.

[30] Satake, Y., Ishii, H., and Hirai, S. On-demand branching mechanism using heat cutting for soft inflatable growing robot. *IEEE Robotics and Automation Letters*, 2024.

[31] Do, B. H., Wu, S., Zhao, R. R., and Okamura, A. M. Stiffness change for reconfiguration of inflated beam robots. *Soft robotics*, 11(5):779–790, 2024.

[32] Wu, Z., Sadati, H., Vartholomeos, P., Abdelaziz, M. E., Temelkuran, B., Petrou, G., Booth, T., Shapey, J., Ahmed, A., and Bergeles, C. Vine4spine: A steerable tip-growing robot with contact force estimation for navigation in the spinal subarachnoid space. In *Vine4Spine: A Steerable Tip-Growing Robot with Contact Force Estimation for Navigation in the Spinal Subarachnoid Space*. 2025.

[33] Watson, C. and Morimoto, T. K. Permanent magnet-based localization for growing robots in medical applications. *IEEE Robotics and Automation Letters*, 5(2):2666–2673, 2020.

[34] Li, M., Obregon, R., Heit, J. J., Norbash, A., Hawkes, E. W., and Morimoto, T. K. Vine catheter for endovascular surgery. *IEEE Transactions on Medical Robotics and Bionics*, 3(2):384–391, 2021.

[35] Girerd, C., Alvarez, A., Hawkes, E. W., and Morimoto, T. K. Material scrunching enables working channels in miniaturized vine-inspired robots. *IEEE Transactions on Robotics*, 2024.

[36] Dehghani, H., Welch, C. R., Pourghodrat, A., Nelson, C. A., Oleynikov, D., Dasgupta, P., and Terry, B. S. Design and preliminary evaluation of a self-steering, pneumatically driven colonoscopy robot. *Journal of medical engineering & technology*, 41(3):223–236, 2017.

[37] Putzu, F., Abrar, T., and Althoefer, K. Plant-inspired soft pneumatic eversion robot. In *2018 7th IEEE International Conference on Biomedical Robotics and Biomechatronics (Biorob)*, pages 1327–1332. IEEE, 2018.

[38] Pore, A., Piccinelli, N., De Rossi, G., Piano, M., Meli, D., Dall'Alba, D., Muradore, R., and Fiorini, P. Endovine: Soft robotic endoscope for colonoscopy. In *Proceedings of the 14th Hamlyn Symposium on Medical Robotics*, pages 117–118, 2022.

[39] Giri, A., Girerd, C., Cervera-Torralba, J., Tolley, M. T., and Morimoto, T. K. Inchigrab: An inchworm-inspired guided retraction and bending device for vine robots during colonoscopy. *IEEE/ASME Transactions on*

Mechatronics, 2025.

[40] Berthet-Rayne, P., Sadati, S. H., Petrou, G., Patel, N., Giannarou, S., Leff, D. R., and Bergeles, C. Mammobot: A miniature steerable soft growing robot for early breast cancer detection. *IEEE Robotics and Automation Letters*, 6(3):5056–5063, 2021.

[41] Larrea, C., Berthet-Rayne, P., Sadati, S. H., Leff, D. R., Bergeles, C., and Georgilas, I. Growing robotic endoscope for early breast cancer detection: Robot motion control. In *Towards Autonomous Robotic Systems: 22nd Annual Conference, TAROS 2021, Lincoln, UK, September 8–10, 2021, Proceedings 22*, pages 391–401. Springer, 2021.

[42] Wu, Z., Reyzabal, M. D. I., Sadati, S. H., Liu, H., Ourselin, S., Leff, D., Katzschmann, R. K., Rhode, K., and Bergeles, C. Towards a physics-based model for steerable eversion growing robots. *IEEE robotics and automation letters*, 8(2):1005–1012, 2023.

[43] Al Harthy, S., Sadati, S. H., Wu, Z., Seneci, C. A., and Bergeles, C. Variable stiffness soft eversion growing robot via temperature control of low-melting point alloy pressurised medium. In *2024 International Symposium on Medical Robotics (ISMR)*, pages 1–7. IEEE, 2024.

[44] Davy, J., Greenidge, N. J., Kim, S., Tinsley, L. J., Lloyd, P., Chandler, J. H., Harris, R. A., Morimoto, T. K., and Valdastri, P. Vine robots with magnetic skin for surgical navigations. *IEEE Robotics and Automation Letters*, 9(8):6888–6895, 2024.

[45] Slade, P., Gruebele, A., Hammond, Z., Raitor, M., Okamura, A. M., and Hawkes, E. W. Design of a soft catheter for low-force and constrained surgery. In *2017 IEEE/RSJ International Conference on Intelligent Robots and Systems (IROS)*, pages 174–180. IEEE, 2017.

[46] Jitosho, R., Agharese, N., Okamura, A., and Manchester, Z. A dynamics simulator for soft growing robots. In *2021 IEEE International Conference on Robotics and Automation (ICRA)*, pages 11775–11781. IEEE, 2021.

[47] Aluru, J. S., Barsouk, A., Saginala, K., Rawla, P., and Barsouk, A. Valvular heart disease epidemiology. *Medical sciences*, 10(2):32, 2022.

[48] Cribier, A. Les 20 ans du tavi, 2022. Communication orale au Congrès HIGH TECH 2022, Paris, France. Disponible sur `https://youtu.be/Sc3YnKZ8RNQ?si=t5OlI8nu4E-1TOrb`.

[49] Cribier, A., Eltchaninoff, H., Bash, A., Borenstein, N., Tron, C., Bauer,

F., Derumeaux, G., Anselme, F., Laborde, F., and Leon, M. B. Percutaneous transcatheter implantation of an aortic valve prosthesis for calcific aortic stenosis: first human case description. *Circulation*, 106(24):3006–3008, 2002.

[50] Webb, J. G., Pasupati, S., Humphries, K., Thompson, C., Altwegg, L., Moss, R., Sinhal, A., Carere, R. G., Munt, B., Ricci, D., et al. Percutaneous transarterial aortic valve replacement in selected high-risk patients with aortic stenosis. *Circulation*, 116(7):755–763, 2007.

[51] Carabello, B. A. Transcatheter aortic-valve implantation for aortic stenosis in patients who cannot undergo surgery. *Current cardiology reports*, 13: 173–174, 2011.

[52] Reardon, M. J., Van Mieghem, N. M., Popma, J. J., Kleiman, N. S., Søndergaard, L., Mumtaz, M., Adams, D. H., Deeb, G. M., Maini, B., Gada, H., et al. Surgical or transcatheter aortic-valve replacement in intermediate-risk patients. *New England journal of medicine*, 376(14):1321–1331, 2017.

[53] Adams, D. H., Popma, J. J., Reardon, M. J., Yakubov, S. J., Coselli, J. S., Deeb, G. M., Gleason, T. G., Buchbinder, M., Hermiller Jr, J., Kleiman, N. S., et al. Transcatheter aortic-valve replacement with a self-expanding prosthesis. *New England Journal of Medicine*, 370(19):1790–1798, 2014.

[54] Mack, M. J., Leon, M. B., Thourani, V. H., Makkar, R., Kodali, S. K., Russo, M., Kapadia, S. R., Malaisrie, S. C., Cohen, D. J., Pibarot, P., et al. Transcatheter aortic-valve replacement with a balloon-expandable valve in low-risk patients. *New England Journal of Medicine*, 380(18):1695–1705, 2019.

[55] Popma, J. J., Deeb, G. M., Yakubov, S. J., Mumtaz, M., Gada, H., O'Hair, D., Bajwa, T., Heiser, J. C., Merhi, W., Kleiman, N. S., et al. Transcatheter aortic-valve replacement with a self-expanding valve in low-risk patients. *New England Journal of Medicine*, 380(18):1706–1715, 2019.

[56] Trautner, B. W. and Darouiche, R. O. Catheter-associated infections: pathogenesis affects prevention. *Archives of internal medicine*, 164(8):842–850, 2004.

[57] Goldfarb, N. J. Medicinal injector., November 28 1905. US Patent 805,851.

[58] Tibone, J. J. Catheter, August 19 1958. US Patent 2,847,997.

[59] Kennedy, J. A. Process of rubberizing tubing, May 1 1934. US Patent 1,956,722.

[60] Eugene, B. L. Method of making hair curling tube, February 16 1960. US

Patent 2,925,021.

[61] Daniel, S. Medical probing instrument having flexible, extrudable tubing adapted to be extraverted under pressure into a body cavity, February 2 1965. US Patent 3,168,092.

[62] Silverman, D. Medical instrument for everting a thinwalled flexible tubing, April 14 1970. US Patent 3,506,011.

[63] Cox, C. E., Hinman Jr, F., and Harautuneian, A. Medical instrument with outrolling catheter, June 8 1971. US Patent 3,583,391.

[64] Silverman, D. Method and apparatus for placing in and retrieving a tubular probe from a body cavity, March 24 1970. US Patent 3,502,069.

[65] Silverman, D. Medical probe adapted to be everted under pressure and method, March 17 1970. US Patent 3,500,819.

[66] Lowery, G. R., Bacich, S. R., and Tholin, K. Apparatus and method for independent movement of an instrument within a linear catheter, April 5 1994. US Patent 5,300,023.

[67] Lowery, G. R., Bacich, S. R., and Tholin, K. Method of tubal recanalization and catheter system therefor, November 15 1994. US Patent 5,364,345.

[68] Schickling, D. P., Lowery, G. R., Bacich, S. R., Ciulei, D. M., and Woker, G. Linear eversion catheter with reinforced inner body extension, December 15 1992. US Patent 5,171,305.

[69] Fogarty, T. J. and Chin, A. K. Dilation catheter method and apparatus, June 9 1981. US Patent 4,271,839.

[70] Masuda, S. Method and apparatus for passing an article through an interior of a pipe, March 7 1978. US Patent 4,077,610.

[71] Minteer, W. B. Extroversive catheter, July 25 1967. US Patent 3,332,424.

[72] Viek, N. F. Catheter, September 30 1975. US Patent 3,908,663.

[73] Shook, D. R. Toposcopic catheter and method of fabrication, August 5 1986. US Patent 4,604,094.

[74] Zeimer, H. S. and Simkin, A. Evertable, extendible probe, August 25 1970. US Patent 3,525,329.

[75] Goldstein, S. R. and Jones, R. Method and apparatus for traversing blood vessels, July 23 1985. US Patent 4,530,698.

[76] Shook, D., Doppman, J., Cattau Jr, E., and Goldstein, S. Everting (toposcopic) catheter for broad clinical application. 1986.

[77] Trivedi, D., Rahn, C. D., Kier, W. M., and Walker, I. D. Soft robotics: Biological inspiration, state of the art, and future research. *Applied bionics*

and biomechanics, 5(3):99–117, 2008.

[78] Pfeifer, R., Marques, H. G., and Iida, F. Soft robotics: the next generation of intelligent machines. 2013.

[79] Lipson, H. Challenges and opportunities for design, simulation, and fabrication of soft robots. *Soft Robotics*, 1(1):21–27, 2014.

[80] Walker, I. D., Dawson, D. M., Flash, T., Grasso, F. W., Hanlon, R. T., Hochner, B., Kier, W. M., Pagano, C. C., Rahn, C. D., and Zhang, Q. M. Continuum robot arms inspired by cephalopods. In *Unmanned Ground Vehicle Technology VII*, volume 5804, pages 303–314. SPIE, 2005.

[81] Laschi, C., Cianchetti, M., Mazzolai, B., Margheri, L., Follador, M., and Dario, P. Soft robot arm inspired by the octopus. *Advanced robotics*, 26(7): 709–727, 2012.

[82] Lin, H.-T., Leisk, G. G., and Trimmer, B. Goqbot: a caterpillar-inspired soft-bodied rolling robot. *Bioinspiration & biomimetics*, 6(2):026007, 2011.

[83] Wu, S., Hong, Y., Zhao, Y., Yin, J., and Zhu, Y. Caterpillar-inspired soft crawling robot with distributed programmable thermal actuation. *Science Advances*, 9(12):eadf8014, 2023.

[84] Hannan, M. W. and Walker, I. D. Analysis and experiments with an elephant's trunk robot. *Advanced robotics*, 15(8):847–858, 2001.

[85] Hannan, M. W. and Walker, I. D. Kinematics and the implementation of an elephant's trunk manipulator and other continuum style robots. *Journal of robotic systems*, 20(2):45–63, 2003.

[86] Al Harthy, S., Sadati, H., Girerd, C., Kim, S., Wu, Z., Saldarriaga, B., Seneci, C., Morimoto, T., and Bergeles, C. Tip-growing robots: Design, theory, application. *IEEE TRANSACTIONS ON ROBOTICS*, 2024.

[87] Oyejide, A. J., Stroppa, F., and Saraç, M. Miniaturized soft growing robots for minimally invasive surgeries: challenges and opportunities. *Progress in Biomedical Engineering*, 2025.

[88] Suulker, C., Mack, T., Distefano, G., Ho Chan, C., Zhang, K., Sadati, S. H., Mecozzi, L., Sulaiman, S., Adhnan Thaha, M., Ficuciello, F., et al. State of the art in soft eversion robots for colonoscopy: a review. *Progress in Biomedical Engineering*, 8(1):012012, 2026.

[89] Abrar, T., Putzu, F., Ataka, A., Godaba, H., and Althoefer, K. Highly manoeuvrable eversion robot based on fusion of function with structure. In *2021 IEEE International Conference on Robotics and Automation (ICRA)*, pages 12089–12096. IEEE, 2021.

[90] Putzu, F., Abrar, T., Konstantinova, J., and Althoefer, K. Minimally invasive surgery eversion overtube. *Genoa, Italy*, 9:2, 2019.

[91] El-Hussieny, H., Jeong, S.-G., and Ryu, J.-H. Dynamic modeling of a class of soft growing robots using euler-lagrange formalism. *Society of Instrument and Control Engineers*, pages 453–458, 2019.

[92] Ataka, A., Abrar, T., Putzu, F., Godaba, H., and Althoefer, K. Model-based pose control of inflatable eversion robot with variable stiffness. *IEEE Robotics and Automation Letters*, 5(2):3398–3405, 2020.

[93] Blumenschein, L. H., Koehler, M., Usevitch, N. S., Hawkes, E. W., Rucker, D. C., and Okamura, A. M. Geometric solutions for general actuator routing on inflated-beam soft growing robots. *IEEE Transactions on Robotics*, 38 (3):1820–1840, 2021.

[94] Greer, J. D., Blumenschein, L. H., Okamura, A. M., and Hawkes, E. W. Obstacle-aided navigation of a soft growing robot. In *2018 IEEE International Conference on Robotics and Automation (ICRA)*, pages 4165–4172. IEEE, 2018.

[95] Greer, J. D., Blumenschein, L. H., Alterovitz, R., Hawkes, E. W., and Okamura, A. M. Robust navigation of a soft growing robot by exploiting contact with the environment. *The International Journal of Robotics Research*, 39 (14):1724–1738, 2020.

[96] Blumenschein, L. H., Okamura, A. M., and Hawkes, E. W. Modeling of bioinspired apical extension in a soft robot. In *Conference on Biomimetic and Biohybrid Systems*, pages 522–531. Springer, 2017.

[97] Haggerty, D. A., Naclerio, N. D., and Hawkes, E. W. Characterizing environmental interactions for soft growing robots. In *2019 IEEE/RSJ International Conference on Intelligent Robots and Systems (IROS)*, pages 3335–3342. IEEE, 2019.

[98] Przybylski, F., Adagolodjo, Y., CERRUTI, G., DEQUIDT, J., DURIEZ, C., BERTHET-RAYNE, P., et al. 3d kinematics and quasi-statics of a growing robot eversion. In *2023 IEEE International Conference on Soft Robotics (RoboSoft)*, pages 1–6. IEEE, 2023.

[99] Pai, D. K. Strands: Interactive simulation of thin solids using cosserat models. In *Computer graphics forum*, volume 21, pages 347–352. Wiley Online Library, 2002.

[100] Spillmann, J. and Teschner, M. Corde: Cosserat rod elements for the

dynamic simulation of one-dimensional elastic objects. In *Proceedings of the 2007 ACM SIGGRAPH/Eurographics symposium on Computer animation*, pages 63–72, 2007.

[101] Rucker, D. C., Jones, B. A., and Webster III, R. J. A geometrically exact model for externally loaded concentric-tube continuum robots. *IEEE transactions on robotics*, 26(5):769–780, 2010.

[102] Trivedi, D., Lotfi, A., and Rahn, C. D. Geometrically exact models for soft robotic manipulators. *IEEE Transactions on Robotics*, 24(4):773–780, 2008.

[103] Renda, F., Armanini, C., Lebastard, V., Candelier, F., and Boyer, F. A geometric variable-strain approach for static modeling of soft manipulators with tendon and fluidic actuation. *IEEE Robotics and Automation Letters*, 5(3):4006–4013, 2020.

[104] Renda, F., Cacucciolo, V., Dias, J., and Seneviratne, L. Discrete cosserat approach for soft robot dynamics: A new piece-wise constant strain model with torsion and shears. In *2016 IEEE/RSJ International Conference on Intelligent Robots and Systems (IROS)*, pages 5495–5502. IEEE, 2016.

[105] Cao, D., Liu, D., and Wang, C. H.-T. Three-dimensional nonlinear dynamics of slender structures: Cosserat rod element approach. *International Journal of Solids and Structures*, 43(3-4):760–783, 2006.

[106] Abdelal, G. F., Abuelfoutouh, N., and Gad, A. H. *Finite element analysis for satellite structures: applications to their design, manufacture and testing*. Springer Science & Business Media, 2012.

[107] Abdullah, S., Al-Asady, N., Ariffin, A., and Rahman, M. A review on finite element analysis approaches in durability assessment of automotive components. *Journal of Applied Sciences*, 8(12):2192–2201, 2008.

[108] Zienkiewicz, O. C. and Taylor, R. L. *The finite element method for solid and structural mechanics*. Elsevier, 2005.

[109] Jagota, V., Sethi, A. P. S., and Kumar, K. Finite element method: an overview. *Walailak Journal of Science and Technology (WJST)*, 10(1):1–8, 2013.

[110] Adagolodjo, Y., Renda, F., and Duriez, C. Coupling numerical deformable models in global and reduced coordinates for the simulation of the direct and the inverse kinematics of soft robots. *IEEE Robotics and Automation Letters*, 6(2):3910–3917, 2021.

[111] Coevoet, E., Morales-Bieze, T., Largilliere, F., Zhang, Z., Thieffry, M.,

Sanz-Lopez, M., Carrez, B., Marchal, D., Goury, O., Dequidt, J., et al. Software toolkit for modeling, simulation, and control of soft robots. *Advanced Robotics*, 31(22):1208–1224, 2017.

[112] Comas, O. *Real-time soft tissue modelling on GPU for medical simulation*. PhD thesis, Université des Sciences et Technologie de Lille-Lille I, 2010.

[113] Comas, O., Cotin, S., and Duriez, C. A shell model for real-time simulation of intra-ocular implant deployment. In *International Symposium on Biomedical Simulation*, pages 160–170. Springer, 2010.

[114] Golembiovskỳ, T. and Duriez, C. Bézier shell finite element for interactive surgical simulation. In *VRIPHYS 12: 9th Workshop on Virtual Reality Interactions and Physical Simulations*, pages 107–116. Eurographics Association, 2012.

[115] Yuan, C. S., Hassan, A., Ghazali, M. I. H., and Ismail, A. F. Heat sealability of laminated films with lldpe and ldpe as the sealant materials in bar sealing application. *Journal of Applied Polymer Science*, 104(6):3736–3745, 2007.

[116] Kalogeropoulos, A. S., Redwood, S. R., Allen, C. J., Hurrell, H., Chehab, O., Rajani, R., Prendergast, B., and Patterson, T. A 20-year journey in transcatheter aortic valve implantation: evolution to current eminence. *Frontiers in cardiovascular medicine*, 9:971762, 2022.

[117] U.S. Food and Drug Administration. P160043: Resolute onyx™ zotarolimus-eluting coronary stent system – summary of safety and effectiveness data (ssed). `https://www.accessdata.fda.gov/cdrh_docs/pdf16/P160043C.pdf`, 2017.

[118] Boston Scientific Corporation. Promus elite® everolimus-eluting platinum chromium coronary stent system – product specifications (eu). `https://www.bostonscientific.com/content/dam/bostonscientific/Interventional%20Cardiology/portfolio-group/Stents/promus-elite/library/IC-533403-AA%20Promus%20ELITE%20Spec%20Sheet_EU_FINAL.pdf`, 2020.

[119] Corporation, B. S. Synergy™ product spec sheet – balloon-expandable stent system: Nominal inflation pressure / rated burst pressure. `https://www.bostonscientific.com/content/dam/bostonscientific/Interventional%20Cardiology/portfolio-group/Stents/Synergy/resource-center/SYNERGY-Product-Spec-Sheet.pdf`, 2015.

[120] Fajardo, B. S., Seneci, C., Sadati, H., Wu, Z., Rhode, K., and Bergeles, C. Co2 laser welding of low-density polyethylene for soft linear eversion robot fabrication. In *IEEE 20th International Conference on Automation Science and Engineering (CASE)*, 2024.

[121] Zhang, D., Wang, X., Tian, M., Shen, D., and Mao, Y. A novel manufacturing method for thermoplastic polyurethane welding using co2 laser. In *2019 IEEE International Conference on Mechatronics and Automation (ICMA)*, pages 1687–1691. IEEE, 2019.

[122] Siau, K., Hayee, B., and Gayam, S. Endoscopy's current carbon footprint. *Techniques and Innovations in Gastrointestinal Endoscopy*, 23(4): 344–352, 2021. ISSN 2590-0307. doi: https://doi.org/10.1016/j.tige.2021.06.005. URL `https://www.sciencedirect.com/science/article/pii/S259003072100043X`. Green Endoscopy.

[123] Peery, A. F., Crockett, S. D., Murphy, C. C., Lund, J. L., Dellon, E. S., Williams, J. L., Jensen, E. T., Shaheen, N. J., Barritt, A. S., Lieber, S. R., et al. Burden and cost of gastrointestinal, liver, and pancreatic diseases in the united states: update 2018. *Gastroenterology*, 156(1):254–272, 2019.

[124] Ahlawat, R., Hoilat, G. J., and Ross, A. B. Esophagogastroduodenoscopy. 2018.

[125] Ciocîrlan, M. Low-cost disposable endoscope: pros and cons. *Endoscopy International Open*, 7(09):E1184–E1186, 2019.

Appendix A

Overview of SOFA's Mechanical Architecture

The Simulation Open Framework Architecture (SOFA) provides a modular and hierarchical environment for the modeling and simulation of deformable structures. Widely used in soft robotics and biomedical applications, SOFA is designed for real-time physics computation, enabling the combination of multiple mechanical representations within a single simulation scene.

The mechanical representation of any system in SOFA is built as a graph of interconnected components, where each node contains a set of mechanical variables and their associated physical models. Each node may itself contain child nodes, forming a hierarchical scene graph where data and forces propagate throughout the structure. Three core components define the structure and behavior of this graph:

- **MechanicalObjects** store the state variables of the system—namely positions and velocities. These coordinates may be either generalized (serving directly as the system's degrees of freedom) or derived through kinematic relations.
- **Mappings** implement these kinematic relations between two `MechanicalObjects`. They convert coordinates from one space (the source) to another (the target) according to a defined geometric model. Forces are propagated

in the opposite direction, ensuring consistent mechanical coupling between the two representations.

- **ForceFields** define the constitutive laws that link the primal variables (position, velocity) to their dual quantities (forces). They determine the local mechanical response of each component to external or internal loading.
- **Solvers and Constraints** are responsible for assembling and resolving the system equations. Linear, nonlinear, and time integrators are available, often combined with constraint solvers (e.g., Lagrange multipliers, penalties) to enforce physical conditions such as fixed boundaries, joints, or contacts.
- **VisualModels** manage the graphical representation of the simulated object. They are typically mapped to the mechanical layer to follow its deformation, allowing a separation between physical computation and rendering.
- **CollisionModels** define the geometric primitives used for detecting contacts or intersections between deformable or rigid bodies. These models are often simpler than the visual meshes to optimize detection efficiency.
- **Contact and Response** components handle the physical consequences of collisions, computing contact constraints, penalties, or frictional responses that modify the system's equations of motion accordingly.

Through the combination of these elements, SOFA enables the construction of hierarchical mechanical systems that couple multiple physical representations—rigid, flexible, or continuum—within a unified computational framework. This hierarchical organization facilitates the definition of hybrid models, such as the "Fiber–FEM", which reproduces the eversion behavior of the eversion-based robot.

Further details and implementation guidelines are available in the official SOFA documentation[1] and source repository[2].

[1] `https://www.sofa-framework.org/community/doc/`
[2] `https://github.com/sofa-framework`

Appendix B

Algorithms

Algorithm 1 SOFA Hierarchy – Fiber-Based Geometry

```
Controller                                              ▷ Movement of fibers
Node 'root'
  Node 'Fibers'                                         ▷ Creation of fibers
    For i = 0 to f do
      Node 'Base'
        MechanicalObject: baseMO
        FixedConstraint
      Node 'FiberCoordinate'
        MechanicalObject: coordinatesMO
        BeamHookeLawForceField
      Node 'FiberFrame'
        MechanicalObject: framesMO
        DiscreteFiberMapping          ▷ From coordinatesMO to framesMO
    End for
    Node 'FiberMappingGeneral'
      MechanicalObject: generalMO
      SubsetMultiMapping                  ▷ From framesMO to generalMO
      UniformMass
      Node 'OriginalMesh'
        MechanicalObject: generalMOTransfo
        MeshTopology
        IdentityMapping             ▷ From generalMO to generalMOTransfo
```

Algorithm 2 SOFA Hierarchy – FEM Layer on Fiber-Based Geometry

```
Controller                                          ▷ Movement of mesh
Node 'root'
  Node 'Fibers'                  ▷ Fiber-based geometry (cf. Algorithm 1)
    ...
    Node 'FiberMappingGeneral'
      ...
      Node 'OriginalMesh'
        MechanicalObject: generalMOTransfo
        MeshTopology
        IdentityMapping          ▷ From generalMO to generalMOTransfo

  Node 'MeshSurfacic'                ▷ FEM on the fiber-based geometry
    Node 'Solvers'
      EulerImplicitSolver
      SparseLDLSolver
      GenericConstraintCorrection
    Node 'FEMMesh'
      MechanicalObject: femMO
      MeshTopology
      RestShapeSpringsForceField
      TriangleFEMForceField
      SurfacePressureConstraint
      TriangleCollisionModel
      LineCollisionModel
      PointCollisionModel
```

Algorithm 3 SOFA Hierarchy – Shell Model

Node 'root'
  Node 'Fibers' ▷ Fiber-based geometry (cf. Algorithm 1) - Initialization only
    ...
  Node 'Shell' ▷ Creation of Shell mesh
    Node 'Solvers'
      `EulerImplicitSolver`
      `SparseLDLSolver`
      `GenericConstraintCorrection`
    Node 'ShellMesh'
      `MechanicalObject`: *shellMO*
      `MeshTopology`
      `TriangleShellForceField`
      `FixedConstraint`
        Node 'PressureMesh'
          `MeshTopology`
          `MechanicalObject`: *shellMOTransfo*
          `SurfacePressureConstraint`
          `TriangleCollisionModel`
          `LineCollisionModel`
          `PointCollisionModel`
          `IdentityMapping` ▷ From *shellMO* to *shellMOTransfo*

Algorithm 4 SOFA Hierarchy – Guide

```
Controller                                              ▷ Movement of mesh
Node 'root'
  Node 'Fibers'   ▷ Fiber-based geometry (cf. Algorithm 1) - Initialization only
    ...
  Node 'Shell'
    ArrowObject                                         ▷ Everted Zone
    ArrowObject                                         ▷ Storage Zone
    Node 'Solvers'
      ...
    Node 'EvenGuide'                  ▷ Guide Hierarchy (cf. Algorithm 5)
    ...
    Node 'OddGuide'                   ▷ Same as EvenGuide for odd i
    ...
    Node 'ShellMesh'
      MechanicalObject: shellMO
      ...
      For i = 0 to f do
        Node 'Attachment'
          MechanicalObject: attachmentMO
          RestShapeSpringsForceField
          SubsetMapping               ▷ From shellMO to attachmentMO
      End For
      Node 'PressureMesh'
        ...
```

Algorithm 5 SOFA Hierarchy – Guide w/ focus on EvenGuide

`Controller` ▷ Movement of mesh
Node 'root'
Node 'Fibers' ▷ Fiber-based geometry (cf. Algorithm 1) - Initialization only
...
Node 'Shell'
...
Node 'Solvers'
...
Node 'EvenGuide'
`MechanicalObject`: *baseGuideMO*
Node 'GuideCoordinate'
`MechanicalObject`: *coordinatesGuideMO*
`BeamHookeLawForceField`
Node 'GuideFrame'
`MechanicalObject`: *framesGuideMO*
`DiscreteGuideMapping` ▷ From *coordinatesGuideMO* to *framesGuideMO*
Node 'EvenSubGuide'
For $i = 0$ to f **do**
If $i \bmod 2 = 0$ **then**
Node 'EvenSubGuideBase'
`MechanicalObject`: *baseSubGuideMO*
`RestShapeSpringsForceField`
Node 'SubGuideFrame'
`MechanicalObject`: *framesSubGuideMO*
`DiscreteSubGuideMapping` ▷ From *baseSubGuideMO* to *framesSubGuideMO*
Node 'OrientedSubGuide'
`MechanicalObject`: *orientedSubGuideMO*
`RigidMapping` ▷ From *framesSubGuideMO* to *orientedSubGuideMO*
Node 'SubGuideCoordinate'
`MechanicalObject`: *coordinatesSubGuideMO*
`BeamHookLawForceField`
End For
Node 'OddGuide' ▷ Same as *EvenGuide* for odd i
...
Node 'ShellMesh'
...
Node 'Attachment'
...
Node 'PressureMesh'
...

Appendix C

Bariatric Applications: Supplementary Studies

In parallel with the endovascular work presented in the previous chapters, this chapter gathers complementary exploratory studies. The objective was to preliminarily assess to what extent the robotic platform designed around the eversion principle could be adapted to another clinical context — that of bariatric endoscopy. This is therefore not a direct transposition of the TAVI procedure, which relies on saline pressurization and addresses specific vascular constraints, but rather a parallel study aimed at testing the versatility of the concept and identifying common challenges (miniaturization, material selection, embedded monitoring) from a different perspective.

In the United States, approximately 6 million gastroscopies are performed each year [122, 123]. The procedure consists in introducing a flexible endoscope through the mouth, advancing through the esophagus and stomach while insufflating air or CO_2 to distend the lumen, and then directly inspecting the mucosa. The device, generally 10 to 14 mm in diameter, is equipped with a high-definition camera and an operating channel allowing the insertion of instruments such as a biopsy forceps. This forceps is used both for tissue sampling and for manipulating or removing local structures, and thus constitutes an essential tool in endoscopic practice.

Although considered a safe and routine procedure, gastroscopy is not without

constraints. It often causes discomfort related to the passage of the endoscope, which can trigger a gag reflex. For this reason, most procedures are performed under conscious sedation, which reduces discomfort but requires continuous monitoring, additional recovery time, and specific drug administration. In some cases, general anesthesia may be necessary, particularly during complex therapeutic procedures. More rarely, complications may occur, such as bleeding, perforation of the digestive wall, or infection [124]. Moreover, these clinical constraints are compounded by a significant economic burden: the purchase cost of a standard flexible gastroscope is estimated between 20,000 and 40,000 USD, while each procedure entails an additional cost of 140 to 280 USD for reprocessing, along with frequent maintenance and repair expenses [125].

In this context, the eversion-based robot aims to reproduce the essential functions of an endoscope, visual inspection, tool insertion via a forceps, and tracking of progression, while offering several advantages. Its eversion-based progression limits friction against the walls and could therefore reduce the risk of mucosal trauma. Its simpler architecture may also lower manufacturing and maintenance costs compared to conventional endoscopes requiring extensive reprocessing. Finally, the possibility of integrating embedded monitoring functions (internal pressure sensing, eversion tracking) opens the way to enhanced traceability during navigation.

C.1 Design and Preliminary Tests

In the bariatric context, the development of an eversion-based robot requires navigation without exceeding an external diameter of 15 mm. This value, derived from endoscopic recommendations for adults, constitutes a major clinical constraint: it determines the tolerability of passage through the digestive tract and defines the dimensional limit beyond which the risk of trauma or discomfort becomes too high.

To explore this feasibility, a first complete robot prototype was built in LDPE, with a reduced diameter of 15 mm. LDPE was chosen for its flexibility and ease of forming. A 14 mm support capsule was integrated at the robot's tip to host a high-definition 1080p endoscopic camera with LED lighting (*B0B76QWFY9*, IL-

IHOME) and 2.8 mm biopsy forceps (*Radial Jaw 4*, Boston Scientific). These instruments, representative of dimensions commonly used in gastroscopy, provided a realistic first test of the functional compatibility between an eversion-based mechanism and the essential actions of an endoscope — mucosal visualization and simple biopsy sampling. However, the narrow margin between the capsule (14 mm) and the clinical limit (15 mm) illustrates the major challenge of miniaturization and integration inherent in this approach.

deployment tests were conducted at an eversion pressure of approximately 1 bar, over a deployment length close to one meter, using air pressurization. This choice stems from the clinical context: unlike the endovascular (TAVI) application, where a liquid is required to prevent any risk of embolism, digestive endoscopy allows the use of air without danger in the event of leakage, especially since air is already the fluid routinely used for insufflation during gastroscopy. The use of air also has the advantage of improving the system's compliance compared to a liquid, which would bring no benefit in this setting. This difference highlights that, although based on the same eversion principle, the adaptation of the robot to the bariatric context entails specific operating conditions distinct from those of the endovascular application.

The first tests, however, revealed several limitations (Figure C.1). The sealing of the custom-made LDPE tube, produced by thermal fusion, proved fragile, with ruptures occurring at the welds after only about 10 cm of deployment. A single test could be performed: the camera and forceps functioned, although the image sharpness was partially reduced due to the capsule, which left a portion of the plastic visible within the field of view. The simultaneous integration of these two instruments also increased internal friction, compromising the smoothness of deployment and creating a risk of tearing the plastic wall. Finally, maneuverability was limited by the use of a rudimentary pressurization box, whose main drawback was poor ergonomics, making handling uncomfortable for the operator.

These results, although encouraging in terms of feasibility, showed that LDPE is not suitable for clinical translation. The choice of this material was initially motivated by its availability and ease of shaping at the time of the first trials, before the option of TPU was considered. However, the fragility of the welds and the lack of biocompatibility certification make it necessary to turn toward more

appropriate materials. In the continuation of this work (Section 5.1.2), attention was directed toward TPU, whose forming and preforming processes were experimentally and numerically mastered, and which offers the advantage of recognized biocompatibility. In parallel, the deployment system was redesigned to improve operator experience: the rudimentary box was replaced by an ergonomic manual device, providing more intuitive and comfortable handling. These two developments, adoption of TPU and improvement of the deployment system, represent essential steps toward a bariatric robot truly compatible with the constraints of miniaturization and clinical safety.

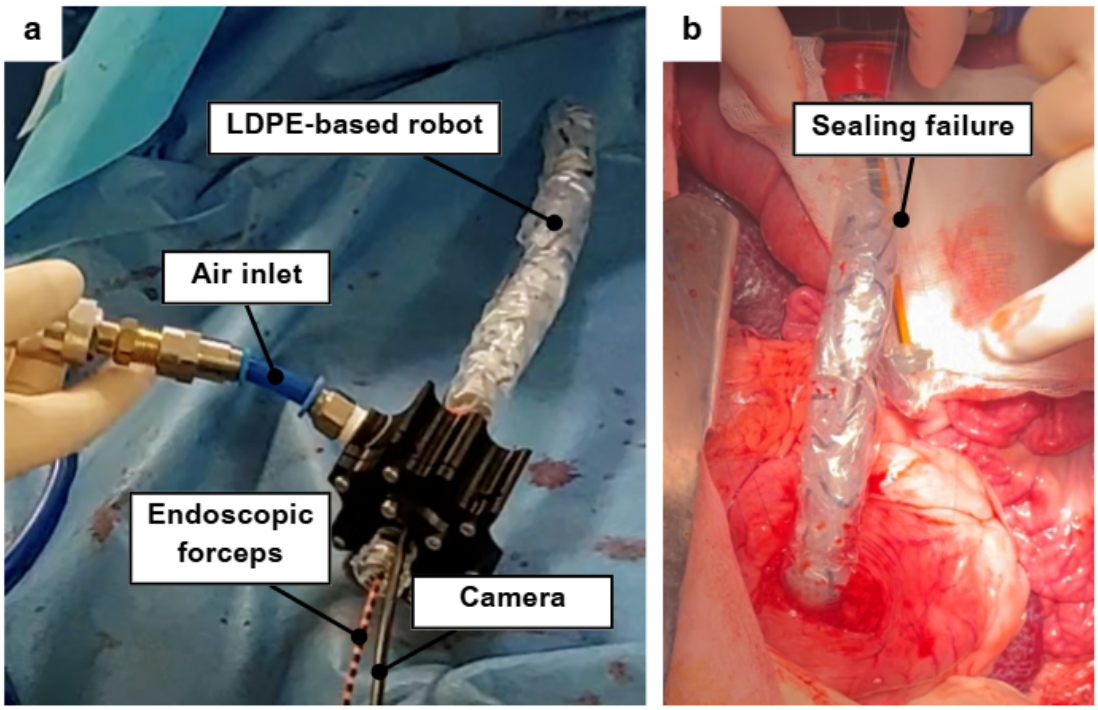


Figure C.1: (a) First prototype of a 15 mm LDPE eversion-based robot equipped with a support capsule integrating an endoscopic camera and biopsy forceps, with air inlet connected to the pressurization box. (b) Sealing failure observed during the test, with rupture occurring at the welded edges after approximately 10 cm of deployment.

C.2 Embedded Capsule

One of the main challenges identified during the initial bariatric trials concerned the absence of objective feedback on the internal state of the robot during de-

ployment. Traditional flexible endoscopes provide continuous visualization of the digestive mucosa and an approximate indication of progression using length markers, but they offer no data on the mechanical stresses exerted or on the local pressures applied to the walls. However, in the case of an eversion-based robot operating by eversion—where deployment depends on internal pressurization and close contact with the mucosa—the absence of such information increases the risk of overpressure, misdirection, or instability.

To address this need, an embedded electronic capsule was developed (Figure C.2). Its purpose was to complement optical vision with real-time monitoring of critical parameters: internal pressure to prevent excess, motion tracking for stability assessment, and eversion detection through markers. The clinical objective here was to endow the eversion-based robot with a level of traceability and safety.

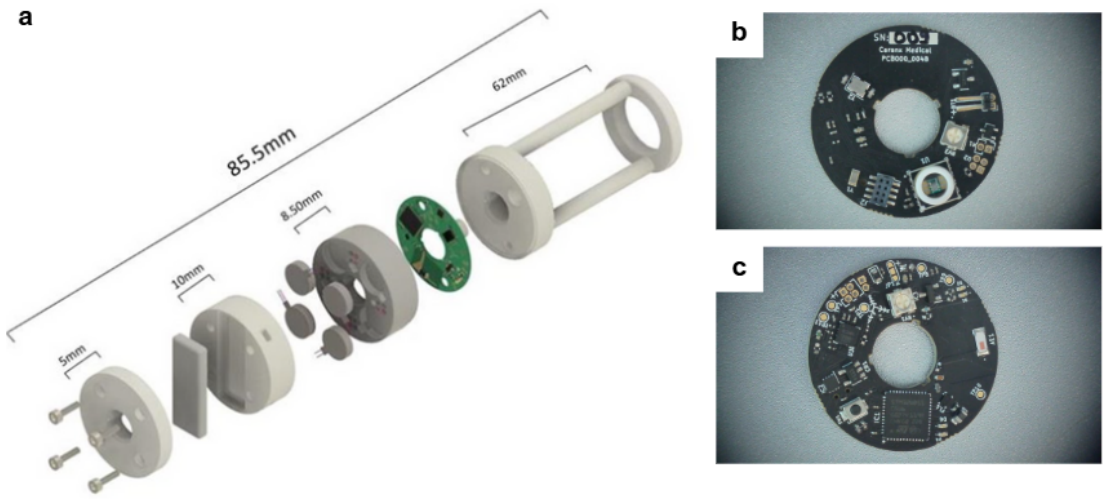


Figure C.2: Prototype of the embedded electronic capsule integrating sensing, communication, and control electronics: (a) complete capsule, (b) upper side of the PCB, and (c) lower side of the PCB.

The capsule integrated a multilayer printed circuit board, a low-power Bluetooth microcontroller, a pressure sensor to monitor pressurization, an accelerometer-gyroscope to measure motion, and an infrared sensor designed to detect eversion markers positioned along the robot. A miniaturized antenna ensured connectivity, and a LiPo battery provided power. A micro vibrating motor was also included to generate local oscillations, following the approach previously tested in the endovascular context (Section 5.1.1), to reduce friction and facilitate deployment.

Validation tests confirmed the feasibility of this concept: the pressure measurement showed a sensitivity of about 700 mV/bar, validated by comparison with a reference sensor; Bluetooth transmission remained stable over several hours of continuous acquisition; and the motor could be activated remotely via a user interface. However, several important limitations remain. Eversion marker detection proved incomplete, as the infrared signal was sensitive to alignment and optical interference. Energy autonomy was limited, since the battery occupied a disproportionate volume relative to the 15 mm clinical constraint. Finally, the wireless communication did not yet include security protocols, exposing the system to interference risks in a hospital environment.

Another limitation was the visual presence of plastic within the camera's field of view, which reduced image clarity. To overcome this issue, a storage zone of approximately 60 mm was created inside the capsule, following a principle similar to the scrunch method [35]. This compromise allowed the material to be locally folded, clearing the view for the camera and enabling a clearer observation of the mucosa. Although space-consuming, this strategy illustrates the need to integrate optical constraints early in the mechanical design of the robot.

In its current state, this capsule remains an exploratory proof of concept: with a diameter of 20 mm, it is still too large for safe esophageal insertion. The main challenge lies in miniaturization, particularly of the battery and antenna, which impose significant spatial constraints. Future size reduction could be achieved through the use of flexible circuits, low-power components, and more integrated packaging strategies. Another complementary direction would be to reduce the functional load of the capsule itself: some measurements, such as deformation or position tracking, could be transferred to sensors directly integrated onto the robot's membrane using printed conductive inks. By redistributing monitoring functions in this way, it would become possible to reduce the number of components embedded in the capsule, refine its design, and move closer to the dimensional constraints imposed by clinical practice.

C.3 Conductive Inks

Given the miniaturization limits of the capsule, a complementary strategy was considered: transferring part of the monitoring functions directly onto the robot's membrane. The idea was not to concentrate all sensors inside the capsule but to distribute certain measurements (local pressure, deformations, eversion tracking) along the robot's body through printed electronics.

Conductive inks deposited on polymer membranes make it possible to transform the wall into a functional surface without rigidifying the structure. This approach aims to achieve two clinical benefits: reducing the capsule's footprint to meet the 15 mm constraint and providing distributed monitoring.

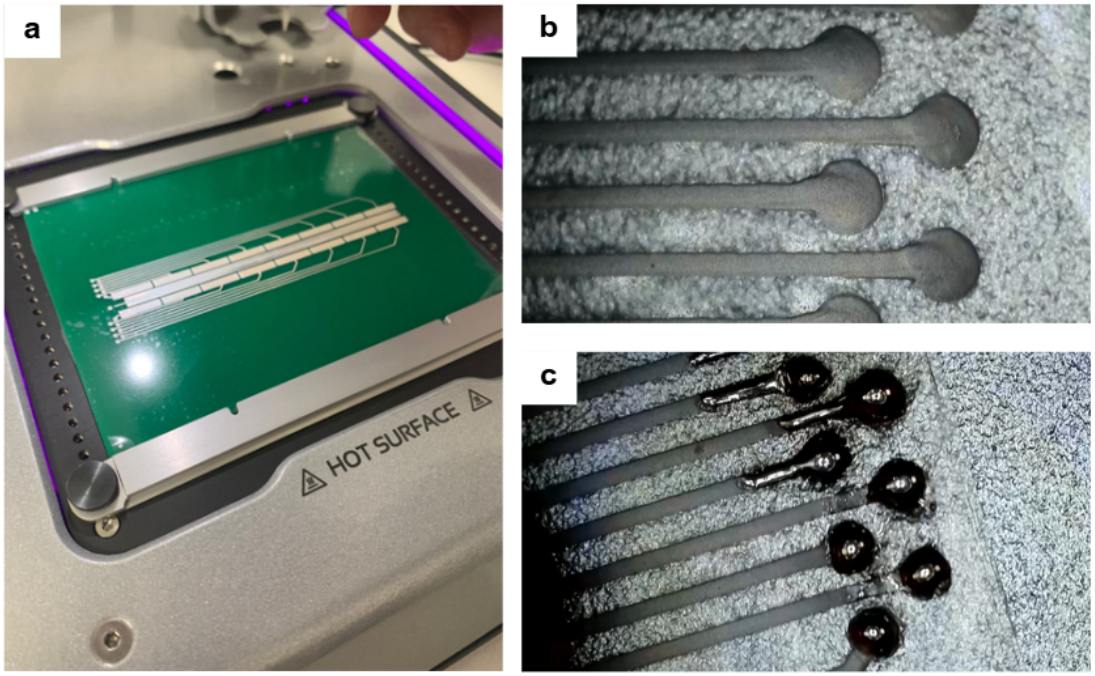


Figure C.3: Conductive patterns printed on a Pellethane substrate using the Voltera V-One printer and SEFlex conductive ink. (a) Plastic film positioned on the Voltera printing platform, (b) microscopic view of the SEFlex ink deposited on the TPU surface, and (c) final printed track demonstrating the good solderability of the ink with tin.

Printing was carried out using a *Voltera V-One* printer, capable of precisely depositing conductive inks on flexible substrates (Figure C.3). The selected substrate was an elastic polyurethane with a thickness of 25.4 μm (*MT-2001*

Polyether Polyurethane, American PolyFilm), chosen for its flexibility, printability, and potential medical use. Three formulations of inks supplied by VFP Ink Technologies were tested: SESC (Silver Epoxy Standard Conductive), SEFlex (Silver Epoxy Flexible), and CEL Carbon.

Electrical characterization showed that silver-based inks offered good conductivity and encouraging mechanical stability. The SEFlex ink exhibited the best performance, with a resistance of approximately 2.6 Ω after curing and maintained integrity after several dozen bending and winding cycles. The SESC ink, although conductive ($\approx$ 3.6 Ω), was more prone to microcrack formation. The carbon-based ink, with a resistivity on the order of 43 kΩ, proved unsuitable.

From a clinical perspective, these values demonstrate that silver traces are capable of transmitting usable signals for simple sensors (pressure, contact), but their durability remains limited: a gradual loss of conductivity appears after a few dozen cycles, whereas an endoscopic procedure would require at least several hundred stable cycles to ensure reliability.

Overall, this work paves the way for realistic integration of conductive traces directly onto TPU membranes. It suggests that printed electronics could take over part of the distributed monitoring functions (pressure, deformation, eversion distance), thus reducing reliance on a bulky electronic capsule. However, durability under repeated eversion and compatibility with a real digestive environment (humidity, acidity, cleaning) remain major challenges. Strategies such as serpentine pattern designs, protective coatings, or more robust ink formulations will need to be explored to validate this approach under clinical conditions.

C.4 Conclusion

The work presented in this chapter explored, in a preliminary manner, the adaptation of the eversion-based robot to the context of bariatric endoscopy. The initial LDPE prototype made it possible to verify the feasibility of reducing the diameter to 15 mm and integrating standard tools such as a camera and biopsy forceps. However, the early rupture of the welds confirmed the limitations of this material and of the assembly technique used, emphasizing the need for more suit-

able and biocompatible materials such as TPU, which was studied in the previous chapters.

In addition, the development of an electronic capsule demonstrated the feasibility of real-time monitoring through the integration of pressure and motion sensors combined with wireless transmission. This approach addresses a recognized need in digestive endoscopy, where the absence of objective feedback increases the risk of complications. However, the current size of the capsule (20 mm) remains a major constraint, calling for further miniaturization efforts.

To overcome this limitation, the use of conductive inks printed directly on the membrane was considered to transfer part of the monitoring functions onto the robot's wall. The first results obtained on TPU confirm the compatibility of this approach with flexible substrates, while highlighting the need to improve the durability of the printed traces under repeated eversion cycles.

Taken together, these studies should not be regarded as independent contributions, but rather as complementary steps oriented toward a common objective. The analysis of the first prototype's failures informs the choice of materials and fabrication processes; the electronic capsule demonstrates the relevance of embedded feedback; and the exploration of conductive inks offers a crucial path toward miniaturization compatible with anatomical constraints.

These results remain exploratory, but they open promising perspectives for specific bariatric applications, including less invasive postoperative exploration, detection of local complications, and integration of distributed physiological sensors along the digestive tract.

Appendix D

Copyright Permissions

D.1 Authorization to re-use Figure 2.5

CCC Marketplace

Order Number: 1658677
Order Date: 04 Oct 2025

Payment Information

Flavie PRZYBYLSKI
flavie.przybylski@caranx-medical.com
Payment method: Invoice

Billing Address:
Flavie PRZYBYLSKI
400 promenade des anglais
Nice
France

+33 0640380484
flavie.przybylski@caranx-medical.com

Customer Location:
Flavie PRZYBYLSKI
400 promenade des anglais
Nice
France

Order Details

1. Journal of biomechanical engineering

Billing Status: Open

Article: A miniature toposcopic catheter suitable for small diameter tortuous blood vessels.

Order License ID	1658677-1	**Type of Use**	Republish in a thesis/dissertation
Order detail status	Completed	**Publisher**	A S M E INTERNATIONAL
ISSN	1528-8951	**Portion**	Image/photo/illustration

0,00 EUR
Republication Permission

LICENSED CONTENT

Publication Title	Journal of biomechanical engineering	**Rightsholder**	American Society of Mechanical Engineers ASME
Article Title	A miniature toposcopic catheter suitable for small diameter tortuous blood vessels.	**Publication Type**	e-Journal
		Start Page	221
		Issue	3
Author / Editor	American Society of Mechanical Engineers.	**Volume**	102
		URL	http://biomechanical.asmedigitalcollection.asme.org/journal.aspx
Date	01/01/1977		
Language	English		
Country	United States of America		

REQUEST DETAILS

Portion Type	Image/photo/illustration	**Distribution**	Worldwide
Number of Images / Photos / Illustrations	1	**Translation**	Original language of publication
Format (select all that apply)	Electronic	**Copies for the Disabled?**	No
		Minor Editing Privileges?	No
Who Will Republish the Content?	Publisher, not-for-profit	**Incidental Promotional Use?**	No
		Currency	EUR
Duration of Use	Life of current and all future editions		
Lifetime Unit Quantity	Up to 499		
Rights Requested	Main product		

NEW WORK DETAILS

Title	Thesis	**Institution Name**	INRIA Lille & Caranx Medical
Instructor Name	Flavie PRZYBYLSKI	**Expected Presentation Date**	2025-10-04

ADDITIONAL DETAILS

D.2 Authorization to re-use Figure 2.7

JOHN WILEY AND SONS LICENSE TERMS AND CONDITIONS

Oct 04, 2025

This Agreement between Flavie PRZYBYLSKI ("You") and John Wiley and Sons ("John Wiley and Sons") consists of your license details and the terms and conditions provided by John Wiley and Sons and Copyright Clearance Center.

License Number	6122011169328
License date	Oct 04, 2025
Licensed Content Publisher	John Wiley and Sons
Licensed Content Publication	Macromolecular Rapid Communications
Licensed Content Title	Light-Driven, Caterpillar-Inspired Miniature Inching Robot
Licensed Content Author	Hao Zeng, Owies M. Wani, Piotr Wasylczyk, et al
Licensed Content Date	May 31, 2017
Licensed Content Volume	39
Licensed Content Issue	1
Licensed Content Pages	6
Type of Use	Dissertation/Thesis
Requestor type	University/Academic
Format	Electronic
Portion	Figure/table
Number of figures/tables	1
Will you be translating?	No
Title of new work	Thesis
Institution name	INRIA Lille & Caranx Medical
Expected presentation date	Jan 2026
Portions	Figure of soft robot
The Requesting Person / Organization to Appear on the License	Flavie PRZYBYLSKI
Requestor Location	Flavie PRZYBYLSKI 400 promenade des anglais Nice, France
Publisher Tax ID	EU826007151
Total	**0.00 EUR**
Terms and Conditions	

TERMS AND CONDITIONS

This copyrighted material is owned by or exclusively licensed to John Wiley & Sons, Inc. or one of its group companies (each a"Wiley Company") or handled on behalf of a society with which a Wiley Company has exclusive publishing rights in relation to a particular work (collectively "WILEY"). By clicking "accept" in connection with completing this licensing transaction, you agree that the following terms and conditions apply to this transaction (along with the billing and payment terms and conditions established by the Copyright Clearance Center Inc., ("CCC's Billing and Payment terms and conditions"), at the time that you opened your RightsLink account (these are available at any time at http://myaccount.copyright.com).

Terms and Conditions

- The materials you have requested permission to reproduce or reuse (the "Wiley Materials") are protected by copyright.

D.3 Authorization to re-use Figure 2.7

ELSEVIER LICENSE
TERMS AND CONDITIONS

Oct 04, 2025

This Agreement between Flavie przybylski ("You") and Elsevier ("Elsevier") consists of your license details and the terms and conditions provided by Elsevier and Copyright Clearance Center.

License Number	6122011479213
License date	Oct 04, 2025
Licensed Content Publisher	Elsevier
Licensed Content Publication	Sensors and Actuators A: Physical
Licensed Content Title	A soft crawling robot driven by single twisted and coiled actuator
Licensed Content Author	Xintian Tang,Kai Li,Yingxiang Liu,Dong Zhou,Jianguo Zhao
Licensed Content Date	Jun 1, 2019
Licensed Content Volume	291
Licensed Content Issue	n/a
Licensed Content Pages	7
Start Page	80
End Page	86
Type of Use	reuse in a thesis/dissertation
Portion	figures/tables/illustrations
Number of figures/tables/illustrations	1
Format	electronic
Are you the author of this Elsevier article?	No
Will you be translating?	No
Title of new work	Thesis
Institution name	INRIA Lille & Caranx Medical
Expected presentation date	Jan 2026
Portions	Figure soft robot
The Requesting Person / Organization to Appear on the License	Flavie przybylski
Requestor Location	Flavie PRZYBYLSKI 400 promenade des anglais Nice, France
Publisher Tax ID	GB 494 6272 12
Total	**0.00 EUR**
Terms and Conditions	

INTRODUCTION

1. The publisher for this copyrighted material is Elsevier. By clicking "accept" in connection with completing this licensing transaction, you agree that the following terms and conditions apply to this transaction (along with the Billing and Payment terms and conditions established by Copyright Clearance Center, Inc. ("CCC"), at the time that you opened your RightsLink account and that are available at any time at https://myaccount.copyright.com).

GENERAL TERMS

2. Elsevier hereby grants you permission to reproduce the aforementioned material subject to the terms and conditions indicated.

D.4 Authorization to re-use Figure 2.7

ELSEVIER LICENSE
TERMS AND CONDITIONS

Oct 04, 2025

This Agreement between Flavie PRZYBYLSKI ("You") and Elsevier ("Elsevier") consists of your license details and the terms and conditions provided by Elsevier and Copyright Clearance Center.

License Number	6122020272305
License date	Oct 04, 2025
Licensed Content Publisher	Elsevier
Licensed Content Publication	Materials Science and Engineering: C
Licensed Content Title	Design concept and validation of a robotic arm inspired by the octopus
Licensed Content Author	M. Cianchetti,A. Arienti,M. Follador,B. Mazzolai,P. Dario,C. Laschi
Licensed Content Date	Aug 12, 2011
Licensed Content Volume	31
Licensed Content Issue	6
Licensed Content Pages	10
Start Page	1230
End Page	1239
Type of Use	reuse in a thesis/dissertation
Portion	figures/tables/illustrations
Number of figures/tables/illustrations	1
Format	electronic
Are you the author of this Elsevier article?	No
Will you be translating?	No
Title of new work	Thesis
Institution name	INRIA Lille & Caranx Medical
Expected presentation date	Jan 2026
Portions	Figure of soft robot
The Requesting Person / Organization to Appear on the License	Flavie PRZYBYLSKI
Requestor Location	Flavie PRZYBYLSKI 400 promenade des anglais Nice, France
Publisher Tax ID	GB 494 6272 12
Total	**0.00 EUR**
Terms and Conditions	

INTRODUCTION

1. The publisher for this copyrighted material is Elsevier. By clicking "accept" in connection with completing this licensing transaction, you agree that the following terms and conditions apply to this transaction (along with the Billing and Payment terms and conditions established by Copyright Clearance Center, Inc. ("CCC"), at the time that you opened your RightsLink account and that are available at any time at https://myaccount.copyright.com).

GENERAL TERMS

2. Elsevier hereby grants you permission to reproduce the aforementioned material subject to the terms and conditions indicated.

D.5 Authorization to re-use Figure 2.7

MARY ANN LIEBERT, INC. LICENSE
TERMS AND CONDITIONS

Oct 04, 2025

This Agreement between Flavie PRZYBYLSKI ("You") and Mary Ann Liebert, Inc. ("Mary Ann Liebert, Inc.") consists of your license details and the terms and conditions provided by Mary Ann Liebert, Inc. and Copyright Clearance Center.

License Number	6122020443778
License date	Oct 04, 2025
Licensed Content Publisher	Mary Ann Liebert, Inc.
Licensed Content Publication	Soft Robotics
Licensed Content Title	A Resilient, Untethered Soft Robot
Licensed Content Author	Michael T. Tolley, Robert F. Shepherd, Bobak Mosadegh, et al
Licensed Content Date	Sep 1, 2014
Licensed Content Volume	1
Licensed Content Issue	3
Type of Use	Dissertation/Thesis
Requestor type	academic
Format	electronic
Portion	figures/tables
Number of figures/tables	1
Distribution quantity	1
Title of new work	Thesis
Institution name	INRIA Lille & Caranx Medical
Expected presentation date	Jan 2026
Portions	FIgure of soft robot
The Requesting Person / Organization to Appear on the License	Flavie PRZYBYLSKI
Requestor Location	Flavie PRZYBYLSKI 400 promenade des anglais Nice, France
Payment Type	Invoice
Email Address	flavie.przybylski@caranx-medical.com
Billing Address	Flavie PRZYBYLSKI 400 promenade des anglais Nice, France
Total	**0.00 EUR**
Terms and Conditions	

Mary Ann Liebert, Inc. publishers Terms and Conditions

1. Introduction

The publisher for this copyrighted material is Mary Ann Liebert, Inc. publishers. By clicking "accept" in connection with completing this licensing transaction, you agree that the following terms and conditions apply to this transaction (along with the Billing and Payment terms and conditions established by Copyright Clearance Center, Inc. ("CCC"), at the time that you opened your Rightslink account and that are available at any time at https://myaccount.copyright.com).

2. Limited License

D.6 Authorization to re-use Figure 2.8

THE AMERICAN ASSOCIATION FOR THE ADVANCEMENT OF SCIENCE
LICENSE
TERMS AND CONDITIONS

Oct 04, 2025

This Agreement between PRZYBYLSKI Flavie ("You") and The American Association for the Advancement of Science ("The American Association for the Advancement of Science") consists of your license details and the terms and conditions provided by The American Association for the Advancement of Science and Copyright Clearance Center.

License Number	6122000763315
License date	Oct 04, 2025
Licensed Content Publisher	The American Association for the Advancement of Science
Licensed Content Publication	Science Robotics
Licensed Content Title	A soft robot that navigates its environment through growth
Licensed Content Author	Elliot W. Hawkes, Laura H. Blumenschein, Joseph D. Greer, Allison M. Okamura
Licensed Content Date	Jul 19, 2017
Licensed Content Volume	2
Licensed Content Issue	8
Volume number	2
Issue number	8
Type of Use	Thesis / Dissertation
Requestor type	Scientist/individual at a research institution
Format	Print
Portion	Full Text
Title of new work	Thesis
Institution name	INRIA Lille & Caranx Medical
Expected presentation date	Jan 2026
The Requesting Person / Organization to Appear on the License	PRZYBYLSKI Flavie
Requestor Location	Flavie PRZYBYLSKI 400 promenade des anglais Nice, France
Payment Type	Invoice
Email Address	flavie.przybylski@caranx-medical.com
Billing Address	Flavie PRZYBYLSKI 400 promenade des anglais Nice, France
Total	**0.00 EUR**

Terms and Conditions

American Association for the Advancement of Science ("AAAS") TERMS AND CONDITIONS
Regarding your request, we are pleased to grant you non-exclusive, non-transferable permission, to republish the AAAS material subject to the terms and conditions herein. We must be contacted for permission for any uses other than those specifically identified in your request.

D.7 Authorization to re-use Figure 2.9

THE AMERICAN ASSOCIATION FOR THE ADVANCEMENT OF SCIENCE
LICENSE
TERMS AND CONDITIONS

Oct 04, 2025

This Agreement between PRZYBYLSKI Flavie ("You") and The American Association for the Advancement of Science ("The American Association for the Advancement of Science") consists of your license details and the terms and conditions provided by The American Association for the Advancement of Science and Copyright Clearance Center.

License Number	6122000763315
License date	Oct 04, 2025
Licensed Content Publisher	The American Association for the Advancement of Science
Licensed Content Publication	Science Robotics
Licensed Content Title	A soft robot that navigates its environment through growth
Licensed Content Author	Elliot W. Hawkes, Laura H. Blumenschein, Joseph D. Greer, Allison M. Okamura
Licensed Content Date	Jul 19, 2017
Licensed Content Volume	2
Licensed Content Issue	8
Volume number	2
Issue number	8
Type of Use	Thesis / Dissertation
Requestor type	Scientist/individual at a research institution
Format	Print
Portion	Full Text
Title of new work	Thesis
Institution name	INRIA Lille & Caranx Medical
Expected presentation date	Jan 2026
The Requesting Person / Organization to Appear on the License	PRZYBYLSKI Flavie
Requestor Location	Flavie PRZYBYLSKI 400 promenade des anglais Nice, France
Payment Type	Invoice
Email Address	flavie.przybylski@caranx-medical.com
Billing Address	Flavie PRZYBYLSKI 400 promenade des anglais Nice, France
Total	**0.00 EUR**

Terms and Conditions

American Association for the Advancement of Science ("AAAS") TERMS AND CONDITIONS
Regarding your request, we are pleased to grant you non-exclusive, non-transferable permission, to republish the AAAS material subject to the terms and conditions herein. We must be contacted for permission for any uses other than those specifically identified in your request.

D.8 Authorization to re-use Figure 2.9

MARY ANN LIEBERT, INC. LICENSE TERMS AND CONDITIONS

Oct 04, 2025

This Agreement between Flavie PRZYBYLSKI ("You") and Mary Ann Liebert, Inc. ("Mary Ann Liebert, Inc.") consists of your license details and the terms and conditions provided by Mary Ann Liebert, Inc. and Copyright Clearance Center.

License Number	6122030444891
License date	Oct 04, 2025
Licensed Content Publisher	Mary Ann Liebert, Inc.
Licensed Content Publication	Soft Robotics
Licensed Content Title	Toward Self-Growing Soft Robots Inspired by Plant Roots and Based on Additive Manufacturing Technologies
Licensed Content Author	Ali Sadeghi, Alessio Mondini, Barbara Mazzolai
Licensed Content Date	Sep 1, 2017
Licensed Content Volume	4
Licensed Content Issue	3
Type of Use	Dissertation/Thesis
Requestor type	academic
Format	electronic
Portion	figures/tables
Number of figures/tables	1
Distribution quantity	1
Title of new work	Thesis
Institution name	INRIA Lille & Caranx Medical
Expected presentation date	Jan 2026
Portions	Figure of soft robot
The Requesting Person / Organization to Appear on the License	Flavie PRZYBYLSKI
Requestor Location	Flavie PRZYBYLSKI 400 promenade des anglais Nice, France
Payment Type	Invoice
Email Address	flavie.przybylski@caranx-medical.com
Billing Address	Flavie PRZYBYLSKI 400 promenade des anglais Nice, France
Total	**0.00 EUR**
Terms and Conditions	

Mary Ann Liebert, Inc. publishers Terms and Conditions

1. Introduction

The publisher for this copyrighted material is Mary Ann Liebert, Inc. publishers. By clicking "accept" in connection with completing this licensing transaction, you agree that the following terms and conditions apply to this transaction (along with the Billing and Payment terms and conditions established by Copyright Clearance Center, Inc. ("CCC"), at the time that you opened your Rightslink account and that are available at any time at https://myaccount.copyright.com).

D.9 Authorization to re-use Figure 2.9

MARY ANN LIEBERT, INC. LICENSE TERMS AND CONDITIONS

Oct 04, 2025

This Agreement between Flavie PRZYBYLSKI ("You") and Mary Ann Liebert, Inc. ("Mary Ann Liebert, Inc.") consists of your license details and the terms and conditions provided by Mary Ann Liebert, Inc. and Copyright Clearance Center.

License Number	6122030651323
License date	Oct 04, 2025
Licensed Content Publisher	Mary Ann Liebert, Inc.
Licensed Content Publication	Soft Robotics
Licensed Content Title	A Soft, Steerable Continuum Robot That Grows via Tip Extension
Licensed Content Author	Joseph D. Greer, Tania K. Morimoto, Allison M. Okamura, et al
Licensed Content Date	Feb 1, 2019
Licensed Content Volume	6
Licensed Content Issue	1
Type of Use	Dissertation/Thesis
Requestor type	academic
Format	electronic
Portion	figures/tables
Number of figures/tables	1
Distribution quantity	1
Title of new work	Thesis
Institution name	INRIA Lille & Caranx Medical
Expected presentation date	Jan 2026
Portions	Figure of soft robot
The Requesting Person / Organization to Appear on the License	Flavie PRZYBYLSKI
Requestor Location	Flavie PRZYBYLSKI 400 promenade des anglais Nice, France
Payment Type	Invoice
Email Address	flavie.przybylski@caranx-medical.com
Billing Address	Flavie PRZYBYLSKI 400 promenade des anglais Nice, France
Total	**0.00 EUR**
Terms and Conditions	

Mary Ann Liebert, Inc. publishers Terms and Conditions

1. Introduction

The publisher for this copyrighted material is Mary Ann Liebert, Inc. publishers. By clicking "accept" in connection with completing this licensing transaction, you agree that the following terms and conditions apply to this transaction (along with the Billing and Payment terms and conditions established by Copyright Clearance Center, Inc. ("CCC"), at the time that you opened your Rightslink account and that are available at any time at https://myaccount.copyright.com).

2. Limited License

D.10 Authorization to re-use Figure 2.9

MARY ANN LIEBERT, INC. LICENSE TERMS AND CONDITIONS

Oct 04, 2025

This Agreement between Flavie PRZYBYLSKI ("You") and Mary Ann Liebert, Inc. ("Mary Ann Liebert, Inc.") consists of your license details and the terms and conditions provided by Mary Ann Liebert, Inc. and Copyright Clearance Center.

License Number	6122030954742
License date	Oct 04, 2025
Licensed Content Publisher	Mary Ann Liebert, Inc.
Licensed Content Publication	Soft Robotics
Licensed Content Title	Stiffness Change for Reconfiguration of Inflated Beam Robots
Licensed Content Author	Brian H. Do, Shuai Wu, Ruike Renee Zhao, et al
Licensed Content Date	Oct 1, 2024
Licensed Content Volume	11
Licensed Content Issue	5
Type of Use	Dissertation/Thesis
Requestor type	academic
Format	electronic
Portion	figures/tables
Number of figures/tables	1
Distribution quantity	1
Title of new work	Thesis
Institution name	INRIA Lille & Caranx Medical
Expected presentation date	Jan 2026
Portions	Figure of soft robot
The Requesting Person / Organization to Appear on the License	Flavie PRZYBYLSKI
Requestor Location	Flavie PRZYBYLSKI 400 promenade des anglais Nice, France
Payment Type	Invoice
Email Address	flavie.przybylski@caranx-medical.com
Billing Address	Flavie PRZYBYLSKI 400 promenade des anglais Nice, France
Total	**0.00 EUR**
Terms and Conditions	

Mary Ann Liebert, Inc. publishers Terms and Conditions

1. Introduction

The publisher for this copyrighted material is Mary Ann Liebert, Inc. publishers. By clicking "accept" in connection with completing this licensing transaction, you agree that the following terms and conditions apply to this transaction (along with the Billing and Payment terms and conditions established by Copyright Clearance Center, Inc. ("CCC"), at the time that you opened your Rightslink account and that are available at any time at https://myaccount.copyright.com).

2. Limited License

Résumé en français

La présente thèse de doctorat, *Conception, modélisation et développement d'un robot endoscopique chirurgical souple*, porte sur la conception d'une architecture robotique dédiée à la chirurgie mini-invasive, et plus particulièrement à l'implantation percutanée de valve aortique (TAVI). Elle propose une approche fondée sur la robotique souple à croissance par éversion, afin d'améliorer la sécurité et la précision de la navigation endovasculaire.

Chapitre 1 – Introduction

Ce premier chapitre expose le contexte clinique et les motivations de la recherche. La sténose aortique, pathologie valvulaire la plus fréquente, provoque une surcharge du ventricule gauche liée au rétrécissement de la valve. Le remplacement chirurgical, longtemps réservé aux patients à faible risque opératoire, a vu son champ d'application élargi grâce à l'émergence du TAVI, initiée par Alain Cribier et réalisée pour la première fois en 2002. Les systèmes développés par Edwards Lifesciences ont permis la généralisation de la voie transfémorale, moins invasive. Malgré plus d'un million de procédures réalisées, la navigation de cathéters rigides dans des artères tortueuses et calcifiées demeure une source majeure de complications (perforation, dissection, AVC embolique).

L'objectif de cette thèse est de concevoir un robot souple à croissance par éversion, actionné par fluide, capable de suivre la géométrie vasculaire avec des forces de contact minimales. Le chapitre se conclut par la présentation de la structure du manuscrit : l'historique de l'éversion (Chapitre 2), la modélisation et l'optimisation (Chapitres 3-4), la validation expérimentale (Chapitre 5) et les perspectives (Chapitre 6).

Chapitre 2 – Du cathéter à la robotique souple

Ce chapitre retrace l'évolution des dispositifs endoluminaux, depuis les premiers cathéters jusqu'aux robots souples basés sur l'éversion. Les cathéters classiques présentent des limitations intrinsèques liées à la friction et au compromis entre rigidité et flexibilité. Le brevet fondateur de Daniel Silverman (1963) introduit le principe d'éversion, où une gaine flexible se retourne sur elle-même sous pression interne, assurant une progression sans glissement.

Ce principe a inspiré divers dispositifs de drainage, d'échantillonnage ou à des fins thérapeutiques. Le cathéter toposcopique, développé dans les années 1970, a validé la faisabilité in vivo de l'éversion à 65 kPa grâce à un tube en TPU avec revêtement hydrophile. Dans les années 2010, la robotique souple a réinterprété cette idée sous la forme des robots à croissance (vine/growing robots), dont la progression imite celle des plantes grimpantes.

Un premier prototype textile/silicone préformé a été testé pour l'application TAVI, mais a conduit à une rupture artérielle dans un modèle cadavérique, révélant que la pressurisation saline conférait une rigidité excessive au matériau.

Chapitre 3 – Modélisation du robot basé sur l'éversion

Afin d'analyser et d'optimiser le comportement du robot, un cadre de modélisation numérique hybride a été développé. Celui-ci vise à combiner la légèreté computationnelle des modèles géométriques à fibres avec la précision locale des méthodes de maillage de surface, afin de décrire à la fois la cinématique globale du corps et les phénomènes locaux au niveau de la membrane. Le modèle repose sur une représentation à fibres, adaptée aux grandes déformations et à la description cinématique du robot, couplée à la méthode des éléments finis (FEM), particulièrement appropriée pour la modélisation des contacts, des plis et des frictions internes.

Le robot est divisé en trois zones fonctionnelles distinctes : (S1) la zone stockée, (S2) la zone d'éversion et (S3) la zone déployée. Le couplage entre les modèles s'effectue par des ressorts reliant les nœuds du modèle FEM aux fibres géométriques, permettant une transition fluide entre rigidité et déformation libre au fur et à mesure du déploiement. Cette approche offre une première représentation con-

tinue de l'éversion tout en maintenant la stabilité numérique. Les simulations ont reproduit fidèlement les formes d'éversion observées expérimentalement, ainsi que la redistribution des contraintes lors du passage dans des environnements contraints, confirmant la pertinence du couplage pour prédire le comportement mécanique global du robot.

Chapitre 4 – Modélisation raffinée et optimisation structurelle

Ce chapitre présente une modélisation unifiée en coques minces (thin-shell FEM) intégrant simultanément la rigidité en traction et en flexion. Les fibres servent désormais uniquement de support géométrique pour générer des maillages de qualité. Un ajustement empirique du terme de rigidité en flexion (remplacement de $h^3/12$ par h^2) a permis d'assurer la stabilité numérique pour des épaisseurs inférieures à 100 µm.

Un guide numérique à ressorts variables a été introduit pour concentrer les calculs dans la zone d'éversion et garantir un déploiement stable et continu. Cette approche a renforcé la cohérence entre la simulation et les comportements physiques observés.

Chapitre 5 – Conception, contrôle et validation expérimentale

Les validations expérimentales ont permis de confronter la simulation aux essais physiques. Le système d'actionnement utilise une pompe à double seringue injectant une solution saline (0,9 % NaCl) à travers un réservoir amorti par une chambre à air. Le TPU s'est révélé supérieur au LDPE, présentant une pression d'éversion stable de 18 kPa et une meilleure conformité. La découpe laser avec un décalage de 2 mm a permis d'assurer l'étanchéité des jonctions.

Le TPU a franchi des sténoses de 5 mm et 4 mm de diamètre à des pressions inférieures à 70 kPa, soit près de 17 fois moins que la pression minimale nécessaire au déploiement d'un stent coronarien. Une validation préclinique a ensuite été menée dans des fantômes anatomiques, un cadavre humain et un modèle porcin vivant. Le contrôle en boucle fermée a permis un déploiement autonome stable jusqu'à la crosse aortique. Des ruptures localisées au niveau des jonctions soudées ont toutefois mis en évidence un point faible de la conception, appelant à une

optimisation du procédé d'assemblage.

Chapitre 6 – Conclusion et perspectives

Les travaux ont confirmé que la pressurisation saline augmente la rigidité du robot, et que le TPU constitue le matériau le plus adapté à une navigation atraumatique. Les contributions principales incluent: le développement d'un modèle hybride à base de fibres et d'un modèle FEM à coque mince la conception d'un robot souple pressurisé et préformé pour la navigation endovasculaire; et la validation expérimentale et préclinique d'un contrôle autonome par pression régulée.

Les perspectives de cette recherche concernent à la fois l'amélioration de la durabilité des jonctions du robot et l'intégration de capteurs embarqués destinés au suivi des paramètres internes en temps réel. Le modèle numérique sera également affiné afin de prendre en compte les comportements non linéaires du matériau, les phénomènes de friction et la compliance vasculaire. Enfin, les principes développés pourraient être transposés à d'autres champs cliniques, notamment la neurochirurgie, la bronchoscopie et la chirurgie bariatrique.

Annexe B – Applications bariatriques : études complémentaires

Cette annexe présente des travaux exploratoires pour adapter le robot à la gastroscopie. Un prototype de 15 mm en LDPE intégrant une capsule de 14 mm (caméra et pince à biopsie) a été testé, mais les soudures se sont avérées fragiles. Une capsule électronique embarquée dotée de capteurs de pression et de mouvement a démontré la faisabilité d'un monitoring en temps réel via Bluetooth. Une alternative plus prometteuse consiste à imprimer des encres conductrices sur la membrane en TPU pour assurer la mesure et la transmission directement depuis la paroi du robot. La conductivité est restée stable après flexion, bien que la durabilité doive encore être améliorée pour une application clinique.

Mots-clés : robotique souple, robot à croissance, éversion, TAVI, modélisation numérique, TPU, chirurgie mini-invasive.